

DYE SENSITIZED SOLAR CELLS: OPTIMIZATION OF GRÄTZEL SOLAR CELLS  
TOWARDS PLASMONIC ENHANCED PHOTOVOLTAICS

by

JEREMY ESSNER

B.S., Benedictine College, 2008

A THESIS

submitted in partial fulfillment of the requirements for the degree

MASTER OF SCIENCE

Department of Chemistry  
College of Arts and Sciences

KANSAS STATE UNIVERSITY  
Manhattan, Kansas

2011

Approved by:

Major Professor  
Jun Li

# **Copyright**

JEREMY ESSNER

2011

## Abstract

With the worldly consumption of energy continually increasing and the main source of this energy, fossil fuels, slowly being depleted, the need for alternate sources of energy is becoming more and more pertinent. One promising approach for an alternate method of producing energy is using solar cells to convert sunlight into electrical energy through photovoltaic processes. Currently, the most widely commercialized solar cell is based on a single p-n junction with silicon. Silicon solar cells are able to obtain high efficiencies but the downfall is, in order to achieve this performance, expensive fabrication techniques and high purity materials must be employed. An encouraging cheaper alternative to silicon solar cells is the dye-sensitized solar cell (DSSC) which is based on a wide band gap semiconductor sensitized with a visible light absorbing species. While DSSCs are less expensive, their efficiencies are still quite low compared to silicon. In this thesis, Grätzel cells (DSSCs based on  $\text{TiO}_2$  NPs) were fabricated and optimized to establish a reliable standard for further improvement. Optimized single layer GSCs and double layer GSCs showing efficiencies  $>4\%$  and efficiencies of  $\sim 6\%$ , respectively, were obtained. Recently, the incorporation of metallic nanoparticles into silicon solar cells has shown improved efficiency and lowered material cost. By utilizing their plasmonic properties, incident light can be scattered, concentrated, or trapped thereby increasing the effective path length of the cell and allowing the physical thickness of the cell to be reduced. This concept can also be applied to DSSCs, which are cheaper and easier to fabricate than Si based solar cells but are limited by lower efficiency. By incorporating 20 nm diameter Au nanoparticles (Au NPs) into DSSCs at the FTO/ $\text{TiO}_2$  interface as sub wavelength antennae, average photocurrent enhancements of 14% (maximum up to  $\sim 32\%$ ) and average efficiency enhancements of 13% (maximum up to  $\sim 23\%$ ) were achieved with well dispersed, low surface coverages of nanoparticles. However the Au nanoparticle solar cell (AuNPSC) performance is very sensitive to the surface coverage, the extent of nanoparticle aggregation, and the electrolyte employed, all of which can lead to detrimental effects (decreased performances) on the devices.

# Table of Contents

List of Figures .....	vi
List of Tables .....	xix
Acknowledgements .....	xx
Dedication .....	xxi
Chapter 1 - I Saw the Light! .....	1
Energy Crisis & Global Warming .....	1
Necessity for Sustainability .....	2
Alternatives to Present Energy Economy .....	3
Solar Energy Harvesting .....	4
Photovoltaic Generations (1 <sup>st</sup> , 2 <sup>nd</sup> , & 3 <sup>rd</sup> ).....	4
Solid State Devices .....	7
Dye-Sensitized Devices .....	9
Incorporation of Metallic Nanoparticles .....	11
Photovoltaic Device Characterizations .....	14
Chapter 2 - Solar Simulator System: Setup & Beam Alignment.....	25
Newport Solar Simulator System .....	27
Solar Simulator System Setup and Calibration.....	30
300 Watt Broadband Light Source.....	31
75 Watt Monochromatic Light Source.....	37
Calibrated Si Reference Cell.....	42
Conclusions.....	45
Chapter 3 - Fabrication & Optimization of Grätzel Cells.....	46
Benchmark Grätzel Cell.....	47
Optimized Fabrication of Dye-Sensitized Solar Cell .....	48
Device Fabrication .....	48
Device Assembly .....	49
Photoanode & Device Characterization .....	50
Dye-Sensitized Solar Cell Optimization.....	51
Optimization Process .....	53

Further Device Characterizations .....	65
Conclusions.....	68
Chapter 4 - Material Properties and Performance Effects of Dye-Sensitized Solar Cells (DSSC's)	
containing Au Nanoparticles (NPs).....	69
Device Rationale.....	69
AuNP DSSC's Synthesis and Assembly .....	73
Device Fabrication .....	73
Device Assembly .....	76
Photoanode & Device Characterization.....	76
Device Characterizations .....	78
Additional Characterizations .....	86
Conclusions.....	86
Chapter 5 - Overall Conclusions and Future Outlook .....	88
References.....	90
Appendix A - Solar Simulation System.....	96
Appendix B - Reference Cell Data Supplied by PV Measurements, Inc. ....	100
Appendix C - Optimization of GSCs .....	102
Appendix D - AuNP Incorporated DSSC's .....	109

## List of Figures

- Figure 1.1 World Energy Consumption Timeline<sup>3</sup> & 2006 Energy Source Usage (%)<sup>4</sup> The left image shows a timeline from 1965 to 2005 of the continually increasing power consumption of fuels with fossil fuels being the major contributors. (Used with permission from ref. 3. Copyright © 2007 Frank V. Mierlo) The right image shows a linear bar graph of the percentage of fuels consumed in 2006 again showing that fossil fuels (non-renewable sources) comprise over 90% while renewable sources (solar, wind) constitute <1%. (Used with permission from ref. 4. Copyright © 2008 Omegatron) ..... 2
- Figure 1.2 Remaining Oil Energy<sup>5</sup> The estimated energy amounts and percentages of the various oil sources are shown above. A median estimate of 57 ZJ of oil energy is believed to remain on earth with 8 ZJ as a low end estimate and 110 ZJ as a high end estimate. For the median estimate with an increasing consumption rate of 2 EJ/year the oil supplies would run out in ~150 years. (Used with permission from ref. 5. Copyright © 2008 Frank van Mierlo) ..... 3
- Figure 1.3 Total Possible Available Power of Renewable Sources<sup>6</sup> Of all the renewable sources, solar is one of the more promising to replace fossil fuels due to the 86 PW of power that is supplied to the Earth’s surface. This 86 PW is more than 5000x the current global consumption of 15 TW. (Used with permission from ref. 6. Copyright © 2008 Delphi234, based on work by Frank v. Mierlo)..... 4
- Figure 1.4 Solar Cell Generations - Cost vs. Efficiency<sup>13-15</sup> Photovoltaic devices are segregated into three generations; 1<sup>st</sup>) Solid-state devices (mainly Si), 2<sup>nd</sup>) thin film devices, 3<sup>rd</sup>) Devices not in 1<sup>st</sup> & 2<sup>nd</sup> (3D hierarchical, organic/polymer devices, tandem cells, etc.). The 2<sup>nd</sup> generation was developed to circumvent the expensive 1<sup>st</sup> generation but both are limited by the Shockley-Queisser theoretical limit. The 3<sup>rd</sup> generation tackles both these issues with low cost, high efficiency devices that have the potential of being pushed above the thermodynamic limit by strategic device design. (Used with permission from ref. 13. Copyright © 2007 IOP Publishing) ..... 5
- Figure 1.5 Best Efficiencies Obtained for Research Photovoltaic Cells<sup>36</sup> Since 1975, as the generations of photovoltaics have evolved, the best obtained efficiencies for research cells

have steadily been climbing with 1<sup>st</sup> generation Si solar cells approaching the Shockley-Queisser limit and 3<sup>rd</sup> generation multijunction (tandem) devices reaching upwards of 43%. (Used with permission from ref. 36, Updated image came directly from author. Copyright © 2011 NREL)..... 6

Figure 1.6 Solid State Device Schematic A solid state photovoltaic device consists of a n-type semiconductor placed in contact with a p-type semiconductor forming a p-n junction. When brought into contact, the excess charges in the materials diffuse across the semiconductor interface and combine with an opposing charge. This diffusion leads to the formation of a depletion layer in which excess negative charges are left in the p-type and excess positive charges are left in the n-type which gives rise to a built-in electric field. .... 7

Figure 1.7 PN Junction Operation When subjected to a photon flux of appropriate energy, the photons are absorbed and an electron-hole pair is generated. With the help of the built-in electric field, the generated charges are swept away, separated and begin to diffuse towards the front and rear contacts. The generated electrons will diffuse towards the top contact (cathode) and the generated holes towards the bottom contact (anode). .... 9

Figure 1.8 DSSC Components & Operation<sup>37</sup> A DSSC consists of a semiconductor sensitized with a visible light absorbing species (dye) sandwiched in between a transparent conductive electrode and a counter electrode with a redox couple filler to shuttle the charges to and from the CE and the dye/semiconductor interface. When the dye absorbs incident light, an electron is excited and can then be injected into the semiconductor, where it percolates through and is ideally collected to do work. (Used with permission from ref. 37. Copyright © 2009 M. R. Jones) ..... 10

Figure 1.9 Surface Plasmon Resonance Schematic<sup>58</sup> When the size of a particle is reduced to sub wavelength dimensions, the particle will experience a uniform electric field as incident light interacts with the particle. This uniform electric field causes the charges in the particle to oscillate with the electric field. This oscillation acts a restoring force leading to resonance at a particular frequency. This resonance can be exploited for enhancing photovoltaics. (Image adapted from ref. 58.) ..... 12

Figure 1.10 Light Trapping Geometries<sup>56</sup> Depending on the size and geometry of the particle, the particle can be employed in different geometrical setups to achieve various light trapping.

Incident light can be scattered (far left), concentrated (center), and/or redirected (far right).

(Used with permission from ref. 56. Copyright © 2010 Nature Publishing Group) ..... 12

Figure 1.11 Schematic Dark & Illuminated IV Curves with Equivalent Circuit Model Displayed on the schematic IV curve are the short circuit current density ( $J_{SC}$ ), open circuit voltage ( $V_{OC}$ ), theoretical power ( $P_{Theoretical}$ ), current density at the maximum power output ( $J_{MP}$ ), voltage at the maximum power output ( $V_{OC}$ ), and the maximum power output ( $P_{max}$ ) of the device. The photovoltaic device can be modeled by the simple equivalent circuit shown on the right. .... 15

Figure 1.12 Maximum Power Output Curve The maximum power density output of the device can be determined by plotting the product of the current values and the voltage values vs. the original voltage values. A parabolic curve should be obtained with the maximum of the curve being the maximum power output..... 17

Figure 1.13 Schematic Dark Back Reaction Critical information regarding charge transport properties can be inferred from the IV response under dark conditions by plotting the dark current density in log scale over a specified voltage range..... 18

Figure 1.14 Schematic IPCE The incident photon to current conversion efficiency provides information into how efficiently the device converts photons into electrons (current) at each wavelength. Characteristic UV-Vis peak absorption wavelengths ideally will correspond to the peak IPCE wavelengths. .... 19

Figure 1.15 Schematic Chronoamperogram Chronoamperometry can provide three key pieces of information about the device; the stability of the device, whether it is limited by diffusion and if so what is the diffusion coefficient of the electrolyte. As the illumination is continually interrupted, a stable device will have the same current response during each illumination period. If the device is diffusion limited, a decay in the photocurrent is visible. This decay can be plotted vs. time<sup>-0.5</sup> and the apparent diffusion coefficient can be extracted. .... 21

Figure 1.16 Schematic Chronopotentiogram Similar to chronoamperometry, chronopotentiometry can provide critical information into the device stability and charge transfer properties. The decay in the photovoltage can be used to determine the recombination lifetime of electrons in the electrolyte. .... 21

Figure 1.17 Schematic EIS Spectra of DSSC The Nyquist plot for a DSSC consists of three semicircles; the first one representing the charge transfer resistance at the CE (kHz region), the 2<sup>nd</sup> representing the charge transfer resistance in the photoanode (Hz region), and the third representing the electrolyte resistance (mHz region). Plotting the data in a Bode phase plot and extracting the peak frequency of the 2<sup>nd</sup> semicircle will give information into the electron lifetime in the semiconductor film. .... 23

Figure 1.18 DSSC Equivalent Circuit The Nyquist plot of a DSSC can be modeled by a resistor and two RC circuits in series, with one RC circuit containing a finite-Warburg Impedance element,  $Z_w$ .  $R_s$  corresponds to the resistance of the electrolyte and the electric contacts. The two RC circuits ( $Q$  = capacitor,  $C$ , of variable capacitance) represent the charge transfer resistances at the counter electrode/electrolyte interface ( $R_{CTCE}$ ) and the dye/semiconductor/electrolyte (photoanode) interface ( $R_{CTPA}$ ) as well as the double layer capacitances at each interface ( $Q$ ). .... 23

Figure 2.1 Solar Energy Diagram<sup>68</sup> Of the 174 PW of solar power that reaches the Earth’s outer atmosphere, 89 PW is not reflected or absorbed by the atmosphere, allowing massive amounts of energy to be harvested through photovoltaic devices. (Used with permission from ref. 68. Copyright © 2008 Frank v. Mierlo)..... 25

Figure 2.2 Solar Radiation Spectrum<sup>69</sup> The spectrum of the 174 PW of sunlight reaching the upper atmosphere is represented by the yellow (plus the orange) curves. The power reduction to 89 PW due to the atmosphere arises from the absorption of light (& reflection – not shown) from the greenhouse gases ( $O_3$ ,  $H_2O$ ,  $O_2$ , and  $CO_2$ ) which produces the spectrum of solar radiation at sea level (orange). (Used with permission from ref. 69. Copyright © 2007 Robert A. Rohde) ..... 26

Figure 2.3 Standard Solar Spectra<sup>70</sup> Shown in blue is the standard solar spectra, developed (AM1.5 Global) for solar simulation measurements. The spectrum represents the standard irradiance of  $100 \text{ mW/cm}^2$  used for photovoltaic characterizations. Also shown are the AM0 spectrum (solar radiation outside the atmosphere) and the AM1.5D spectrum (only includes the direct solar radiation onto the earth, not direct and diffuse – AM1.5G). (Used with permission from ref. 70. Copyright © Christiana Honsberg and Stuart Bowden, original work and data from SMARTS modeling program used at NREL) ..... 27

Figure 2.4 Newport Solar Simulator Above is an actual picture of the solar simulator setup with the major components labeled. .... 28

Figure 2.5 Newport Solar Simulator Schematic (See Table 2.1) Schematic of the overhead view of the major solar simulator components that are shown in Figure 2.4 as well as their locations on the supporting laser table. .... 29

Figure 2.6 Schematic of Possible Incident Lamp Beams Ideally, an incident beam of light irradiating from the lamp that consisted of uniform power across the beam would be achieved as seen in A above. The reality is that the power of the incident beam is more conical shaped in its magnitude i.e. high power at the center with the power decreases away from the center (B). The goal is then to spread this uniformity outward across the beam as much as possible to give more of a dome shaped beam as shown in C above. .... 31

Figure 2.7 300 W Lamp Setup Schematic The schematic above shows the path that the irradiated light takes from the 300 W source. Light irradiated in the forward direction (to the right in the schematic) goes directly to through the condenser tube towards the sample. In order to collect as much light as possible and increase the intensity subjected on the sample, light irradiated in the backwards direction (to the left in the schematic) is re-directed forward with a reflector mirror and is then collimated with the condenser lens before striking the sample. .... 32

Figure 2.8 Arc Lamp & Arc Lamp Image Alignment For proper alignment of the 300 W arc lamp, the actual arc and the arc image (created by back reflector mirror) need to be superimposed in such a manner that the “hot spots” of the electrodes (tip of point electrode) do not lie directly over the larger curved anode as seen in C of the above figure. .... 33

Figure 2.9 300 W Lamp Incident Power vs Time For proper use of the 300 W lamp, the lamp needs time to warm up and the irradiated power needs to stabilize before characterizing any devices. A warm up period of 20 minutes is sufficient enough for lamp usage but complete stabilization does not occur until at least 30 minutes of warm up time. .... 34

Figure 2.10 300 W Lamp Acceptable Uniformity The desired beam uniformity is a power density variation of less than 10% over a 1 cm<sup>2</sup> area. After many adjustments to the lamp position, a uniformity of 8.72% over 1 cm in the x-direction and 4.79% over 1 cm in the y-direction was obtained which is well within the desired outcome. Additional fine tunings could be made to further improve the uniformity. .... 35

Figure 2.11 300 W Lamp Final Uniformity Following fine adjustments to the lamp to further improve the previous beam uniformity achieved, a final beam uniformity of 7.27% over 1 cm in the x-direction and 3.77% over 1 cm in the y-direction was obtained. The beam uniformity could potentially be further improved but these values are well within the desired power density variation..... 36

Figure 2.12 75 Watt Lamp Setup Schematic The schematic above shows the path that the irradiated light takes from the 75 W source. In order to collect as much light as possible and increase the intensity subjected on the sample, white reflector plate are placed on two sides of the lamp to re-direct the light towards the reflector mirror. From the reflector mirror, the broadband light is monochromatized and is then collimated with the condenser lens before striking the sample. .... 37

Figure 2.13 75 W Lamp Acceptable Uniformity at 550 nm Due to the sensitizer employed (N719 -  $\lambda_{\text{max abs}} = 530 \text{ nm}$ ), the uniformity of the monochromatic light was first tested at 550 nm. Again a uniformity of a power density variation of less than 10% over a  $1 \text{ cm}^2$  area is desired. After some alterations in the reflector mirror position an acceptable uniformity of 6.72% over  $\sim 2.0 \text{ cm}$  in the x direction and 4.79% over  $\sim 2.0 \text{ cm}$  in the y-direction was obtained..... 38

Figure 2.14 75 W Lamp Uniformities vs Wavelength (X&Y Axes) After achieving a decent beam uniformity at 550 nm, the uniformity at other wavelengths was tested. The uniformity was found to be very wavelength dependent but the uniformities over the visible range, which are the wavelengths of interest, are roughly within the desired power density variation. The power density variations vs wavelength for the above curves are in Table 2.2..... 39

Figure 2.15 75 W Lamp Final Uniformity Further improvements were made to the acceptable uniformity shown in Figure 2.13 to obtain a final uniformity of 9.43% over 2.4 cm in the x-direction and 7.97% over 2.4 cm in the y-direction..... 40

Figure 2.16 Monochromator Components Optimization The default wavelength settings at which the gratings and filter wheel changed gave rise to massive power reductions in the incident beam. By optimizing the wavelengths at which the filter wheel rotated and the wavelength at which the gratings switched, the power variation across the wavelength range of interest was greatly reduced i.e. power reductions were minimized. .... 41

Figure 2.17 Reference Cell IV Curves - Original Power vs Calibrated Power for 1 Sun With 280 Watts applied to the lamp, a detector reading of  $100 \text{ mW/cm}^2$  was obtained. This value was ignorantly assumed to be accurate, which led to sub-par device performance. Testing the performance of a calibrated Si reference cell at this lamp power gave a 2/5 reduction in the photocurrent than what should have been achieved. By increasing the power to 330 Watts (detector reading of  $160 \text{ mW/cm}^2$ ), the desired IV response of the reference cell was attained, leaving the broadband lamp calibrated for further tests. .... 43

Figure 2.18 Measured IV & IPCE of Reference Cell The measured IV response (in current density) and IPCE response of the reference cell coincide with the calibrated curves provided by the supplier (Figure B.1 & B.2) which indicates proper lamp calibration. Table 2.4 compares the measured values with the calibrated values further showing the proper lamp calibration. .... 44

Figure 3.3.1 DSSC Components Above is a schematic of the basic DSSC components. The device consists of three main parts; the photoanode, the counter electrode, and the electrolyte. The photoanode is a film of a sensitized semiconductor sintered to a transparent conductive oxide (TCO) substrate. The counter electrode is simply a Pt coated TCO substrate and the electrolyte consists of a redox couple to shuttle charges from the photoanode and CE. The photoanode and CE are sealed together with a hot melt spacer and the electrolyte fills in the gap. .... 47

Figure 3.2 Solar Cell Fabrication Flow Chart The above chart shows the simplified preparation steps for a DSSC from bare substrates to a fully assembled functioning device. .... 48

Figure 3.3 IV Curves - Optimized Double & Single Layer GSCs Four preparation steps were found to be critical in the fabrication of reasonably efficient GSCs: 1) the transparent conductive oxide (TCO) employed, 2) the method of the Pt application for the CE and its subsequent thickness, 3) the period of time that the  $\text{TiO}_2$  paste was allowed to relax prior to sintering, 4) the integrity of the  $\text{TiCl}_4$  solution for the  $\text{TiCl}_4$  treatment. After optimization of these preparation steps, single layer and double layer GSCs displaying efficiencies  $>4\%$  and  $\sim 6\%$ , respectively, were obtained. .... 53

Figure 3.4 Critical Parameter's Effects on IV Characteristics The effects of the optimization of the four critical preparation steps is shown above. All the optimizations improved (lowered) the series resistance of the devices, which led to higher photocurrents and in turn

higher fill factors and efficiencies. The decreased series resistances and improved properties are made apparent in Table 3.2. .... 54

Figure 3.5 TCO Thermal Stability The criticalness of the choice of which transparent conductive oxide (FTO vs ITO) is employed is evident from the above graph. In order to fabricate a GSC, the transparent conductive electrodes (TCE) need to be subjected to temperatures >500°C. At temperatures this high (first thermal treatment - 525°C), the conductivity of ITO is drastically reduced which would detrimentally increase the series resistance if employed in a device. .... 56

Figure 3.6 IV Curves - ITO vs FTO Due to the increased sheet resistance of ITO upon the thermal treatments required for device fabrication, the overall series resistances of the devices is increased to such an extent that unfavorable effects occur. The increased series resistances decrease the photocurrents and fill factors leading to low efficiency devices. By replacing the ITO substrates with FTO the series resistance reductions can be avoided giving respectable IV responses..... 57

Figure 3.7 IV Curves - Different Pt CEs Using a Pt catalyst paste as the CE material can cause an increase in the series resistance of a device due to the formation a non-uniform film of Pt. By sputtering an appropriate thickness of Pt (50 nm) onto the substrate instead, lower series resistances can be obtained that give high photocurrents and reasonable efficiencies. If the Pt thickness is too thin (40 nm) resulting in a non-continuous film or too thick (80 nm) resulting in larger film resistances, similar heightened series resistances can occur..... 58

Figure 3.8 IV Curves - TiCl<sub>4</sub> Solution Effects Without careful preparations of the TiCl<sub>4</sub> solution, the solution integrity is prone to being compromised which could causes adverse effects on the photovoltaic characteristics. Due to the exothermic nature of the TiCl<sub>4</sub> dilution, all the solutions used for the dilution need to be stored at ~4°C and an ice bath with a magnetic stir bar need to be employed upon dilution. Utilizing this methods ensures a high quality TiCl<sub>4</sub> solution so that upon substrate treatment, decent electrical connections and dye adsorption can be achieved which will result in high photocurrents, reasonable fill factors, and moderate efficiencies. .... 61

Figure 3.9 IV Curves - Paste Relaxation Allowing the TiO<sub>2</sub> paste to relax, reducing the surface irregularities, is the key critical fabrication step. Using the other optimized steps discussed above and allowing the paste to relax for four hours can result in an efficient device but the

variation in the performance is unpredictable. To obtain a double layer GSC with a reasonable reproducible performance, at least a 10 hour past relaxation period is required. 63

Figure 3.10 IV Curves - Optimization of Single Layer GSCs Single layer GSCs were optimized in the same manner as the double layer devices. Using the fully optimized fabrication steps with a four hour relaxation period, single layer GSCs of modest efficiencies were reproducibly fabricated. .... 64

Figure 3.11 IPCE - Double & Single Layer GSCs The incident photon to current conversion efficiencies (IPCE) were collected for double and single layer GSCs. The three characteristic peaks (350 nm - TiO<sub>2</sub>, ~400 nm & 530 nm – dye) of the photoanode components were present. As expected the IPCE for double layer cells was higher than that of the single layer cells but large differences between individual devices within the groups was present. This discrepancy is under investigation. .... 66

Figure 3.12 GSC Illumination On/Off Measurements The interrupted illumination measurements of the V<sub>OC</sub> and the J<sub>SC</sub> of the devices shows that the devices were stable during the testing period and the photocurrent is not limited by electrolyte diffusion. .... 66

Figure 3.13 EIS of GSCs – Nyquist Plot & Bode phase plot Electrical impedance spectroscopy can give vital information into the charge transfer processes occurring within the device. The Nyquist and bode phase plots show similar results for three optimized cells (blue, green, and purple). The cause of the poor series resistance (IV curve with J<sub>SC</sub> of ~6 mA/cm<sup>2</sup> in Figure 3.10) of the non-optimized cell (red), is evident after EIS. The impedance of the counter electrode and the photoanode are both substantially increased which leads to a shorter electron lifetime (Table 3.3) and reduced device performance. .... 68

Figure 4.1 AuNP Incorporated DSSC Design The AuNP incorporated device is essentially a single layer GSC with 20 nm AuNPs placed at the TiO<sub>2</sub>/FTO interface. .... 70

Figure 4.2 UV-Vis Absorption of Au NP Solution & Sensitizer (N719) Due to the sensitizer employed (N719 - λ<sub>max abs</sub> = 530 nm), AuNPs (20 nm) exhibiting a surface plasmon resonance near this wavelength were chosen to ensure the coupling of the nanoparticle and dye. .... 70

Figure 4.3 Electric field enhancement around metallic nanoparticle<sup>56</sup> A coupling between the dye and nanoparticle arises due to a intense electric field enhancement around the nanoparticle. The coupling would hopefully increase the photocurrent of the devices which should in turn

led to increased efficiencies. (Used with permission from ref. 56. Copyright © 2010 Nature Publishing Group).....	71
Figure 4.4 IV Curves – AuNPSCs Enhanced vs Un-enhanced AuNP incorporated devices exhibited both favorable and adverse effects when compared to the performance of single layer GSCs. The devices were grouped into enhanced cells (higher photocurrent than GSC) and un-enhanced cells (similar or lower photocurrent than GSC). The effects on the photocurrent were extremely sensitive to the nanoparticle coverage and dispersion, with well dispersed, lower surface coverage devices exhibiting the highest photocurrent enhancements.....	72
Figure 4.5 Schematic of the AuNP Application Methods Two different application methods were used for the deposition of the AuNPs; casting (drop or spin) and functionalization. For the casting methods the AuNPs were just applied directly to the FTO substrate. In order to functionalize the FTO surface, a silane linker that would electrostatically interact with the AuNPs, was covalently bound to the FTO substrate and then the AuNPs were applied to the silanized FTO.....	74
Figure 4.6 FESEM of AuNP Functionalization – Medium & Low NP Densities (A) , (B), & (C) are of ~15% surface coverage and (D), (E), & (F) are of ~1.6% surface coverage at different magnifications. Well dispersed AuNPs were observed at low density surface coverages of about 2% while at higher surface coverages, large aggregates of NPs were visible.....	79
Figure 4.7 UV-Vis Spectra AuNP Photoanodes The AuNPs absorb <20% of incident photons which is highly desired; if the AuNPs absorb too much light, less light will reach the dye to generate photocurrent. As expected, higher surface coverage generally showed lower transmittance. Due to functionalization inconsistencies and aggregation, large deviations in the amount of transmitted light are present.....	80
Figure 4.8 IV Curves - AuNP Surface Coverage The AuNP incorporated devices were re-grouped by their surface coverages. In general, devices with lower surface coverages, which had less aggregated particles, gave higher photocurrent enhancements. Large deviations in device performances between similar surface coverages were apparent. The deviations were attributed to the inconsistencies in the functionalization and aggregation of the NPs.....	81

Figure 4.9 FESEM - Thermal & Electrolyte Treatments Effects Upon thermal treatment of the AuNP functionalized substrates, the NPs lose their stabilizing ligand which causes them to fuse together into bigger particles (B). Due to the variability in functionalization and the high degree of aggregation, this fusing of particles could lead to large films of Au on the sample and in turn have adverse effects. Another issue is the corrosive nature electrolyte employed ( $I/I_3^-$ ). When the substrates are subjected to the  $TiCl_4$ , a thin layer of  $TiO_2$  is deposited over the surface (C) which ideally would shield the NPs from the corrosive electrolyte but as is evident in (D), after electrolyte treatment only AuNP remnants remain, indicating poor device stability. .... 83

Figure 4.10 IPCE – AuNPSCs To better understand the photocurrent effects, the incident photon to current conversion efficiencies were assessed on various cells. Similar trends to the IV curves in Figure 4.8 were expected but the exact opposite was observed. The lower surface coverage cells generally gave lower IPCE than the higher surface coverage cells and the GSCs. The speculation is that the plasmonic effects are not as prominent at the low light intensities used for the IPCE. .... 84

Figure 4.11 IV Curves - AuNPSCs Performance At Different Light Intensities To investigate the observed IPCE phenomena, the IV responses of AuNPSCs of different surface coverages were measured at lower light intensities (1 sun, 0.5 sun, 0.25 sun). The general trend of lower surface coverages giving larger enhancements is again confirmed. .... 85

Figure 4.12 Photocurrent Density Differences of AuNPSCs vs GSCs The short circuit current densities from Figure 4.11 were extracted and the percent difference between the AuNPSCs and the GSC was calculated. Plotting this difference vs the log scale of the light intensity shows that at lower light intensities the photocurrent difference drops below zero, meaning that at low incident light the plasmonic effects are likely non-beneficial and could actually have quenching effects. .... 86

Figure A.1 Solar Simulator System Complete Schematic A complete schematic of the solar simulator setup including the components on the lower breadboard (laser table) and the upper shelf components (all in dotted lines). .... 97

Figure A.2 Solar Simulator Lower Breadboard Schematic The lower breadboard components consist of the two light sources, the monochromator, the motorized shutter, the sample tracks, and the source measure unit. .... 98

Figure A.3 Solar Simulator Upper Shelf Schematic The components on the upper shelf consist of the 300 W lamp power supply, the motorized shutter power supply, and both detectors/power meters (broadband & monochromatic).....	99
Figure A.4 75 Watt Lamp Warm up Period Similar to the 300 W lamp, the 75 Watt Lamp requires at least a 15 minute warm up period to reach a moderately stable power output but a 30 minute time interval should be used to achieve full stabilization. ....	99
Figure B.1 IV Curve for Calibrated Reference Cell .....	100
Figure B.2 IPCE for Calibrated Reference Cell.....	101
Figure C.1 Calculated Efficiencies - As Measured vs Power Density Corrected The efficiencies of the solar cells tested prior to implementation of the reference cell were re-calculated accounting for the discrepancy in the measured power density. Efficiencies slightly over 4% could have been obtained before the final optimizations steps had the system been properly calibrated with a reference cell. The efficiency increase upon switching to FTO is also clearly evident. ....	103
Figure C.2 Temperature Effects on ITO Sheet Resistance The thermal stability of ITO is quite poor, as is apparent from the above figure, which makes it a very poor candidate for GSC preparation. The GSC preparation requires temperatures >500°C and at this high temperature the sheet resistance of the ITO has already more than tripled. ....	104
Figure C.3 IV Curves - GSC Avg with Sputtered Pt CE vs Dyesol Pt Paste By employing a Pt paste from a different vendor, a GSC with the new Pt paste as the counter electrode gives an illuminated IV response almost within the 99% confidence intervals for five averaged GSC IV responses.....	105
Figure C.4 SEM Image FTO Surface Roughness.....	106
Figure C.5 Poor TiCl <sub>4</sub> Solution Effects on Photovoltaic Performance Additional double layer GSCs were fabricated using the optimized parameters except allowing the integrity of the TiCl <sub>4</sub> to be compromised. The criticalness of this solution's condition is apparent from the increased series resistances, decreased current densities, decreased fill factors , and decreased efficiencies. ....	107
Figure D.1 IV Curves - Casted AuNPSCs Photocurrent enhancements and reductions were observed for AuNPSCs that had the AuNPs deposited both by spin-casting and drop-	

casting. The inconsistencies are attributed to the poor precision of these deposition techniques which comes from variations in the dewetting processes. ....	109
Figure D.2 FESEM of AuNP Functionalization – High & Low NP Densities Higher surface coverages gave well dispersed NPs in areas of the substrate but a majority of the NPs formed large aggregates. Even lower surface coverages of ~5% gave similar results but to a lesser extent than the higher coverages. ....	110
Figure D.3 FESEM AuNPs - 2 Hr Electrolyte Exposure (A) shows a low surface coverage sample (~1.6%). (B) shows the thermal fusion effects of the NPs. In (C) no NPs remained with hardly any remnants of the particles either, which was expected since after a 30 min. exposure there was little NP remnants left. ....	111
Figure D.4 IPCE - AuNPSCs (IV Curves Tested At Different Light Intensities) IPCE for the AuNPSCs that were tested at different light intensities again shows a similar trend to previous IPCE curves in that the low surface coverage devices show reduced IPCE. ....	111
Figure D.5 AuNPSCs $J_{SC}$ and $V_{OC}$ Illumination on/off tests Certain AuNPSCs were subjected to chronoamperometry and chronopotentiometry in order to test stability. The devices were stable during the testing period and also from the choronoamperogram it is evident that the devices are not diffusion limited. ....	112

## List of Tables

Table 2.1 Major Solar Simulator Components .....	29
Table 2.2 75 W Lamp % Differences vs Wavelength .....	39
Table 2.3 Effect of Mistaken Irradiance on Reference Cell Characteristics.....	43
Table 2.4 Si Reference Cell Calibrated Values vs Measured Values .....	44
Table 3.1 Photovoltaic Characteristics - Optimized Double & Single Layer GSCs .....	53
Table 3.2 Photovoltaic Properties Before & After Key Optimizations .....	54
Table 3.3 Electron Lifetimes in Photoanode.....	68
Table 4.1 Photovoltaic Properties AuNPSCs - Enhanced vs Non-Enhanced.....	73
Table B.1 Certified Values for Si Reference Parameters .....	100
Table C.1 Single Layer GSCs Statistics .....	102
Table C.2 Photovoltaic Characteristics - GSC Avg with Sputtered Pt CE vs Dyesol Pt Paste ..	105
Table C.3 Photovoltaic Parameters - Pristine TiCl <sub>4</sub> vs Poor TiCl <sub>4</sub> .....	107

## **Acknowledgements**

First and foremost, I would like to thank God, for without Him nothing would be possible. I would like to thank all of my family, especially my parents, Donald & Theresa Essner, as well as my friends, for all of their support and encouragement along the way. A special thanks needs to go out to my girlfriend, Kati Kremer, who has always believed in me and has stood by my side through the thick of it. I would also like to thank my advisor, Dr. Jun Li, for all of his guidance and support throughout my graduate career at Kansas State University and I'd like to thank my fellow lab mates and classmates for all their support, as well as for their friendship.

## **Dedication**

This thesis is dedicated to Donald & Theresa Essner. Without their guidance and continuous support, I would not be where I am nor would I be the man I am today. They never, once, stopped believing in me, they continually reminded me of my potential, and they would not let my ADHD get the best of me. Their dedication, perseverance, and patience in raising me is made visible through this document. I thank you mom and dad for all that you have done and continue to do for me; a son could not ask for better parents. You both are truly examples to live by.

## **Chapter 1 - I Saw the Light!**

Energy crisis; Global warming; these are two phrases that more often than not get tossed as if no stock should be taken into the graveness of their meanings. Both issues, which are actually interconnected, are very real and require immediate attention. Ever since the 1970's oil embargo, the interests in alternate sources of energy especially research into solar and wind energies have steadily increased.<sup>1</sup> During the past decade, especially the latter half, with the economic crises and rise of oil prices, the dire need for an alternate energy source has become more and more apparent. This necessity has initiated floods of research towards harnessing a source worthy enough to replace the current king of energy; fossil fuels. The most commendable and promising source for fossil fuel replacement is the inward solar flux of radiation from the sun onto the earth's surface. All these matters will be addressed in detail below.

### **Energy Crisis & Global Warming**

For about the past century fossil fuels have been the main staple to satisfy the world's energy consumption. It wasn't until recent that the severe negative side effects of combusting fossil fuels became evident. Two critical issues have arisen; the effects of the by-products of fossil fuel synthesis and combustion and the short supply remaining of the non-renewable fuels. The synthesis and combustion of fossil fuels generates massive amounts of CO<sub>2</sub> which can have detrimental effects on the atmospheric conditions of the earth. The atmosphere itself is already composed of the greenhouse gases (O<sub>3</sub>, H<sub>2</sub>O, O<sub>2</sub>, and CO<sub>2</sub>) which help regulate the incident solar energy and the escaping thermal energy through absorption, reflection, and re-radiation. The excess generation of CO<sub>2</sub> could have profound effects on the surface climate of the earth including global warming, severe weather pattern shifts, and more intense seasonal conditions. On top of this, the amount of fossil fuels left for garnering is dwindling, which means an alternate source needs to be found as quickly as possible to avoid further atmospheric effects and/or the depletion of the current primary energy source.

Due to the exponential increase of the earth's population and economic rise of many undeveloped countries, the world energy consumption is on roughly a linear rise (Figure 1.2). In 2004 the total world energy consumption was up to  $4.7 \times 10^{20}$  J (15 TW) and in 2008 it had risen to  $\sim 5.0 \times 10^{20}$  J (16 TW). It is projected that by 2050 the worldly power consumption will rise

up over 26 TW.<sup>2</sup> Figure 1.2 shows two plots; a timeline (1965 to 2005) of world energy consumption broken down into the top sources (left) and a linear bar graph of all sources showing their % make up of the total consumption (right). Both plots show that non-renewable sources (nuclear & fossil fuels – oil, coal, and natural gas) constitute well over 90% of the total energy consumed with less than 10% coming from the renewable sources. Among the renewable sources, solar and wind show the most potential. Solar energy converted into electrical energy through photovoltaic processes, which is one of the very promising renewable energy technologies (discussed later), does not even comprise a thousandth.

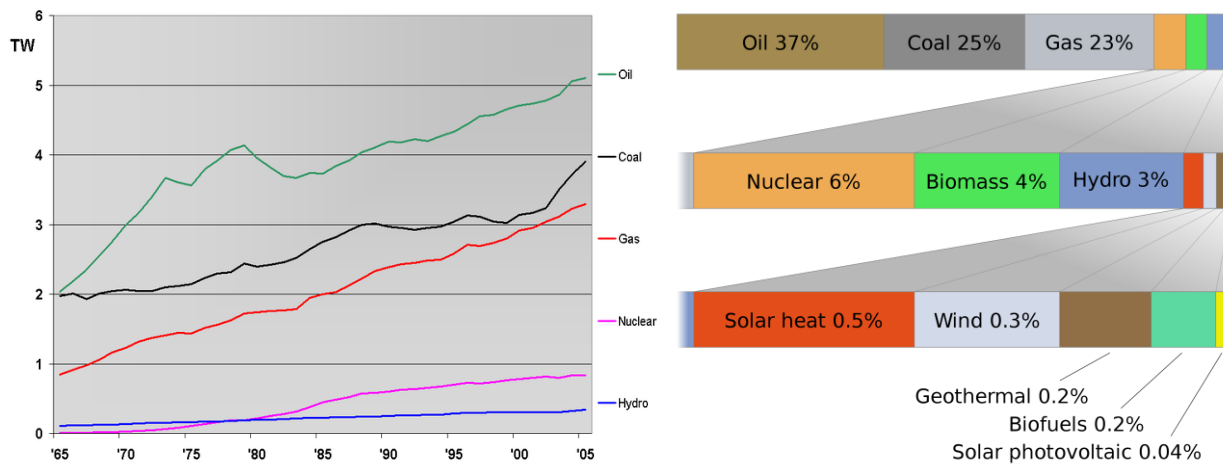


**Figure 1.1 World Energy Consumption Timeline<sup>3</sup> & 2006 Energy Source Usage (%)<sup>4</sup>**

The left image shows a timeline from 1965 to 2005 of the continually increasing power consumption of fuels with fossil fuels being the major contributors. (Used with permission from ref. 3. Copyright © 2007 Frank V. Mierlo) The right image shows a linear bar graph of the percentage of fuels consumed in 2006 again showing that fossil fuels (non-renewable sources) comprise over 90% while renewable sources (solar, wind) constitute <1%. (Used with permission from ref. 4. Copyright © 2008 Omegatron)

### *Necessity for Sustainability*

With renewable sources only composing such a small percentage and the depletion of fossil fuels approaching quickly, a push towards an efficient, sustainable energy source is vital. It is estimated that there is only 57 ZJ ( $10^{21}$ ) of energy left on earth from various oil sources, with a low estimate of 8 ZJ and a high estimate of 110 ZJ. The energy amount and percentage breakdown of the various oil sources for the median estimate are shown in Figure 1.2.

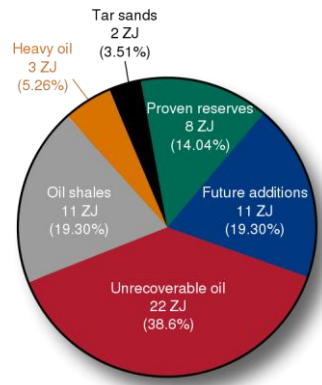


**Figure 1.2 Remaining Oil Energy<sup>5</sup>**

**The estimated energy amounts and percentages of the various oil sources are shown above. A median estimate of 57 ZJ of oil energy is believed to remain on earth with 8 ZJ as a low end estimate and 110 ZJ as a high end estimate. For the median estimate with an increasing consumption rate of 2 EJ/year the oil supplies would run out in ~150 years. (Used with permission from ref. 5. Copyright © 2008 Frank van Mierlo)**

If the current energy consumption rate (0.18 ZJ/year) would level out (no longer increase linearly), then the oil sources would run out in 44 years (low), 316 (median), or 611 years (high). Since it is highly unlikely that constant consumption would occur anytime soon, it can be assumed that the yearly consumption rate will still increase by 2 EJ/year, meaning the oil supply would run out in ~20 years (low), ~150 years (median), or ~240 years (high). With the depletion of the fossil fuels potentially occurring within the next century, the discovery and implementation of an efficient, sustainable energy source needs to take place. As mentioned earlier solar energy is one of the most promising candidates of the possible renewable sources. (Figure 1.3)

### ***Alternatives to Present Energy Economy***

The sun deposits  $4.3 \times 10^{20}$  J of energy onto the earth in one hour which is more energy than mankind consumes in one year. Of the 174 PW that reaches the earth's outer atmosphere, 86 PW (equivalent to  $2.71 \times 10^{24}$  J/year  $\rightarrow$  5,000x the energy used) still reaches the earth's surface; the other 88 PW being absorbed or reflected by the atmosphere (Figure 2.1). Figure 1.3 displays some of the renewable sources with their amount of potentially harvestable power and compares them to the power consumed. Using a combination of the renewable sources would provide more than enough energy for sustainability but solar alone could also accomplish this. If

only 0.16% of the earth's surface was covered with solar energy conversion systems that were at least 10% efficient, the energy requirements would be satisfied.

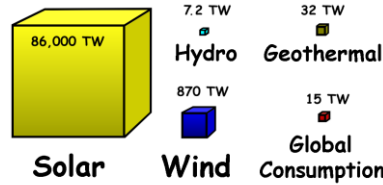


**Figure 1.3 Total Possible Available Power of Renewable Sources<sup>6</sup>**

**Of all the renewable sources, solar is one of the more promising to replace fossil fuels due to the 86 PW of power that is supplied to the Earth's surface. This 86 PW is more than 5000x the current global consumption of 15 TW. (Used with permission from ref. 6.**

**Copyright © 2008 Delphi234, based on work by Frank v. Mierlo)**

### **Solar Energy Harvesting**

The primary solar energy conversion systems employed to harvest the incident solar energy are photovoltaic devices. These photovoltaic devices, also known as solar cells, capture and convert the incident solar radiation into electrical energy through the generation and collection of electron-hole pairs. In the past this has been accomplished by semiconductor materials sandwiched together into a p-n junction (discussed later), but due to high materials and fabrication costs, alternative means are being explored. Recently, emerging dye-sensitized/quantum dot sensitized and polymer/organic based devices with their low materials costs and relatively high efficiencies are showing much promise.<sup>7-12</sup>

#### ***Photovoltaic Generations (1<sup>st</sup>, 2<sup>nd</sup>, & 3<sup>rd</sup>)***

With these emerging photovoltaic technologies, the various devices have been categorized into solar cell generations; 1<sup>st</sup>, 2<sup>nd</sup>, & 3<sup>rd</sup> (Figure 1.4).

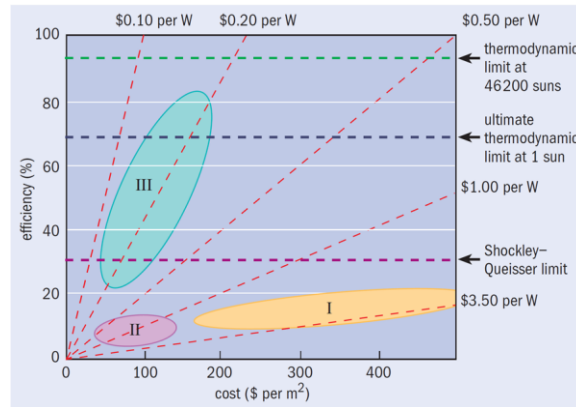


**Figure 1.4 Solar Cell Generations - Cost vs. Efficiency<sup>13-15</sup>**

**Photovoltaic devices are segregated into three generations; 1<sup>st</sup>) Solid-state devices (mainly Si), 2<sup>nd</sup>) thin film devices, 3<sup>rd</sup>) Devices not in 1<sup>st</sup> & 2<sup>nd</sup> (3D hierarchical, organic/polymer devices, tandem cells, etc.). The 2<sup>nd</sup> generation was developed to circumvent the expensive 1<sup>st</sup> generation but both are limited by the Shockley-Queisser theoretical limit. The 3<sup>rd</sup> generation tackles both these issues with low cost, high efficiency devices that have the potential of being pushed above the thermodynamic limit by strategic device design. (Used with permission from ref. 13. Copyright © 2007 IOP Publishing)**

The first generation mainly consists of the silicon-based family of solar cells (monocrystalline/polycrystalline) which constitute most of the photovoltaic market but also has had single p-n semiconductor junction based solar cells grouped within as well. The major downfall to the first generation is the high-costs associated with the production of high efficiency devices. Figure 1.4 shows that for about 5% increase in efficiency (~10% to ~15%), the cost per m<sup>2</sup> would double (\$200/m<sup>2</sup> to \$400/m<sup>2</sup>). By employing thin film technology, the cell thickness can be reduced from hundreds of microns thick down to just a few microns, which reduces the high costs of the first generation cells. These thin film cells make up the 2<sup>nd</sup> generation cells. The biggest problem with the 2<sup>nd</sup> generation is due to the reduced materials costs (thinner cells), there is less light-absorbing material to generate photocurrent leading to lowered efficiencies. The downfall to the 1<sup>st</sup> and 2<sup>nd</sup> generations is that since their operation is based on a single p-n junction, they are limited by their Shockley-Queisser theoretical limits. The 3<sup>rd</sup> generation solar cells, which currently consist of any cells that aren't grouped into the 1<sup>st</sup> and 2<sup>nd</sup> generations, try to circumvent the high costs/low efficiencies and some are not limited by the Shockley-Queisser limit. Since the 3<sup>rd</sup> generation encompasses all those cells that don't fit into the 1<sup>st</sup> and 2<sup>nd</sup> it

involves many different technologies such as tandem cells<sup>14-17</sup>, 3D hierarchical structured cells<sup>9, 18-20</sup>, dye/quantum dot sensitized cells<sup>7, 8, 20-24</sup>, polymer/organic cells<sup>12, 25-30</sup>, plasmon enhanced cells<sup>31-35</sup>, etc. Figure 1.5 gives the best research efficiencies of the 1<sup>st</sup>, 2<sup>nd</sup> and some 3<sup>rd</sup> generation devices.

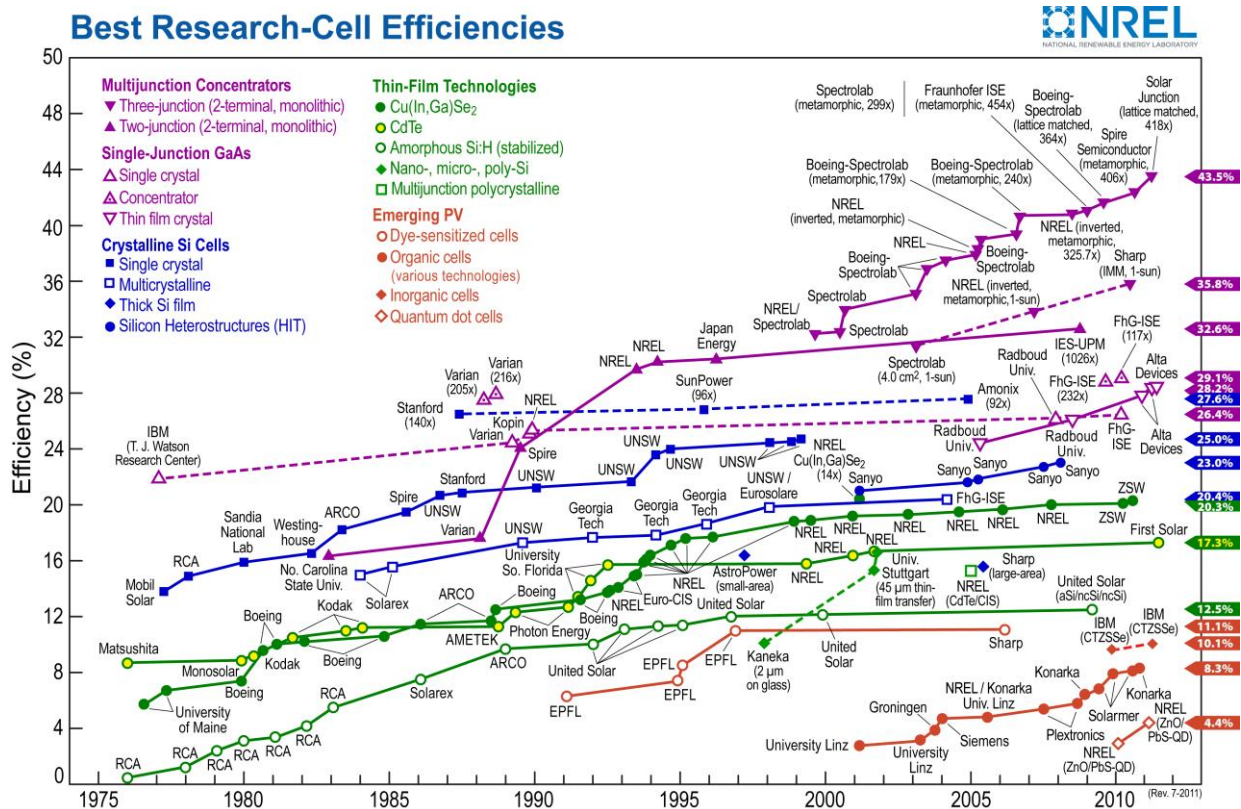


Figure 1.5 Best Efficiencies Obtained for Research Photovoltaic Cells<sup>36</sup>

Since 1975, as the generations of photovoltaics have evolved, the best obtained efficiencies for research cells have steadily been climbing with 1<sup>st</sup> generation Si solar cells approaching the Shockley-Queisser limit and 3<sup>rd</sup> generation multijunction (tandem) devices reaching upwards of 43%. (Used with permission from ref. 36, Updated image came directly from author. Copyright © 2011 NREL)

It clearly shows that the 2<sup>nd</sup> generation thin film cells (Si and other semiconductors) are plagued by lower efficiencies than the 1<sup>st</sup> generation Si cells, while the 3<sup>rd</sup> generation multijunction devices have already been able to surpass the Shockley-Queisser limit for Si based devices (32%). While the efficiencies of these multijunction devices are high, their materials and fabrication are too expensive. The emerging photovoltaic devices (organic & dye sensitized)

show much promise due to their low costs, ease of fabrication, and relatively high efficiencies – up to 11% (despite being in their infancy). A brief overview of Si/thin film Si devices and dye-sensitized solar cells, as well as plasmon enhanced devices, is given below.

## *Solid State Devices*

### *Device Basics and Operation*

The 1<sup>st</sup> and 2<sup>nd</sup> generation Si based photovoltaic devices will be grouped into one category deemed solid state devices. These solid state devices consist of a p-type semiconductor (B-doped Si → hole-rich) and an n-type semiconductor (P-doped Si → electron-rich) placed in contact to form a junction. Figure 1.6 shows a schematic of a solid state device.

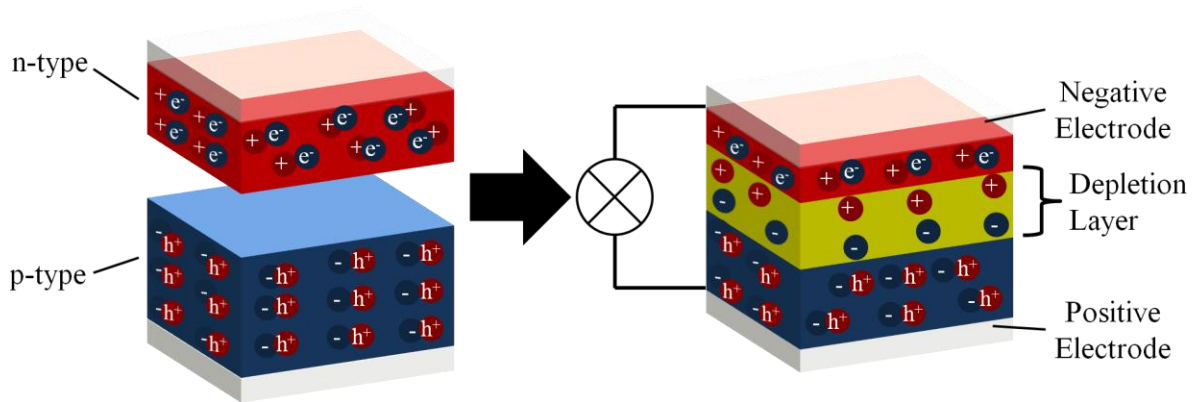


**Figure 1.6 Solid State Device Schematic**

**A solid state photovoltaic device consists of a n-type semiconductor placed in contact with a p-type semiconductor forming a p-n junction. When brought into contact, the excess charges in the materials diffuse across the semiconductor interface and combine with an opposing charge. This diffusion leads to the formation of a depletion layer in which excess negative charges are left in the p-type and excess positive charges are left in the n-type which gives rise to a built-in electric field.**

Upon placing these semiconductors in contact and without an external bias applied, an equilibrium between the excess holes and electrons is reached. The holes in the p-type semiconductor (in blue) diffuse across the semiconductor interface combining with an electron in the n-type (in red) and leaving a trapped electron in the p-type. The same process occurs in the n-type semiconductor; the electrons diffuse across the interface into the p-type, combining with holes, and leaving additional trapped holes in the n-type material. This diffusion leads to a

depletion layer in the device, which then gives rise to a built-in electric field. The built-in electric field at this interface will help separate and keep separated the generated electron-hole pairs. The interface of the semiconductors (p-type & n-type) is known as the p-n junction.

### ***P-N Junction of Photovoltaic Device***

Figure 1.7 below highlights the processes that occur at a p-n junction upon electromagnetic radiation. Upon absorption of a photon of appropriate energy, an electron is excited up to the conduction band (CB) making it a free carrier and leaving a hole in the valence band (VB), which can also freely move throughout the crystal lattice. If the charges are generated in the depletion layer (near the p-n junction) then due to the built-in electric field the generated majority carriers (electrons in n-type, holes in p-type) are quickly swept away due to opposition to the electric field. The minority carriers (holes in n-type, electrons in p-type) will diffuse across the semiconductor and ideally cross the p-n junction without recombining. Once across the junction the minority carrier becomes a majority carrier and will easily be swept away by the electric field. If the electron-hole pair is generated far from the built-in electric field or near a defect in the crystal (trap site), the chances of recombination drastically increase. The time to recombination is based upon the minority carrier lifetime. If the electron-hole pair is generated far enough from the depletion layer that the minority carrier can't diffuse to the built-in electric field before its lifetime is up, then it will recombine and no current can be produced due to this parasitic recombination.

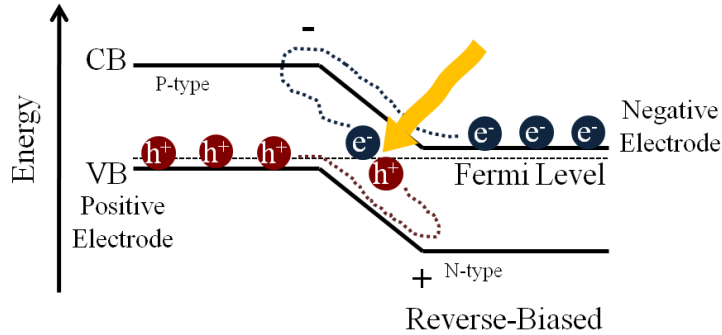


**Figure 1.7 PN Junction Operation**

**When subjected to a photon flux of appropriate energy, the photons are absorbed and an electron-hole pair is generated. With the help of the built-in electric field, the generated charges are swept away, separated and begin to diffuse towards the front and rear contacts. The generated electrons will diffuse towards the n-type region (negative electrode) and the generated holes towards the p-type region (positive electrode).**

### *Downfalls to Solid State Devices*

The downfall to both Si and thin film Si is that in order to minimize these parasitic recombinations and achieve high efficiency devices, high quality, expensive materials and fabrication techniques are required. By reducing the thickness of the device i.e. making a thin film cell the costs can be dramatically lessened but at expense of the efficiency. One way to circumvent this thin film loss is to incorporate metal nanoparticles to take advantage of their plasmonic properties (discussed in a latter section). Despite the reduction in costs, the thin film device fabrication is still an extensive process and the high quality materials can still be expensive. A cheaper, easy to fabricate alternative is the dye-sensitized solar cell.

### *Dye-Sensitized Devices*

Dye-sensitized solar cells (DSSCs) were pioneered over 20 years ago by Michael Grätzel with the debut of the benchmark “Grätzel cell”. Since then DSSCs have been able to reach efficiencies >11%.<sup>7, 8</sup>

### *Device Basics and Operation*

DSSCs make up and operation principles differ greatly from their solid state predecessors. Basic DSSCs consist of a semiconductor nanoparticle network sensitized with a visible light absorbing species with an interwoven electrolyte, all sandwiched between a transparent conducting oxide (TCO) electrode and a Pt thin film counter electrode (Figure 1.8). The heart of the device lies in the sensitized photoanode, where charge generation and separation occur as two distinct processes, which is what sets the DSSC apart from the solid state devices. In the solid state devices, the charge generation and separation occurs within the same material whereas in the DSSC, charge generation occurs within the dye and separation occurs at the dye/TiO<sub>2</sub> nanoparticle interface and the electrons flow through the TiO<sub>2</sub> network while the holes are carried by redox mediators in the electrolyte solution.

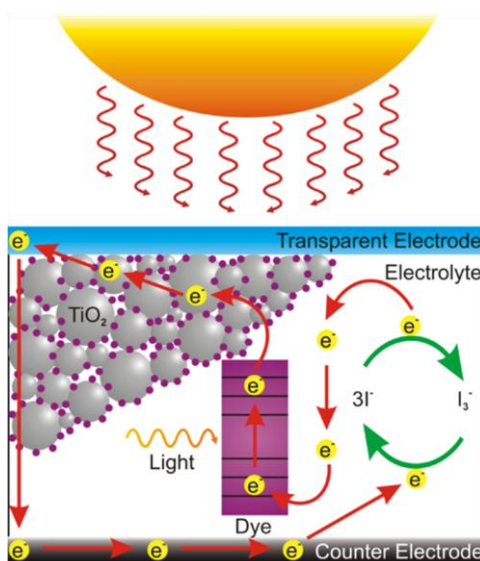


**Figure 1.8 DSSC Components & Operation**<sup>37</sup>

**A DSSC consists of a semiconductor sensitized with a visible light absorbing species (dye) sandwiched in between a transparent conductive electrode and a counter electrode with a redox couple filler to shuttle the charges to and from the CE and the dye/semiconductor interface. When the dye absorbs incident light, an electron is excited and can then be injected into the semiconductor, where it percolates through and is ideally collected to do work. (Modified from ref. 37. Copyright © 2009 M. R. Jones)**

Upon light irradiance of appropriate energy, an electron of the dye is excited from the highest occupied molecular orbital (HOMO) to one of the higher energy unoccupied orbitals.

The electron is then injected into the  $\text{TiO}_2$  where it percolates its way to the transparent electrode. Once collected, the electron flows through the external circuit, does work, and flows to the Pt counter electrode. At the CE, the electron reduces the electrolyte ( $\text{I}_3^-$ ). The reduced species ( $3\text{I}^-$ ), acting as charge shuttle, then diffuses through the electrolyte solvent towards the photoanode. Upon arrival at the dye of the photoanode, the  $3\text{I}^-$  is oxidized back to  $\text{I}_3^-$ , reducing the previously oxidized dye and regenerating it for another cycle.

### ***Improving Downfall to DSSCs***

The DSSC can be fabricated with relative ease and its costs are minimal but the device efficiency is still extremely low when compared to the commercially available Si cells. Various approaches to improving the efficiency of the DSSC, such as 3D counter electrodes<sup>38-43</sup>, more stable redox shuttles<sup>44-48</sup>, and higher absorption photoanodes<sup>49-55</sup> are underway. Increasing the photon absorption of the photoanode is critical because the more photons absorbed, the more potential electrons to be collected, and the higher the possible photocurrent. One method to enhance the photoanode absorption that is heavily explored is improvement of the sensitizer. Dyes with wide absorption bands, spanning the whole visible region and even reaching down into the UV region and up into the IR region, are currently being developed.<sup>49-55</sup> Another way to increase the photoanode absorption which could potentially lead to enhanced device efficiencies is to incorporate metallic nanoparticles that display plasmonic properties.

### ***Incorporation of Metallic Nanoparticles***

These metallic nanoparticles that display plasmonic properties (surface plasmon resonance) could be incorporated into various parts of the photovoltaic devices to try to increase the light harvesting characteristics of the devices. The surface plasmon resonance of the metallic nanoparticle should increase the generated photocurrent through enhanced light guiding, trapping, or absorption.

### ***Surface Plasmon Resonances***

Surface plasmon resonances are the collective oscillation of electrons within a metal nanoparticle (Figure 1.9) When the size of the nanoparticle is much smaller than the wavelength of incident light, at any given point the nanoparticle experiences a relatively uniform electric field. This “uniform” electric field pushes the electrons all together to one side of the particle.

The movement of conduction electrons upon light excitation leads to a buildup of polarization charges on the particles surface which acts as a restoring force, allowing a resonance to occur at a particular frequency, which is known as the surface plasmon resonance frequency.<sup>56, 57</sup>

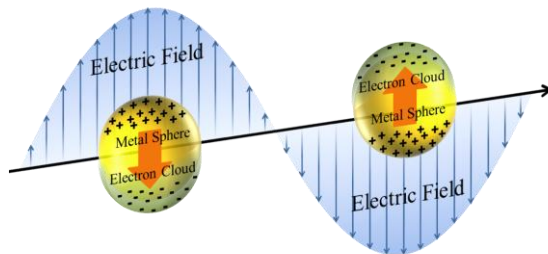


**Figure 1.9 Surface Plasmon Resonance Schematic<sup>58</sup>**

**When the size of a particle is reduced to sub wavelength dimensions, the particle will experience a uniform electric field as incident light interacts with the particle. This uniform electric field causes the charges in the particle to oscillate with the electric field. This oscillation acts a restoring force leading to resonance at a particular frequency. This resonance can be exploited for enhancing photovoltaics. (Image adapted from ref. 58.)**

***Light Trapping Geometries***

Incident light near the surface plasmon resonance frequency is either strongly scattered or absorbed depending on the particle size. This property can be exploited in solar cells as a light trapping mechanism. Various light trapping geometries can be employed depending on the solar cell design and the desired effect (Figure 1.10)

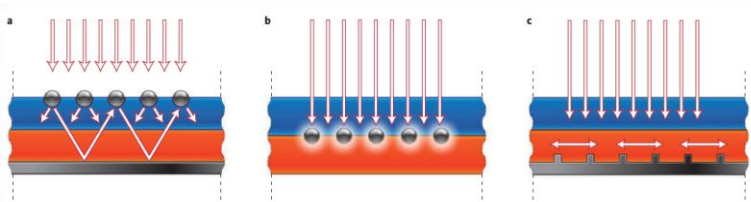


**Figure 1.10 Light Trapping Geometries<sup>56</sup>**

**Depending on the size and geometry of the particle, the particle can be employed in different geometrical setups to achieve various light trapping. Incident light can be scattered (far left), concentrated (center), and/or redirected (far right). (Used with permission from ref. 56. Copyright © 2010 Nature Publishing Group)**

There are three possible light trapping geometries for solar cell applications; light scatterers (1.10a), light concentrators (1.10b), and light redirectors (1.10c). When a metal

nanoparticle that exhibits surface plasmons is placed in a homogeneous material, then incident light will be scattered away from the particle (nearly) symmetrically. If metal nanoparticles of appropriate size ( $>100$  nm) are placed at the semiconductor/glass interface as in Figure 1.10a the incident light will preferentially scatter into the material with a higher permittivity; in this case into the semiconductor.<sup>56, 59</sup> This increases the path length of the light as it travels through the device, increasing the chance of complete absorption and also allowing the thickness of the photoactive material to be decreased. If a reflective back contact is employed such as a Pt CE and the light is not absorbed on the first pass, then as it reflects toward the surface the path length is additionally increased. With an appropriate surface coverage of nanoparticles, the light will essentially be trapped inside the device until it can be absorbed.

When particles of smaller size ( $<100$ nm) are placed at the interface of two semiconductors, such as a p-n junction, the particles will no longer scatter the light but will concentrate it (Figure 1.10b) Upon excitation, a large electric field enhancement is present around the particle (see Figure 4.3). The nanoparticle will act as an antenna for the incident light, storing energy in the localized surface plasmon which will lead to increased absorption by the surrounding semiconductor.<sup>56</sup>

Another way of trapping the light inside the cell besides using the first geometry and a reflective back contact is to incorporate metallic nanostructures on the back contact (Figure 1.10c). Using this geometry, incident light is converted into a surface plasmon polariton (photon coupled to surface plasmon) which is an electromagnetic wave traveling along the interface between the back contact and the absorber.<sup>56</sup> Surface plasmon polaritons excited at this interface can effectively trap and guide light into the semiconductor layer; the incident light is rotated by  $90^\circ$  and re-directed along the lateral direction of the semiconductor layer. The potential path length that the light could travel can be increased by upwards of 1000x due to device thicknesses being on the order of a few microns and device areas being on the order of centimeters.

### ***Applications***

As discussed above, the materials costs of Si based devices can be drastically reduced by employing thin film technology but the device efficiency is also reduced. One way to enhance the efficiency without increasing the materials cost is to incorporate metallic nanoparticles using the geometries discussed above. The surface plasmon resonance of the nanoparticle should

enhance the photocurrent thereby enhancing the overall efficiency. Ag nanoparticles have already been shown to increase photocurrent generation when incorporated into thin film devices.<sup>35, 60, 61</sup> Since DSSCs are a cheaper alternative to the solid state devices but are plagued with lower efficiencies, this same concept of metallic nanoparticle incorporation can be applied to the DSSCs to enhance the photocurrent and in turn the efficiency; Ag & Au nanoparticles have also been shown to enhance the photocurrents and efficiencies for DSSCs but are very sensitive to device design.<sup>31, 32, 34, 62-64</sup> Recently in our lab, Au nanoparticles (AuNPs) were incorporated into DSSCs at the FTO/TiO<sub>2</sub> interface showing potential photocurrent enhancements upwards of 30% and efficiency enhancements upwards of 20%.

### **Photovoltaic Device Characterizations**

With all the discussion of photocurrents and efficiencies, without a further understanding of what these parameters actually mean, then the numbers don't really have much significance. In order to characterize photovoltaic devices (PVDs) and arrive at these parameters, a calibrated solar simulator is required that is capable of producing the standardized intensity of 1 sun (100mW/cm<sup>2</sup>). The characterization techniques and how to arrive at the critical parameters that characterize PVDs will be described below. It should be noted that none of the graphs in the remainder of this chapter are actual data; all the graphs are schematic figures for the ease of discussion.

#### ***IV Curves (Dark & Illuminated)***

The primary means for characterizing PVDs is the collection of the dark & illuminated IV curves. For these measurements, the voltage is swept from negative to positive (approx. -0.2V to 0.75V depending on device) and the resultant current response of the device is monitored. The dark curve will be further discussed below. The critical parameters that can be extracted from the illuminated curve are the short circuit current density ( $J_{SC}$ ), open circuit voltage ( $V_{OC}$ ), fill factor (FF), efficiency ( $\eta$ ), shunt resistance ( $R_{SH}$ ), and series resistance ( $R_S$ ). Schematic dark & light IV curves are given below in Figure 1.11.

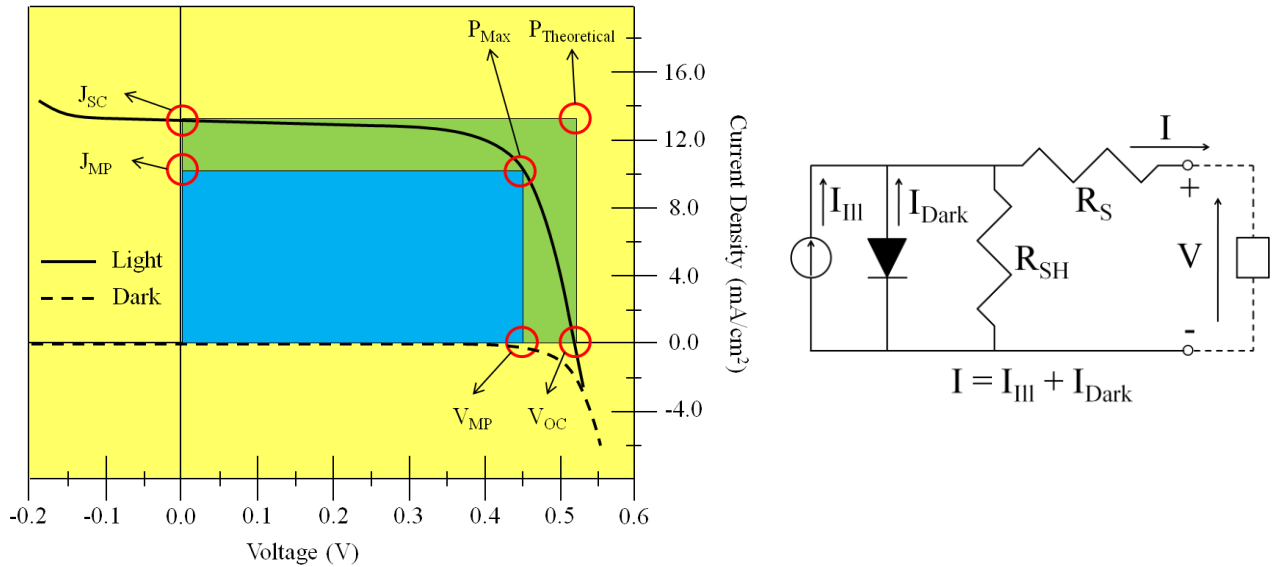


**Figure 1.11 Schematic Dark & Illuminated IV Curves with Equivalent Circuit Model**

**Displayed on the schematic IV curve are the short circuit current density ( $J_{SC}$ ), open circuit voltage ( $V_{OC}$ ), theoretical power ( $P_{Theoretical}$ ), current density at the maximum power output ( $J_{MP}$ ), voltage at the maximum power output ( $V_{OC}$ ), and the maximum power output ( $P_{max}$ ) of the device. The photovoltaic device can be modeled by the simple equivalent circuit shown on the right.**

The short circuit current density occurs when the voltage on the device is zero and it is the maximum possible current that the cell can generate. In contrast, the open circuit voltage occurs when the current flow through the device is zero and it is the maximum obtainable voltage of the cell. Before discussing the fill factor and efficiencies, the resistances of the device need to be mentioned; the shunt resistance arises from the lack of alternate current pathways (power losses) in the device and the series resistance arises from the combined interfacial charge transfer resistances. Ideally the shunt resistance is large, meaning very little power losses and the series resistance is low, meaning very little resistance to charge transport through the device. These resistances can be approximated from the slopes of the IV curve; the series resistance is the inverse of the slope of the IV curve around the  $V_{OC}$  and the shunt resistance is the inverse of the slope of the IV curve around the  $J_{SC}$ . It should be noted that if the shunt resistance is too low, then the photovoltage will decrease and if the series resistance is too high, the photocurrent will decrease. As just mentioned, in the ideal case, the shunt resistance is high (zero slope near  $J_{SC}$ )

and the series resistance is low (large slope,  $\infty$ , near  $V_{OC}$ ). This case would lead to the ideal IV curve, which is the green box in Figure 1.11. The IV responses, both light and dark, can be modeled to an equivalent circuit which is shown on the right side of Figure 1.11. Under dark conditions, the photovoltaic device behaves just like a diode displaying a current  $I_{Dark}$ . Under illumination, the device generates current labeled  $I_{Ill}$ , which is modeled as an additional component (current source) in the circuit model. The total current produced,  $I$ , by the device is then equal to  $I_{Dark} + I_{Ill} + I_{SH}$ . Again in the ideal case, the shunt resistance is near  $\infty$  and the series resistance is near 0, resulting  $I \approx I_{Dark} + I_{Ill}$ . This is also apparent in the circuit model. If  $R_S$  is large, then there will be a large resistance to the flow of electrons through the circuit thereby decreasing the total current,  $I$ , and the efficiency of the device. Likewise if  $R_{SH}$  is too small, then it provides an alternate current path for the electrons to follow which would result in a voltage drop across the circuit (lower photovoltage) and again decreased efficiencies.

Some other parameters shown on the IV curve above are the current density at the maximum power ( $J_{MP}$ ), the photovoltage at the maximum power ( $V_{MP}$ ), the maximum power ( $P_{max}$ ), and the theoretical power ( $P_{theo}$ ). In order to obtain power values, the current and voltage are multiplied together, so to determine the maximum power of the device, the current and voltage values from the IV curve are multiplied together. The resultant values are then plotted vs. the original voltage values giving a curve such as the one in Figure 1.12 and the maximum power is extracted.

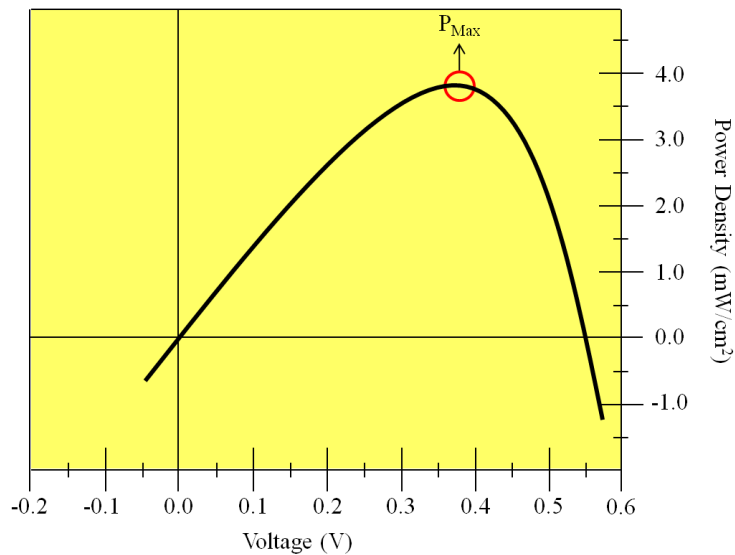


### Figure 1.12 Maximum Power Output Curve

The maximum power density output of the device can be determined by plotting the product of the current values and the voltage values vs. the original voltage values. A near parabolic curve should be obtained with the maximum of the curve being the maximum power output.

The theoretical power of the device is calculated by multiplying the short circuit density by the open voltage. Using all these parameters the fill factor can then be calculated with the formula given below:

$$FF = (J_{MP} \times V_{MP}) / (J_{SC} \times V_{OC}) = P_{max} / P_{Theoretical}$$

Therefore the fill factor of the device is a ratio of the maximum power output to the theoretical maximum power output which is essentially the ratio of the area of the blue square to the area of the green square.

The last parameter, and probably the most critical in terms of device characteristics, is the efficiency. The efficiency is calculated using the following formula:

$$\begin{aligned}\eta &= (FF \times J_{SC} \times V_{OC} / P_{in}) \times 100 \\ &= (J_{MP} \times V_{MP} / P_{in}) \times 100 \\ &= (P_{max} / P_{in}) \times 100\end{aligned}$$

The efficiency is the ratio of the maximum power output of the device to the power of the incident radiation.

The dark IV curve can be used to determine the cathodic current (back reaction) of the device. Extracting the current over a given voltage range, such as the one in the red box in Figure 1.13, and plotting its absolute value in log scale vs. the voltage will give a straight line as seen in insert.

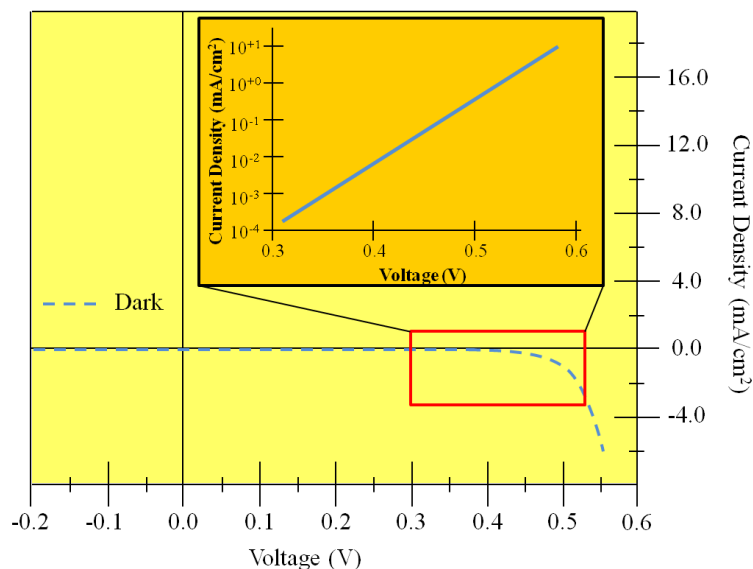


**Figure 1.13 Schematic Dark Back Reaction**

**Critical information regarding charge transport properties can be inferred from the IV response under dark conditions by plotting the dark current density in log scale over a specified voltage range.**

By comparing the slopes and the positions of the lines, various conclusions can be made about the cathodic current and the charge transport properties.<sup>10</sup>

### ***Incident Photon to Current Conversion Efficiency (IPCE)***

Another means to characterize the photovoltaic devices and also to probe the origin of the photocurrent is to measure the incident photon to current conversion efficiency (IPCE). The IPCE gives the percentage of photons at each wavelength that are actually converted into electrons (current). Therefore an IPCE of 50% indicates that for every one electron produced, two photons were required. Figure 1.14 shows a schematic IPCE graph of a DSSC. The IPCE is calculated with the following formula:

$$IPCE_{\lambda} = ((1240 \times J_{SC}) / (P_{in} \times \lambda)) \times 100$$

In order to determine the IPCE, the incident power ( $P_{in}$ ) at each wavelength is measured as well as the short circuit current and these values are plugged into the above equation. For a DSSC the IPCE peaks should correlate well with the UV-Vis peak absorption of the dye. A peak could also be present from the semiconductor such as the peak at ~350 nm in the schematic graph for  $TiO_2$ .

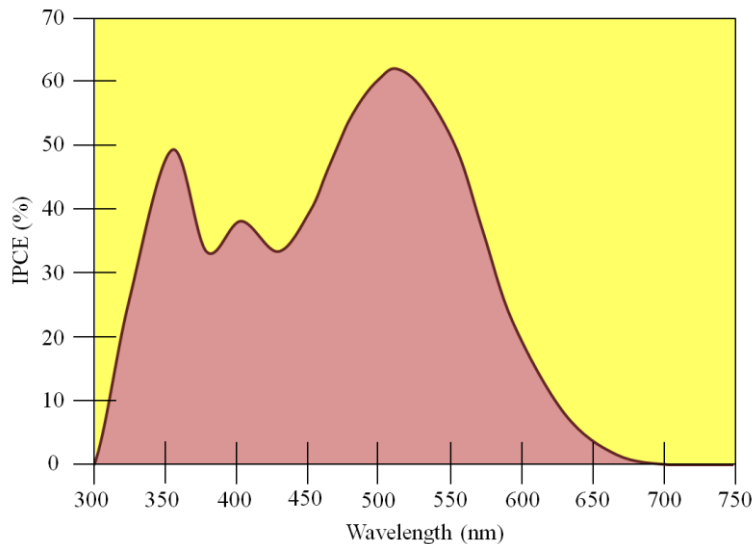


**Figure 1.14 Schematic IPCE**

**The incident photon to current conversion efficiency provides information into how efficiently the device converts photons into electrons (current) at each wavelength.**

**Characteristic UV-Vis peak absorption wavelengths ideally will correspond to the peak IPCE wavelengths.**

***Chronoamperometry/Chronopotentiometry (Illumination On/Off)***

Two powerful techniques that allow the measurement of device stability and charge transport properties are chronoamperometry and chronopotentiometry. For both techniques light is irradiated on the device for a given time period and is then interrupted (usually with a shutter) for a given period. For chronoamperometry, the short circuit current is monitored during these illumination on/off periods (Figure 1.15). The stability of the device's photocurrent is easily visualized from the chronoamperogram; if the measured current density during the on period remains virtually unchanged then the device is stable. The critical information that comes from chronoamperometry is whether or not the device is diffusion limited by the electrolyte. If the device is not diffusion limited (a flat steady photocurrent during the illumination on period) then the redox mediators are able to regenerate the dye at the same rate that it is being excited (oxidized). When the device is diffusion limited, a decay in photocurrent will be visible such as the first two illumination on periods in Figure 1.15. When the light is first turned on, the dye molecules are excited and start to inject electrons into the TiO<sub>2</sub>. These oxidized dye molecules are instantly regenerated by the redox couple surrounding the dye/nanoparticle network allowing

the dye molecules to again be excited and inject electrons. Since the limiting factor of the device is the diffusion of the electrolyte, as the electrolyte surrounding the photoanode is consumed, the oxidized dye molecules have to wait for more redox couple to diffuse to the photoanode before they can be regenerated. With the dye molecules being oxidized faster than the redox couple can reduce them all, many dye molecules remain in the oxidized state waiting for the electrolyte to diffuse to them. In other words as the redox couple diffuses to the photoanode, it will be instantly oxidized before it can penetrate deeply into the nanoparticle network leaving oxidized dye molecules in the oxidized state, rendering them useless. Over time as this process occurs, more and more dye molecules will be left in the oxidized state and therefore a decrease in photocurrent will be visible. Eventually, these processes will come to equilibrium and the photocurrent decay will level out. The critical information that can be extracted from this photocurrent decay is the apparent diffusion coefficient of the redox couple. The photocurrent decay can be plotted vs. the inverse square root of time ( $t^{-0.5}$ ) and if a linear dependence is present then the apparent diffusion coefficient of tri-iodide can be extracted from the slope of the linear portion (Figure 1.15).<sup>10</sup>

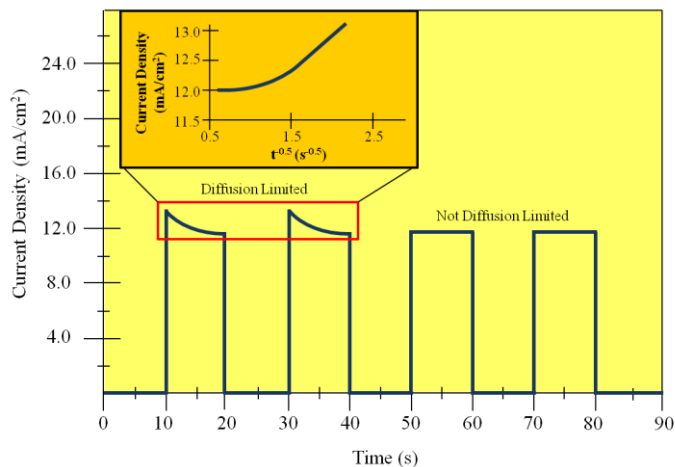


### Figure 1.15 Schematic Chronoamperogram

Chronoamperometry can provide three key pieces of information about the device; the stability of the device, whether it is limited by diffusion and if so what is the diffusion coefficient of the electrolyte. As the illumination is continually interrupted, a stable device will have the same current response during each illumination period. If the device is diffusion limited, a decay in the photocurrent is visible. This decay can be plotted vs. time<sup>0.5</sup> and the apparent diffusion coefficient can be extracted.

In chronopotentiometry, the open circuit voltage is monitored while the incident light is repeatedly interrupted for a given time period. Similar to chronoamperometry this technique can be used to determine the stability of the photovoltage of the device (Figure 1.16). The critical information that can be extracted from the chronopotentiogram again involves decay. Once the light is shut off the photovoltage will begin to decay rapidly and then slow as it approaches lower values. Using this decay, the lifetime of recombination of electrons with oxidized species in the electrolyte can be determined.<sup>65, 66</sup>

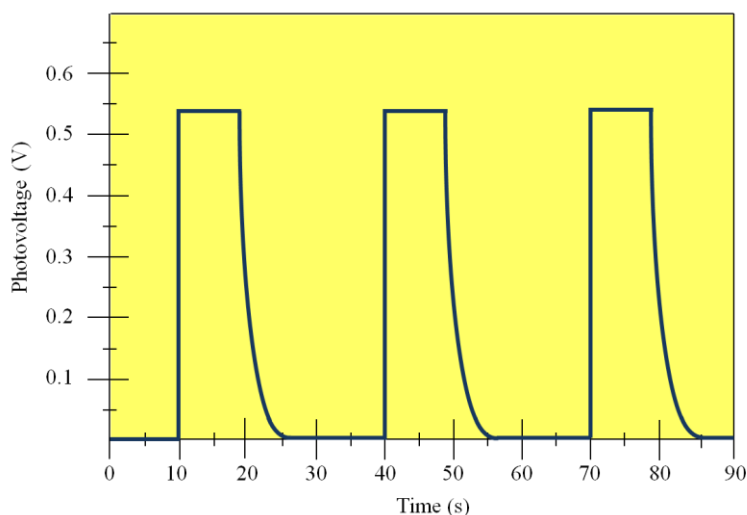


### Figure 1.16 Schematic Chronopotentiogram

Similar to chronoamperometry, chronopotentiometry can provide critical information into the device stability and charge transfer properties. The decay in the photovoltage can be used to determine the recombination lifetime of electrons in the electrolyte.

### ***Electrical Impedance Spectroscopy (EIS)***

Yet another way to probe the charge transport properties of photovoltaic devices is through electrical impedance spectroscopy (EIS). EIS can be performed under any bias (in the working range of the solar cell) and under any illumination conditions, but generally the conditions are open-circuit and  $100 \text{ mW/cm}^2$  illumination. In EIS, a harmonically modulated small-amplitude voltage is superimposed over the bias voltage (open-circuit) which allows a small AC current to flow.<sup>67</sup> The resultant current is monitored over a pre-determined frequency range and the impedance at each of the frequencies is calculated. A typical EIS spectra, called a Nyquist Plot (Figure 1.17), is a plot of the real impedance (x-axis) vs. the negative value of the imaginary impedance (y-axis). For DSSCs, three semicircles are usually present, although the 3<sup>rd</sup> semicircle (mHz region), which is the finite-Warburg impedance of the tri-iodide mass transport, can often vanish into the 2<sup>nd</sup> semicircle or just may not be visible due to the device thickness (if device is thin enough).<sup>9, 67</sup> The first semicircle, which represents the charge transfer resistance at the counter electrode, is usually in the kHz region and the 2<sup>nd</sup> semicircle, which represents the charge transfer resistances throughout the semiconductor and at the semiconductor/dye/electrolyte interfaces, is usually in the Hz region. The electron lifetimes in the semiconductor layer can be determined through EIS by plotting the data in a Bode phase plot and extracting the peak frequency of the 2<sup>nd</sup> semicircle (see Chapter 3 – Figure 3.13).

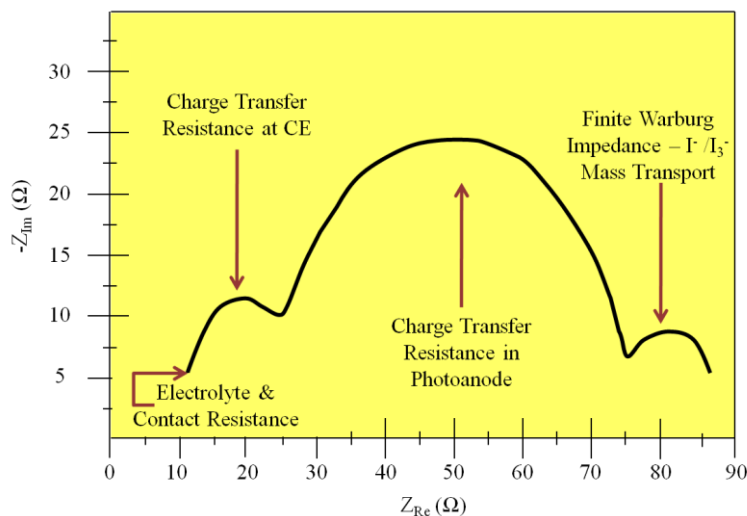


### Figure 1.17 Schematic EIS Spectra of DSSC

The Nyquist plot for a DSSC consists of three semicircles; the first one representing the charge transfer resistance at the CE (kHz region), the 2<sup>nd</sup> representing the charge transfer resistance in the photoanode (Hz region), and the third representing the finite Warburg impedance (mHz region). The semicircles will be shifted to the right (higher resistance) depending on the electrolyte and contact resistance. Plotting the data in a Bode phase plot and extracting the peak frequency of the 2<sup>nd</sup> semicircle will give information into the electron lifetime in the semiconductor film.

Using the appropriate software, the EIS data can be fit to an equivalent circuit (Figure 1.18).

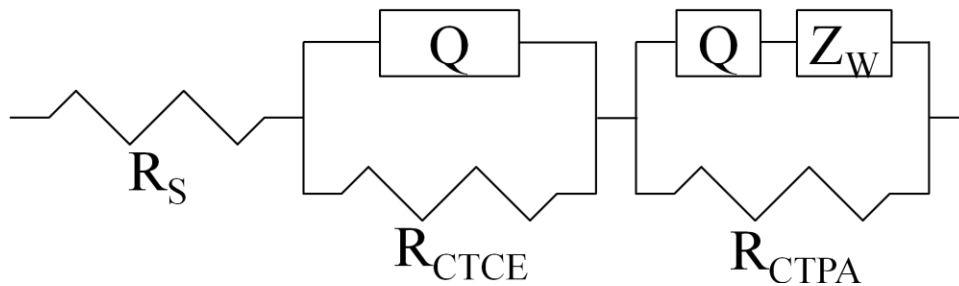


### Figure 1.18 DSSC Equivalent Circuit

The Nyquist plot of a DSSC can be modeled by a resistor and two RC circuits in series, with one RC circuit containing a finite-Warburg Impedance element,  $Z_W$ .  $R_S$  corresponds to the resistance of the electrolyte and the electric contacts. The two RC circuits ( $Q$  = capacitor,  $C$ , of variable capacitance) represent the charge transfer resistances at the counter electrode/electrolyte interface ( $R_{CTCE}$ ) and the dye/semiconductor/electrolyte (photoanode) interface ( $R_{CTPA}$ ) as well as the double layer capacitances at each interface ( $Q$ ).

The resistance that arises from the electrolyte and the electrical contacts can be represented by a simple resistor labeled,  $R_S$ . The first and second semicircles are represented by simple RC circuits (a resistor and a capacitance component) in series. Both the first and 2<sup>nd</sup> semicircles require a capacitor of variable capacitance, represented by  $Q$ . This component arises from double layer capacitance at both the CE/electrolyte (1<sup>st</sup> semicircle) and the photoanode (PA)/electrolyte (2<sup>nd</sup> semicircle) interfaces. The resistors for the 1<sup>st</sup> semicircle ( $R_{CTCE}$ ) and the 2<sup>nd</sup> semicircle ( $R_{CTPA}$ ) correspond to the charge transfer resistances at the respective interfaces;

1<sup>st</sup> semicircle  $\rightarrow R_{CTCE}$  = charge transfer resistance at the counter electrode and 2<sup>nd</sup> semicircle  $\rightarrow R_{CTPA}$  = charge transfer resistance at the photoanode.  $R_s$ ,  $R_{CTCE}$ , and  $R_{CTPA}$  together would give rise to the overall series resistance of the solar cell discussed above. In order to model the third semicircle, the  $Z_W$  component, which models the finite-Warburg impedance of the electrolyte mass transport, needs to be incorporated. If the circuit model did not contain the  $Z_W$  component then only two semi-circles would arise. Even with this component included, the 3<sup>rd</sup> semicircle is often not-visible due to the thin nature of the device (not diffusion limited) and/or the 2<sup>nd</sup> semicircle overlaps the 3<sup>rd</sup> i.e. the diffusion component is masked by the 2<sup>nd</sup> semicircle.<sup>9, 10, 67</sup>

## Chapter 2 - Solar Simulator System: Setup & Beam Alignment

As discussed in Chapter 1, the worldly consumption of energy is continually increasing and the means of this energy, fossil fuels, is slowly being depleted making the need for finding and implementing efficient and renewable sources of energy more and more pertinent. One of the promising approaches is to harness solar energy through solar cells by converting sunlight into electrical energy through photovoltaic processes. As previously stated, over 5.48 YJ ( $10^{24}$  Joules) of energy is irradiated onto the earth by the sun every year (eq. to 174 PW). Of this energy, only about half (~89 PW or 2.8 YJ/yr) reaches the earth's surface due to interactions (absorption, reflection, & re-radiation) with the atmosphere. (Figure 2.1)

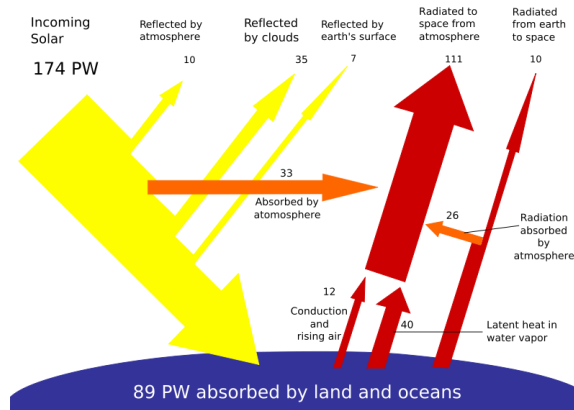


**Figure 2.1 Solar Energy Diagram<sup>68</sup>**

**Of the 174 PW of solar power that reaches the Earth's outer atmosphere, 89 PW is not reflected or absorbed by the atmosphere, allowing massive amounts of energy to be harvested through photovoltaic devices. (Used with permission from ref. 68. Copyright © 2008 Frank v. Mierlo)**

The absorption, reflection, & re-radiation of the incident solar radiation by the atmosphere (the greenhouse gases –  $O_3$ ,  $H_2O$ ,  $O_2$ , and  $CO_2$ ) gives rise to what is known as the solar radiation spectrum. (Figure 2.2)

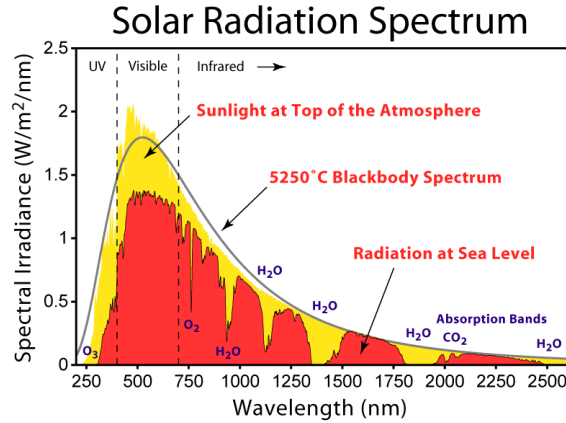


**Figure 2.2 Solar Radiation Spectrum<sup>69</sup>**

**The spectrum of the 174 PW of sunlight reaching the upper atmosphere is represented by the yellow (plus the orange) curves. The power reduction to 89 PW due to the atmosphere arises from the absorption of light (& reflection – not shown) from the greenhouse gases (O<sub>3</sub>, H<sub>2</sub>O, O<sub>2</sub>, and CO<sub>2</sub>) which produces the spectrum of solar radiation at sea level (orange). (Used with permission from ref. 69. Copyright © 2007 Robert A. Rohde)**

Since functioning solar cells, or panels, will be exposed to this spectrum once commercialized, when a new type of cell is developed its photovoltaic properties would ideally be tested using this same solar radiation but planetary climate conditions may not always be favorable to do so nor is the incident solar radiation onto the earth's surface always consistent. In order to circumvent these testing difficulties, systems were developed that would simulate the solar radiation spectrum and standard incident light intensities onto the atmosphere and onto earth's surface were established. These standardized light intensities are designated as Air Mass (AM) 0 (Figure 2.3 – Red Curve) and 1.5, for outside the atmosphere and onto the earth's surface respectively. The incident light onto the earth's surface has two distinctions; one is AM1.5D (Figure 2.3 – Green Curve) which only includes direct radiation and the other is AM1.5G (G stands for Global – Figure 2.3 – Blue Curve) which includes both direct and diffuse radiation. The solar intensity of AM1.5G sunlight is calculated to be  $\sim 970 \text{ W/m}^2$  but due to the variations in the intensity from changing atmospheric conditions, the value is standardized to  $1000 \text{ W/m}^2$ , although the most commonly used and reported values in literature are  $100 \text{ mW/cm}^2$  and 1 sun.<sup>70</sup> Besides a standardized light intensity, a standardized solar spectrum was also developed (Figure

2.3) and for testing purposes the spectrum & intensity are achieved through the use of an AM1.5G filter and a lamp, respectively.

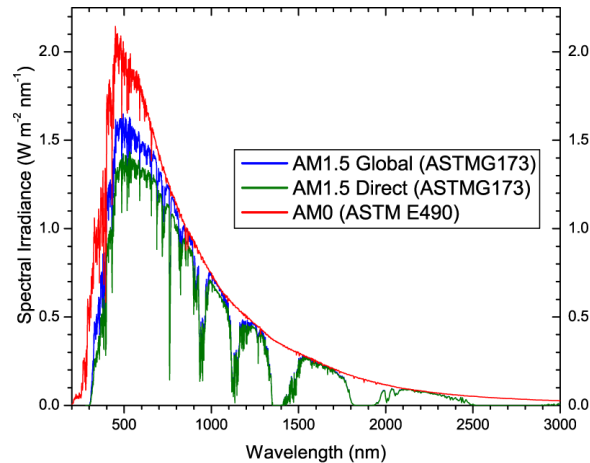


**Figure 2.3 Standard Solar Spectra**<sup>70</sup>

Shown in blue is the standard solar spectra, developed (AM1.5 Global) for solar simulation measurements. The spectrum represents the standard irradiance of  $100 \text{ mW/cm}^2$  used for photovoltaic characterizations. Also shown are the AM0 spectrum (solar radiation outside the atmosphere) and the AM1.5D spectrum (only includes the direct solar radiation onto the earth, not direct and diffuse – AM1.5G). (Used with permission from ref. 70. Copyright © Christiana Honsberg and Stuart Bowden, original work and data from SMARTS modeling program used at NREL)

A variety of solar radiation simulating systems have been developed, ranging from simple economical multi-piece units up to expensive elaborate single units that are capable of conducting all the measurements in situ. Prior to fabricating and studying any solar cells, a said solar simulator system needs to be established. After researching various companies' systems and receiving quotes, a solar simulator system from Newport Corporation was purchased, as well as some additional components from Thorlabs and Agilent Technologies. The solar simulator system will be described in detail in the next section.

### **Newport Solar Simulator System**

The Newport solar simulator that was purchased came with an assortment of instruments (Figure 2.4, Figure 2.5, & Table 2.1). The most important of these instruments will be described

below. A complete detailed list of the instruments can be found in Appendix A as well as a labeled schematic map.

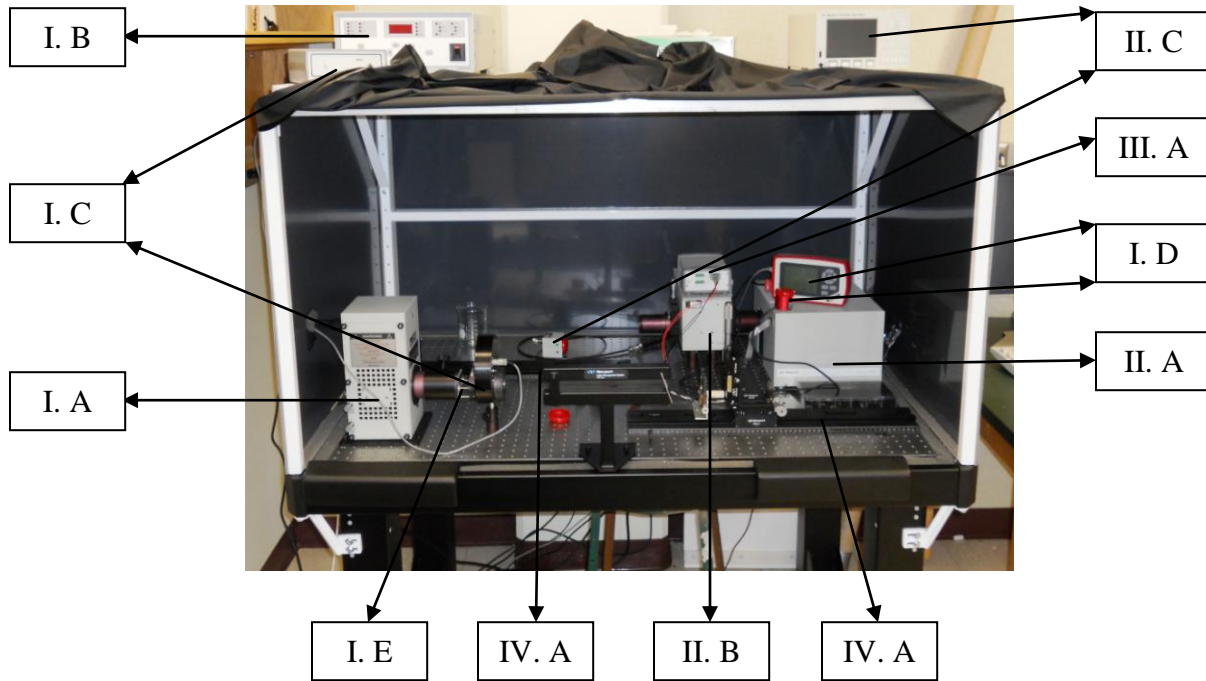


**Figure 2.4 Newport Solar Simulator**

Above is an actual picture of the solar simulator setup with the major components labeled.

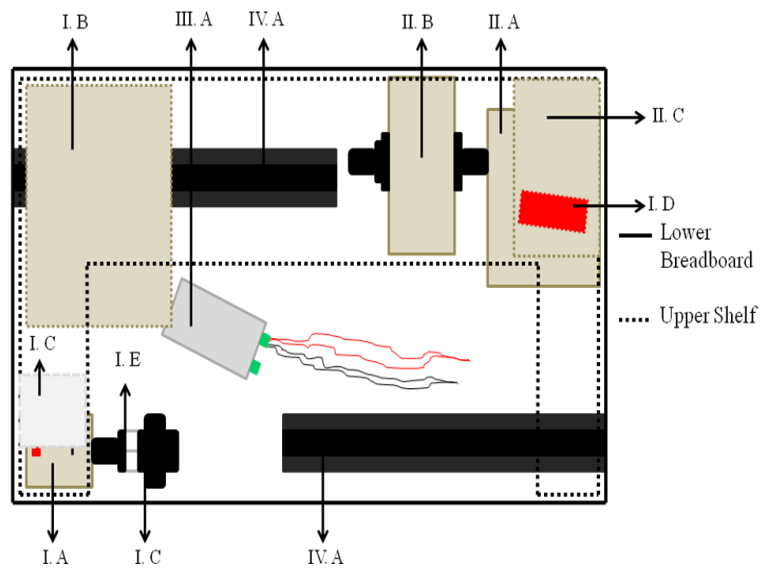


**Figure 2.5 Newport Solar Simulator Schematic (See Table 2.1)**

**Schematic of the overhead view of the major solar simulator components that are shown in Figure 2.4 as well as their locations on the supporting laser table.**

**Table 2.1 Major Solar Simulator Components**

<p><b>I. Broadband Light</b></p> <p>A. 300 W Xe OF Arc Lamp</p> <p>B. Lamp Power Supply</p> <p>C. Shutter and Power Supply</p> <p>D. Thorlabs Thermal Power Sensor &amp; Meter</p> <p>E. AM1.5G Filter</p>	<p><b>III. Electrochemical Characterization Instruments</b></p> <p>A. Agilent Source Measure Unit (SMU)</p> <p>B. CH Instruments Electrochemical Analyzer (not pictured)</p> <p>C. PARSTAT (not pictured)</p> <hr/> <p><b>IV. Misc</b></p> <p>A. 24” Optical Rail/Rail Carrier</p> <p>B. PV Measurements, Inc. 2 cm x 2 cm Calibrated Silicon Reference Cell (not pictured)</p>
<p><b>II. Monochromatic Light</b></p> <p>A. 75 W Xe OF Arc Lamp</p> <p>B. Motorized Monochromator</p> <p>C. Monochromatic Power Sensor &amp; Meter</p>	<p>*All components are from Newport Corporation unless otherwise stated</p>

The solar simulator system contains two light sources for producing the desired types of light for solar cell characterizations; one for broadband white light and another for monochromatic light. For the broadband light, a 300 W Xenon (Ozone Free) Arc Lamp and the AM1.5G Filter are used to provide 100mW/cm<sup>2</sup> of simulated solar radiation. A neutral density filter may also be utilized for lower light intensity measurements. The Thorlabs’ thermal power sensor & meter is used to verify that the incident light is of the desired intensity of 1 sun. Another important component of the broadband light setup is the motorized shutter, which enables the incident light to be interrupted during data collection to see how the device(s) behave from rapidly changing radiation conditions. The other light source (monochromatic) consists of a 75 W Xenon (Ozone Free) Arc Lamp, which produces white light, and a motorized monochromator that separates the white light into its monochromatic components, allowing the device’s behavior, such as incident

photon to current efficiency (IPCE), at each wavelength to be monitored. A different power sensor and meter (Newport), which factors into the power reading that the source is monochromatized, are employed for the measurement of the incident power at each selected wavelength. Being able to simulate the solar spectrum is ideal for testing photovoltaic devices, but without a means of monitoring the device's performance, the ability to simulate the solar spectrum has no meaning. In order to observe the photovoltaic device's performance, a source measure unit (Agilent) is utilized to record the device's current or voltage outputs under the various light conditions (dark & illuminated IV Curves). Also used to further characterize the devices (but not pictured in the schematic) are two different potentiostats; CH Instruments Electrochemical Analyzer (light on/off measurements) and PARSTAT Potentiostat (EIS). The Agilent SMU is capable of monitoring the current & voltage responses during light on/off measurements but due to poorer time resolution, the CH Instruments potentiostat is used. As stated before, the simulator consists of many other components but only the major pieces are highlighted here.

### **Solar Simulator System Setup and Calibration**

Once the simulator had been procured, it was assembled (as seen in Figure 2.4), the lamps were aligned and calibrated, and a quick guide was drafted up. Each lamp required a different alignment and calibration process, which will be discussed below, but for both lamps the uniformity of the incident beam was critical. Figure 2.6 schematically outlines possible beam irradiances from the lamp.

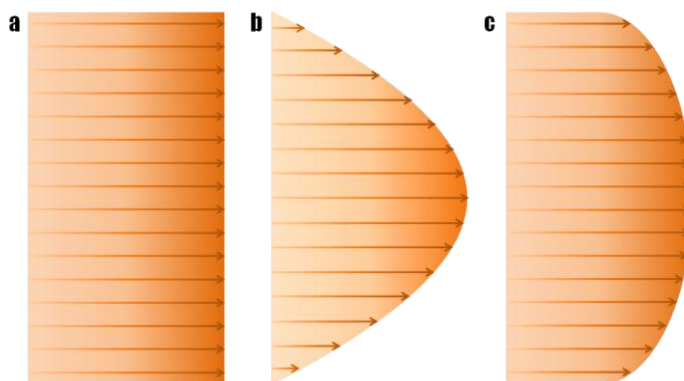


### Figure 2.6 Schematic of Possible Incident Lamp Beams

Ideally, an incident beam of light irradiating from the lamp that consisted of uniform power across the beam would be achieved as seen in A above. The reality is that the power of the incident beam is more conical shaped in its magnitude i.e. high power at the center with the power decreases away from the center (B). The goal is then to spread this uniformity outward across the beam as much as possible to give more of a dome shaped beam as shown in C above.

Ideally the incident radiation from the arc lamps would be of equal power across the entire beam face (perfectly uniform/collimated) as seen in Figure 2.6a. In reality though there is a power maximum at the center of the beam and the beam power drastically decreases with distance from the center (Figure 2.6b). The goal then is to align the lamps and mirrors in such a manner that the maximum power is expanded from a single point to a larger area as well as decrease the power drop off from the beam center (Figure 2.6c). In order to maximize this beam uniformity, four critical parameters had to be optimized; the position of the arc of the lamp, the reflector mirror position, the condenser lens distance from the arc, and the sample placement from the lamp.

### *300 Watt Broadband Light Source*

A schematic of the 300 watt Xe arc lamp setup is shown below in Figure 2.7.

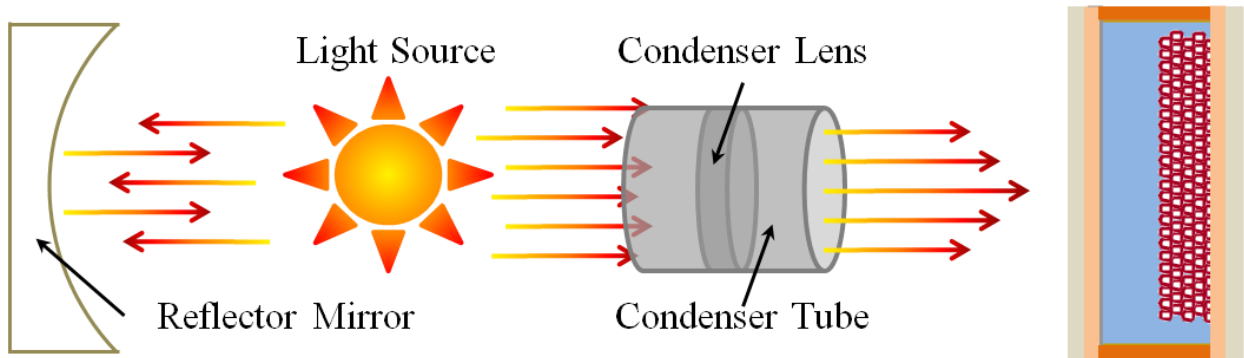


### Figure 2.7 300 W Lamp Setup Schematic

The schematic above shows the path that the irradiated light takes from the 300 W source. Light irradiated in the forward direction (to the right in the schematic) goes directly to through the condenser tube towards the sample. In order to collect as much light as possible and increase the intensity subjected on the sample, light irradiated in the backwards direction (to the left in the schematic) is re-directed forward with a reflector mirror and is then collimated with the condenser lens before striking the sample.

The broadband setup consists of the 300 Watt lamp as the light source, a back reflector mirror to send as much irradiated lamp light as possible forward, and a condenser lens/tube to collimate, converge or diverge the light onto the sample. The first steps for alignment of this lamp were to position the arc in the center of the reflector mirror and the condenser lens. When the lamp was installed in its housing, its horizontal and vertical positioning could be adjusted so that the arc would be roughly centered in the reflector mirror. Once roughly placed in the center, the condenser lens was slid as close as possible to the lamp housing and peering down the condenser tube, the arc was further centered in the back reflector mirror and the condenser lens. This was done by adjusting the vertical and horizontal positions on the lamp, as well as the x, y, z axes of the reflector mirror until the inverted arc image (seen in the reflector mirror) was overlain and aligned nicely with the actual arc. The ideal placement of the inverted arc image over the arc can be seen in Figure 2.8 below (a. arc, b. inverted arc image, c. arc & arc image superimposed).

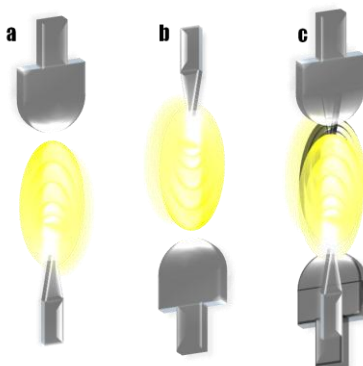


## **Figure 2.8 Arc Lamp & Arc Lamp Image Alignment**

**For proper alignment of the 300 W arc lamp, the actual arc and the arc image (created by back reflector mirror) need to be superimposed in such a manner that the “hot spots” of the electrodes (tip of point electrode) do not lie directly over the larger curved anode as seen in C of the above figure.**

For ideal alignment the inverted arc image (outlined in black) would be superimposed over the actual arc but this would put the arc hot spots (point electrodes - cathode) directly over the curved electrode (anode) and would cause the lamp to overheat. Therefore the inverted arc image was superimposed over the arc such that the arc hot spots were just inside the anode and anode image. The hot spots were situated far enough from each other to keep them from directly overlapping but they put close enough so that they didn't fall onto the anodes or anode image. This placement allowed for the brightest points of the arc & the arc image to overlap so that a near circular beam was irradiated from the lamp housing (condenser lens).

With the inverted arc image aligned nicely over the actual arc, the lamp was turned on and fine tuning of the beam uniformity was begun. Before fine tuning though, the condenser lens was slid forward to diverge the beam and using the Thor Labs power meter, a suitable distance from the lamp was chosen as to get the power density close to  $100\text{mW}/\text{cm}^2$ . Once the distance from the lamp was set, the other three parameters could be slightly adjusted to bring the beam uniformity as close to unity as possible. As stated before, ideally the incident power would be the same across the whole beam but that is not possible. The actual achievable beam uniformity is a power density variation of less than 10% over a  $1\text{ cm}^2$  area, which would well encompass the area of the devices in question. In order for the power density uniformity to be fine tuned, the lamp needed to have ample time to warm up to let the beam stabilize prior to any uniformity measurements could be performed. To determine an ample warm up time period, the detector was placed at the most intense point of the beam (roughly center), the lamp was turned on, and the incident power was monitored over an extended period of time (Figure 2.9).

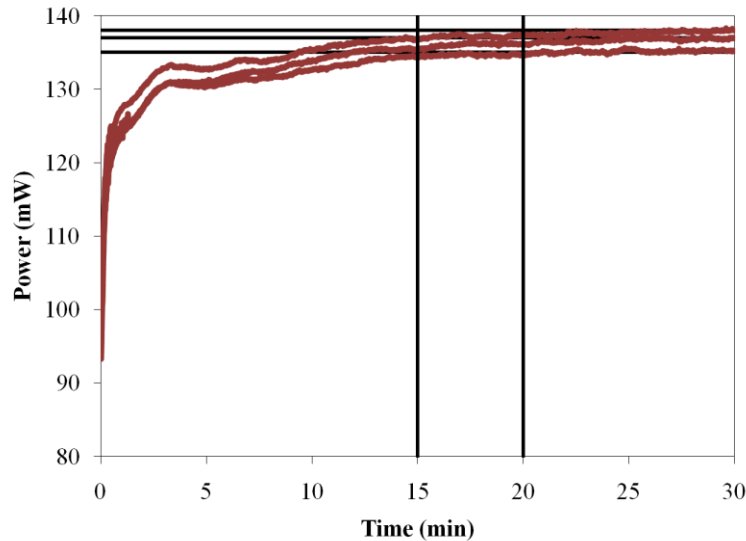


**Figure 2.9 300 W Lamp Incident Power vs. Time**

**For proper use of the 300 W lamp, the lamp needs time to warm up and the irradiated power needs to stabilize before characterizing any devices. A warm up period of 20 minutes is sufficient enough for lamp usage but complete stabilization does not occur until at least 30 minutes of warm up time.**

The red lines are the recorded power over a 30 minute interval from different tests. After 30 minutes the power had stabilized at around 135, 137, & 138 mW respectively. From the black lines, which are drawn at the approximate power stabilizations, the lamp actually stabilizes after about 20 minutes of being on and is fairly stable after 15 minutes but for measurement purposes at least a full 30 minutes was given for the lamp to achieve stabilization. With the lamp roughly centered and warmed up, the fine adjustments were made in order reach the desired beam uniformity. In order to check the uniformity, using the power meter mounted onto the rail carrier, power readings were recorded both in the x-direction (horizontal) and y-direction (vertical). After each uniformity test, a slight adjustment in the reflector mirror position, lamp position, and/or condenser lens position was made and the uniformity was re-checked. The initial uniformity test, which was only done for the x-axis, was quite poor (~75% difference over 2 cm). After many adjustments, a beam uniformity of <10% over 1 cm was obtained for the x-direction so the beam uniformity for the y-direction was tested and was found to be poor as well (~40% difference over 2 cm). After tuning the y-direction it was found that adjustments in the y-

direction affected the x-direction uniformity and vice versa so both axes had to be aligned simultaneously. Following repeated adjustments and tests, an acceptable beam uniformity of 18.09 % difference over 1.5 cm (8.72% over 1 cm) in the x-direction and 11.39 % difference over 1.5 cm (4.79% over 1 cm) in the y-direction was finally obtained (Figure 2.10).

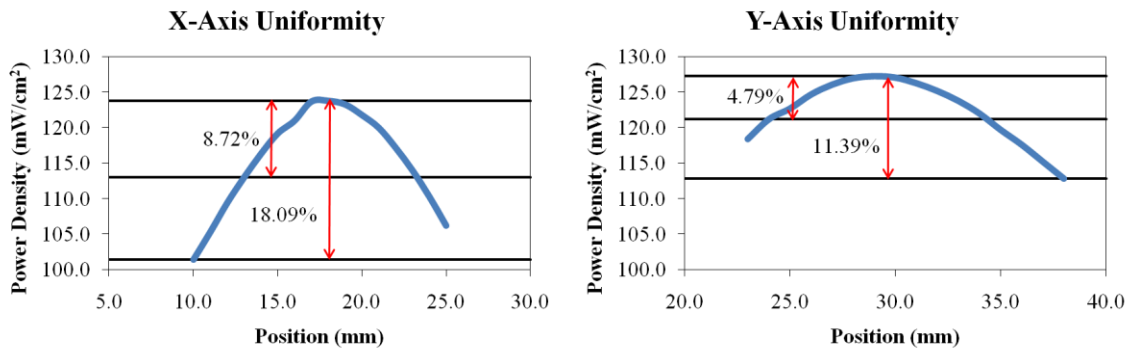


**Figure 2.10 300 W Lamp Acceptable Uniformity**

**The desired beam uniformity is a power density variation of less than 10% over a 1 cm<sup>2</sup> area. After many adjustments to the lamp position, a uniformity of 8.72% over 1 cm in the x-direction and 4.79% over 1 cm in the y-direction was obtained which is well within the desired outcome of <10% variation. Additional fine tunings could be made to further improve the uniformity.**

This uniformity was suitable enough to begin testing devices since the device area would be < 1 cm<sup>2</sup>. Focus was then shifted to the uniformity of the 75 Watt lamp (see section below) Overtime minor modifications were made to the 300 Watt lamp to give a final beam uniformity of 20.50 % difference over 2 cm (7.27% over 1 cm) in the x-direction and 12.66 % difference over 2 cm (3.77% over 1 cm) in the y-direction (Figure 2.11). The uniformity was periodically checked to ensure that it was holding relatively around these values.

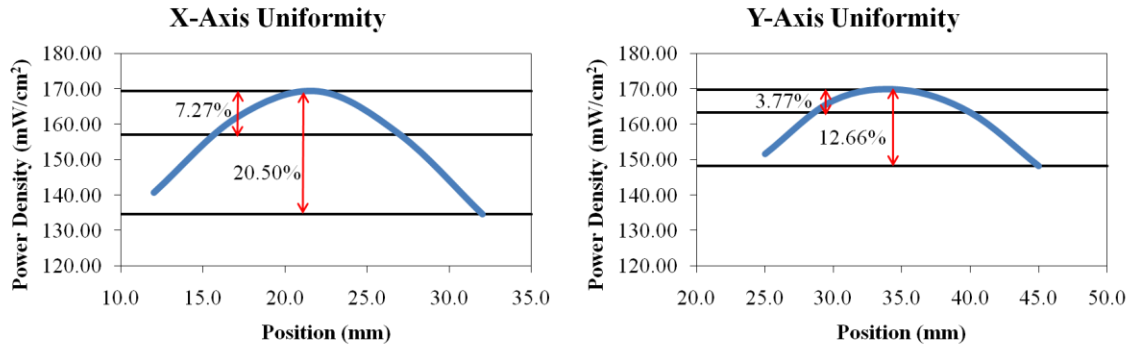


**Figure 2.11 300 W Lamp Final Uniformity**

Following fine adjustments to the lamp to further improve the previous beam uniformity achieved, a final beam uniformity of 7.27% over 1 cm in the x-direction and 3.77% over 1 cm in the y-direction was obtained. The beam uniformity could potentially be further improved but these values are well within the desired power density variation.

### 75 Watt Monochromatic Light Source

A schematic of the 75 watt Xe arc lamp setup is shown below in Figure 2.12.

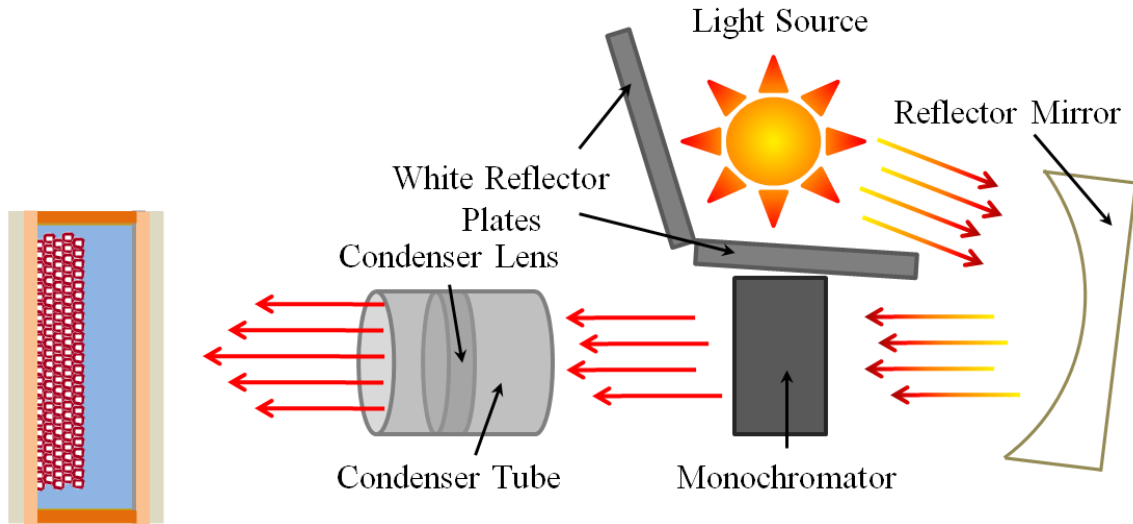


**Figure 2.12 75 Watt Lamp Setup Schematic**

**The schematic above shows the path that the irradiated light takes from the 75 W source. In order to collect as much light as possible and increase the intensity subjected on the sample, white reflector plate are placed on two sides of the lamp to re-direct the light towards the reflector mirror. From the reflector mirror, the broadband light is monochromatized and is then collimated with the condenser lens before striking the sample.**

The monochromatic setup consists of a 75 W broadband light source, reflector plates to send as much irradiated lamp light out of lamp housing, a reflector mirror to re-direct the light towards the monochromator which will separate the broadband light into its monochromatic components, and a condenser lens/tube to collimate, converge or diverge the light onto the sample. The only critical parameter for lamp alignment in this setup is the reflector mirror. The condenser lens plays a minor role and the light source holder is stationary so the lamp position can't be adjusted. Prior to uniformity tests though, the lamp stability over time was tested using the Newport power sensor/meter and it was found that a 30 minute stabilization time was appropriate for this lamp as well (Figure A.4 – Appendix A) Since a majority of the devices tested by this system were dye-sensitized solar cells, mostly those that were sensitized with N719

( $\lambda_{\text{Abs max}} \sim 515 \text{ nm}$ ), the uniformity was first tested and optimized at 550 nm. The initial beam uniformity was well within an acceptable range ( $\sim 13\%$  difference over 1.5 cm in the x-direction and  $\sim 7\%$  difference over 1.5 cm in the y-direction) but improvements were still attempted. In order to get a more accurate reading of the incident power, a mask with a 3 mm hole was employed for the initial uniformity tests. After many adjustments to the x, y, and z directions of the reflector mirror as well as taking measurements at different condenser lens positions (both of which, at times, had detrimental effects on the uniformity), an improved uniformity compared to the initial test was achieved ( $\sim 6\%$  difference over 2.0 cm in both the x and y-directions) (Figure 2.13). Since detrimental deviations occurred from the original uniformity, the power sensor was connected directly to the monochromator housing and the reflector mirror was adjusted until a maximum power was obtained. It was from this reflector mirror position that minor tweaking was done in order to achieve the above improved uniformity.

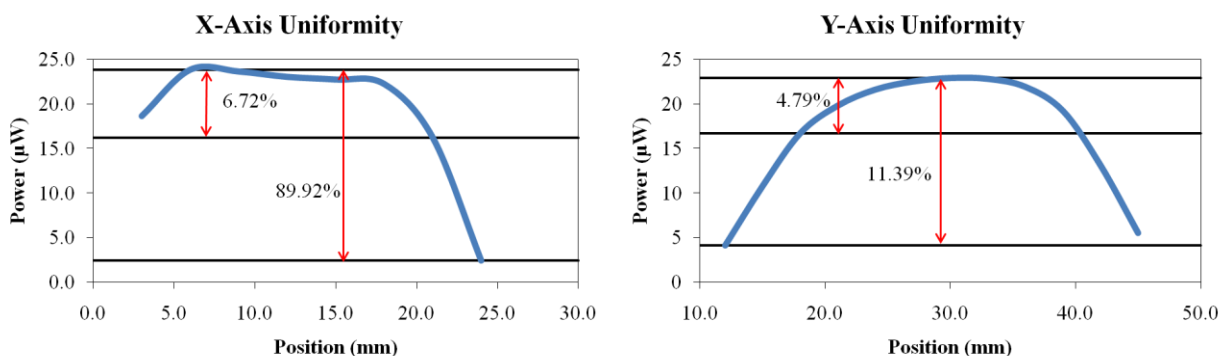


**Figure 2.13 75 W Lamp Acceptable Uniformity at 550 nm**

**Due to the sensitizer employed (N719 -  $\lambda_{\text{max abs}} = 530 \text{ nm}$ ), the uniformity of the monochromatic light was first tested at 550 nm. Again a uniformity of a power density variation of less than 10% over a  $1 \text{ cm}^2$  area is desired. After some alterations in the reflector mirror position an acceptable uniformity of 6.72% over  $\sim 2.0 \text{ cm}$  in the x direction and 4.79% over  $\sim 2.0 \text{ cm}$  in the y-direction was obtained.**

With good beam uniformity at 550 nm, the uniformity at other wavelengths needed to be tested. It was found that the beam uniformity was extremely wavelength dependent (Figure 2.14 & Table 2.2).

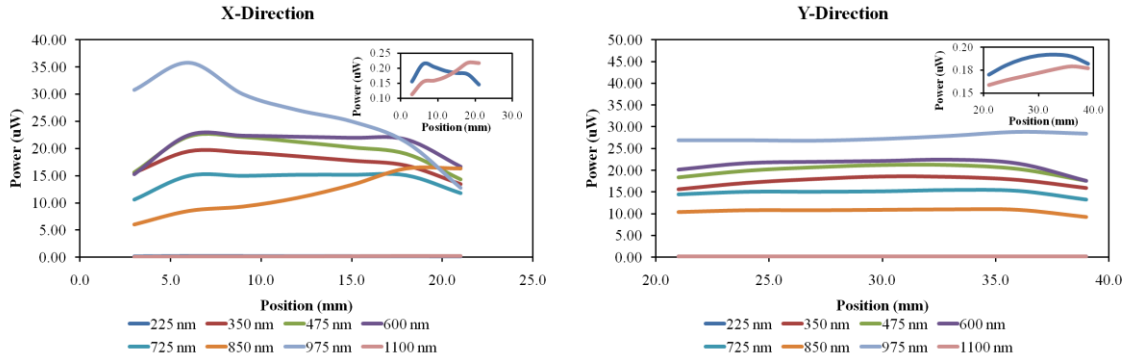


**Figure 2.14 75 W Lamp Uniformities vs. Wavelength (X&Y Axes)**

After achieving a decent beam uniformity at 550 nm, the uniformity at other wavelengths was tested. The uniformity was found to be very wavelength dependent but the uniformities over the visible range, which are the wavelengths of interest, are roughly within the desired power density variation. The power density variations vs. wavelength for the above curves are in Table 2.2.

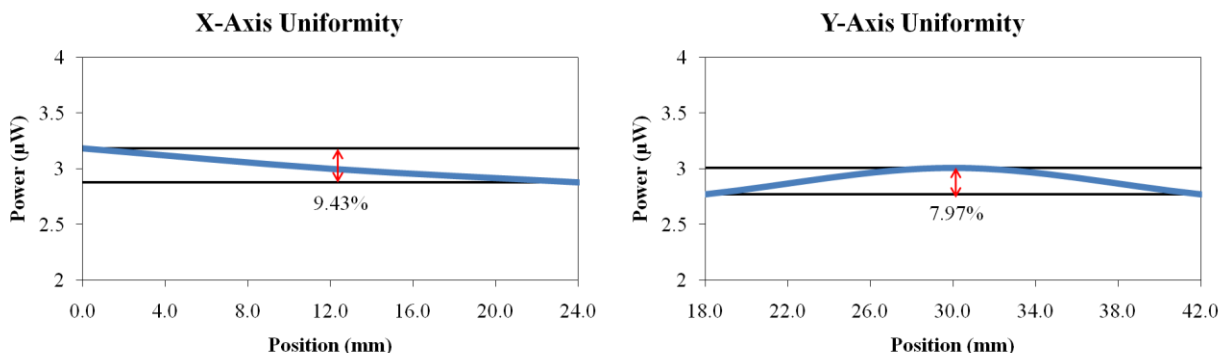
**Table 2.2 75 W Lamp % Differences vs. Wavelength**

<b>X Direction % Differences over 18 mm</b> (3 mm to 21 mm)				<b>Y Direction % Differences over 18 mm</b> (21 mm to 39 mm)			
225 nm	350 nm	475 m	600 nm	225 nm	350 nm	475 m	600 nm
31.78%	30.77%	35.60%	32.00%	11.46%	16.13%	16.98%	21.78%
725 nm	850 nm	975 nm	1100 nm	725 nm	850 nm	975 nm	1100 nm
30.26%	63.19%	64.24%	48.16%	14.19%	15.45%	6.60%	11.17%

<b>X Direction % Differences over 12 mm</b> (6 mm to 18 mm)				<b>Y Direction % Differences over 12 mm</b> (24 mm to 36 mm)			
225 nm	350 nm	475 m	600 nm	225 nm	350 nm	475 m	600 nm
15.89%	13.33%	14.41%	3.56%	6.25%	8.06%	6.13%	4.00%
725 nm	850 nm	975 nm	1100 nm	725 nm	850 nm	975 nm	1100 nm
1.32%	47.85%	40.78%	28.89%	2.58%	1.82%	6.60%	8.38%

Since the beam had been aligned at 550 nm, the uniformity throughout the visible region of the electromagnetic spectrum (which is the only part of the spectrum of major concern for DSSCs) was within acceptable limits (<15 % difference over 1.2 cm in either direction from ~350 nm up to ~725 nm). The uniformity was still satisfactory down into UV range but once the IR region ( $\lambda > 850$  nm) was entered the uniformity became undesirable, with a maximum % difference of >60% over 18 mm at 975 nm in the x-direction. After repeated adjustments to the mirror axes (x, y, & z) as well as changing the sample distance from the source, an extremely uniform beam was obtained over 2.4 cm in both the x & y directions (Figure 2.15).



**Figure 2.15 75 W Lamp Final Uniformity**

**Further improvements were made to the acceptable uniformity shown in Figure 2.13 to obtain a final uniformity of 9.43% over 2.4 cm in the x-direction and 7.97% over 2.4 cm in the y-direction.**

### ***Monochromator Components Optimization***

Since the beam uniformity over the visible region was adequate, a preliminary test using a simple Si test cell from Radioshack® was conducted. Upon collection of the incident power, it was discovered that there was serious dips in the power at 450 nm and 550 nm. (Figure 2.16) This was due to the monochromator components (filter wheel and gratings) not being optimized. The monochromator setup contains 3 cut-on filters (285, 550, and 1000 nm) in its 6 slot filter wheel and 2 gratings inside the monochromator housing. All these components can be programmed to switch at a set wavelength. First the wavelengths at which the filter wheel rotated were optimized by using the transmittance graphs supplied by the vendor to determine the best filter transition. From these graphs and the collected data it was found that the 285 nm cut-on filter would be used from 350 nm to 610 nm, the 550 nm cut-on from 610 nm to 1350 nm,

and the 1000 nm cut-on from 1350 nm & up. By using this configuration the power reduction at 550 nm was drastically improved but the dip at 450 nm was still present (Figure 2.16). The next step was to optimize the wavelength transitions for the monochromator gratings; one grating has a 350 nm blaze and the other a 750 nm blaze. The monochromator was preset to switch gratings at 450 nm (grating 1, 350 nm blaze, 0 nm to 450 nm; grating 2, 750 nm blaze, 450 nm to 1600 nm) which would explain the dip in power. The 350 nm blaze grating is better suited to split out the 450 nm light than the 750 nm blaze so the grating transition needed to be changed from 450 nm to a longer wavelength. After conducting measurements at grating transitions between 450 nm and 550 nm, it was found that a grating transition at 500 nm gave the best performance. The three different curves are given in Figure 2.15; the red curve is prior to any optimizations, the green curve is after the filter wheel adjustments, and the blue curve is after the grating transition change.

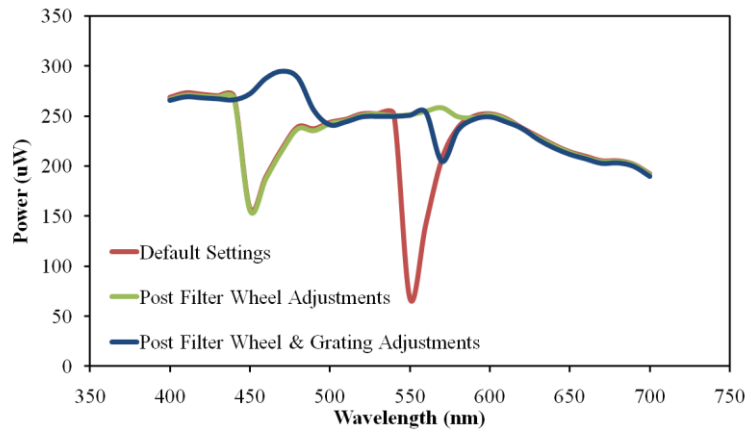


**Figure 2.16 Monochromator Components Optimization**

**The default wavelength settings at which the gratings and filter wheel changed gave rise to massive power reductions in the incident beam. By optimizing the wavelengths at which the filter wheel rotated and the wavelength at which the gratings switched, the power variation across the wavelength range of interest was greatly reduced i.e. power reductions were minimized.**

### *Calibrated Si Reference Cell*

With the lamps aligned and components optimized, the system was ready to be used for photovoltaic device testing. Fabrication and optimization of Grätzel cells began (discussed in detail in Chapter 3) but after the assembly and attempted optimization of countless cells that had low efficiencies to begin with and were showing no drastic improvements in efficiency during optimization, suspicions arose that the cells were optimized but something else was causing the low efficiencies. After all the options had been exhausted, it was realized that the power meters may not be properly calibrated, therefore not displaying the true power from the lamp. In order to accurately test photovoltaic devices, a means of verifying that the incident radiation was 1 sun ( $100 \text{ mW/cm}^2$ ) was required. In order to ensure that the lamp power output was of the desired quantity, a calibrated Si reference cell was purchased from PV Measurements, Inc., Boulder, Colorado (2 cm x 2 cm, KG5 window). Upon measuring the IV curve of the reference cell, the suspicions of an incorrect detector reading were confirmed. When the lamp output was  $100 \text{ mW/cm}^2$  (confirmed by reference cell), the reading of the Thor Labs detector was actually  $\sim 160 \text{ mW/cm}^2$ . Figure 2.17 shows IV curves of the reference cell; one with the lamp at its original power setting (280 Watts applied to lamp) and another with the lamp at the power setting required to achieve 1 sun (330 Watts applied to lamp).

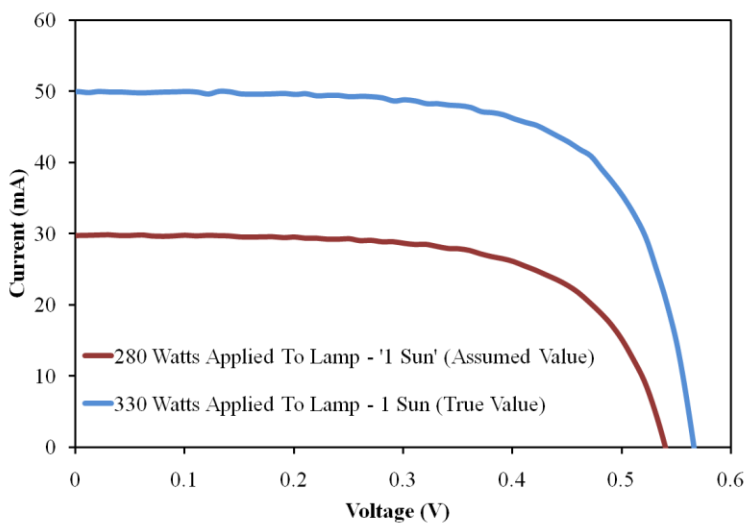


**Figure 2.17 Reference Cell IV Curves - Original Power vs. Calibrated Power for 1 Sun**  
**With 280 Watts applied to the lamp, a detector reading of 100 mW/cm<sup>2</sup> was obtained. This value was ignorantly assumed to be accurate, which led to sub-par device performance. Testing the performance of a calibrated Si reference cell at this lamp power gave a 2/5 reduction in the photocurrent than what should have been achieved. By increasing the power to 330 Watts (detector reading of 160 mW/cm<sup>2</sup>), the desired IV response of the reference cell was attained, leaving the broadband lamp calibrated for further tests.**

The photocurrent is reduced by about 3/5 when using the original lamp power setting of 280 Watts, which accounts for the lower than normal Grätzel cell efficiencies obtained. After implementation of the reference cell and accounting for the power correction, the cell performances were more reasonable (See Chapter 3). Table 2.3 compares the solar cell parameters at the two different applied lamp powers. A 3/5 reduction in photocurrent corresponds to almost a 1/2 reduction in device efficiency (4.64% vs. 2.46%). If the correct sun value is used for the efficiency calculation at 280 Watts applied lamp power, the efficiency of the reference cell is closer to what it should be. Taking this correction into account (assuming the other parameters remain virtually unchanged) would put the efficiency of the “poor” Grätzel cells between ~3.80% - 4.14% compared to ~2.20% - 2.40%, which is close to the highest efficiency obtained for these cells in our lab. (See Chapter 3)

**Table 2.3 Effect of Mistaken Irradiance on Reference Cell Characteristics**

	<b>I<sub>sc</sub> (mA)</b>	<b>J<sub>sc</sub> (mA/cm<sup>2</sup>)</b>	<b>V<sub>oc</sub> (V)</b>	<b>FF</b>	<b>η (%)</b>
<b>1 Sun (True Value)</b> Detector Reading ~160 mW/cm <sup>2</sup>	49.93	11.99	0.5657	0.6845	4.64
<b>“1 Sun” (Assumed Value)</b> Detector Reading 100 mW/cm <sup>2</sup>	29.74	7.143	0.5465	0.6291	2.46
<b>0.58 Sun (True Value)</b> Detector Reading 100 mW/cm <sup>2</sup>	29.74	7.143	0.5465	0.6291	4.20

The reference cell was calibrated by VLSI Standards and calibration data was supplied (IV curves, data table, & IPCE) which can be found in Appendix B. An IV curve and the IPCE collected with the above solar simulator are shown below (Figure 2.18). The critical parameters

of the solar cell provided by VLSI Standards are also compared with those collected by our lab (Table 2.4).

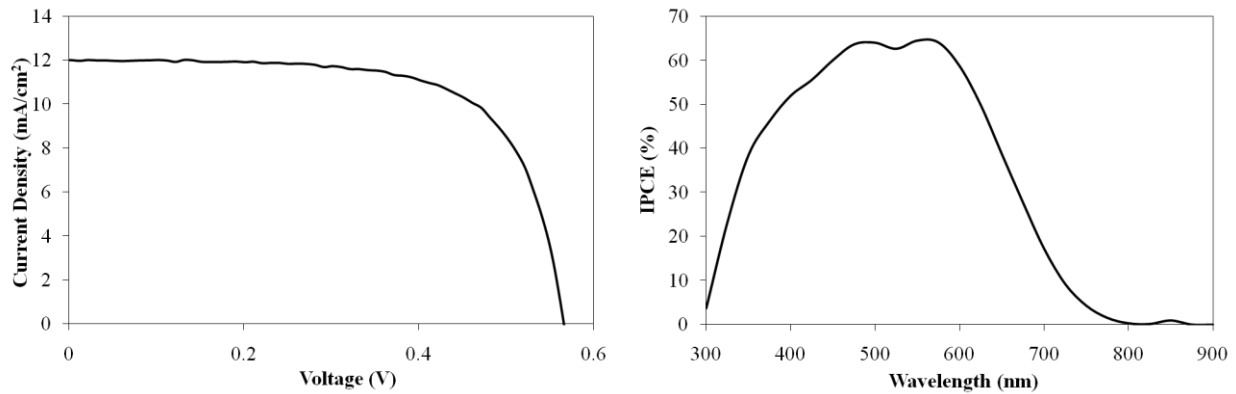


**Figure 2.18 Measured IV & IPCE of Reference Cell**

The measured IV response (in current density) and IPCE response of the reference cell coincide with the calibrated curves provided by the supplier (Figure B.1 & B.2) which indicates proper lamp calibration. Table 2.4 compares the measured values with the calibrated values further showing the proper lamp calibration.

**Table 2.4 Si Reference Cell Calibrated Values vs. Measured Values**

Certified Values							
$I_{SC}$ (mA)	$J_{SC}$ (mA/cm <sup>2</sup> )	$V_{OC}$ (V)	FF (%)	$\eta$ (%)	$J_{max}$ (mA/cm <sup>2</sup> )	$V_{max}$ (V)	$P_{max}$ (mW/cm <sup>2</sup> )
49.7 ± 0.7	11.94	0.5639 ± 0.0032	67.3 ± 1.0	4.5 ± 0.1	10.21	0.4446 ± 0.0059	4.54
Measured Values							
$I_{SC}$ (mA)	$J_{SC}$ (mA/cm <sup>2</sup> )	$V_{OC}$ (V)	FF (%)	$\eta$ (%)	$J_{max}$ (mA/cm <sup>2</sup> )	$V_{max}$ (V)	$P_{max}$ (mW/cm <sup>2</sup> )
49.93	11.99	0.5657	68.40	4.64	10.28	0.4513	4.64

After completing all the setup and optimizations, the solar simulator system was calibrated and ready for use. Prior to any measurements being conducted, the reference cell was tested to ensure that the lamp was still well aligned and of the proper power.

## **Conclusions**

A solar simulator system was acquired, installed and calibrated. To certify this calibration, a reference cell was also employed. Incident power density variations of less than 10% difference over 15 mm in x and y directions were achieved for both broadband and monochromatic light sources. Further lamp uniformity optimizations could be performed to further decrease the power density differences.

## Chapter 3 - Fabrication & Optimization of Grätzel Cells

With the ever increasing need for economical, renewable, alternate sources of energy, there have been surges of research into the various possible alternate sources such as solar and wind energy. The collection and harvesting of solar energy through photovoltaic processes is one of the more promising alternatives to our current fossil fuel economy. Presently the most widely utilized photovoltaic device is based on a single p-n junction made with silicon. Silicon solar cells are able to obtain high efficiencies but the downfall is, in order to achieve this performance, expensive fabrication techniques and high purity materials must be employed. An encouraging cheaper alternative to silicon solar cells is the dye-sensitized solar cell (DSSC) which is based on a wide band gap semiconductor sensitized with a visible light absorbing species. While DSSCs are less expensive, their efficiencies are still relatively low compared to silicon based cells. The DSSC was first pioneered by Michael Grätzel with the development of the benchmark Grätzel cell. These cells (discussed in the section below), whose heart lies in  $\text{TiO}_2$  as the semiconductor and a ruthenium dye complex as the sensitizer, have reached efficiencies  $>10\%$  (Figure 3.1).<sup>7, 8</sup> Due to the low production costs, ease of fabrication, and relatively high efficiencies, Grätzel cells have become a standard for means of comparison to other newly developed DSSCs (new cell architectures or cell components).<sup>10</sup> While investigating new DSSCs devices and investigating their phenomena, Grätzel solar cells (GSCs) were fabricated and optimized in tandem (discussed in latter section). After optimization, GSCs made with a single layer (5-7  $\mu\text{m}$ ) of  $\text{TiO}_2$  nanoparticles having efficiencies  $>4\%$  and GSCs made with two layers (10-14  $\mu\text{m}$ ) of  $\text{TiO}_2$  nanoparticles having efficiencies of  $\sim 6\%$  were obtained.

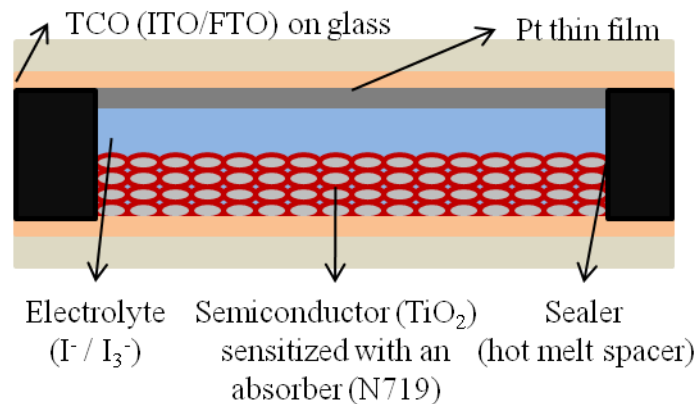


### Figure 3.3.1 DSSC Components

Above is a schematic of the basic DSSC components. The device consists of three main parts; the photoanode, the counter electrode, and the electrolyte. The photoanode is a film of a sensitized semiconductor sintered to a transparent conductive oxide (TCO) substrate. The counter electrode is simply a Pt coated TCO substrate and the electrolyte consists of a redox couple to shuttle charges from the photoanode and CE. The photoanode and CE are sealed together with a hot melt spacer and the electrolyte fills in the gap.

### Benchmark Grätzel Cell

After two decades of research, the benchmark Grätzel Cell mentioned above, which is made with  $\sim 10 \mu\text{m}$  thick  $\text{TiO}_2$  nanoparticle layer, has been pushed to efficiencies  $>10\%$ . The heart of the device (and all DSSCs), is the photoanode, which consists of a semiconductor ( $\text{TiO}_2$ ) and a light absorbing species/sensitizer (ruthenium dye complex). The most basic Grätzel cell consists of the sensitized  $\text{TiO}_2$  nanoparticle network, the electrolyte, and Pt CE, all sandwiched between two fluorine doped tin oxide (FTO) coated pieces of glass. The most efficient devices also contain means of trapping as much light inside the device as possible. A 2<sup>nd</sup>  $\text{TiO}_2$  nanoparticle network (10 nm & 400 nm particles) is applied to the top of the photoanode to act as a light scattering layer and an anti-reflective film is deposited onto the glass's surface to help reduce light losses due to the glass substrate. What sets Grätzel cells (DSSCs) apart from other photovoltaic devices is what occurs at the heart of the device. In solid state p-n junction devices, charge generation and charge separation occur as a single process, whereas in DSSC's, charge generation occurs in the dye and charge separation occurs at the sensitizer/ $\text{TiO}_2$  interface. Charge generation occurs when incident light is absorbed by the dye, exciting an electron, which is immediately injected (0.1 to 100 picoseconds) into the  $\text{TiO}_2$  layer.<sup>71-74</sup> The injection efficiency of the electron is near unity.<sup>74-77</sup> Once injected, the electron must percolate through the nanoparticle network (through  $>1,000,000$  nanoparticles) before it can be collected, which introduces a lot of possible sites for recombination.

# Optimized Fabrication of Dye-Sensitized Solar Cell

## Device Fabrication

All FTO substrates used were diced into 2 cm x 2.5 cm pieces from a larger FTO coated glass piece (TEC8, Dyesol, Queanbeyan NSW, Australia & Pilkington, Toledo, Ohio, USA). A simple schematic flow chart showing the fabrication steps is given below (Figure 3.2) and a full detailed explanation follows.

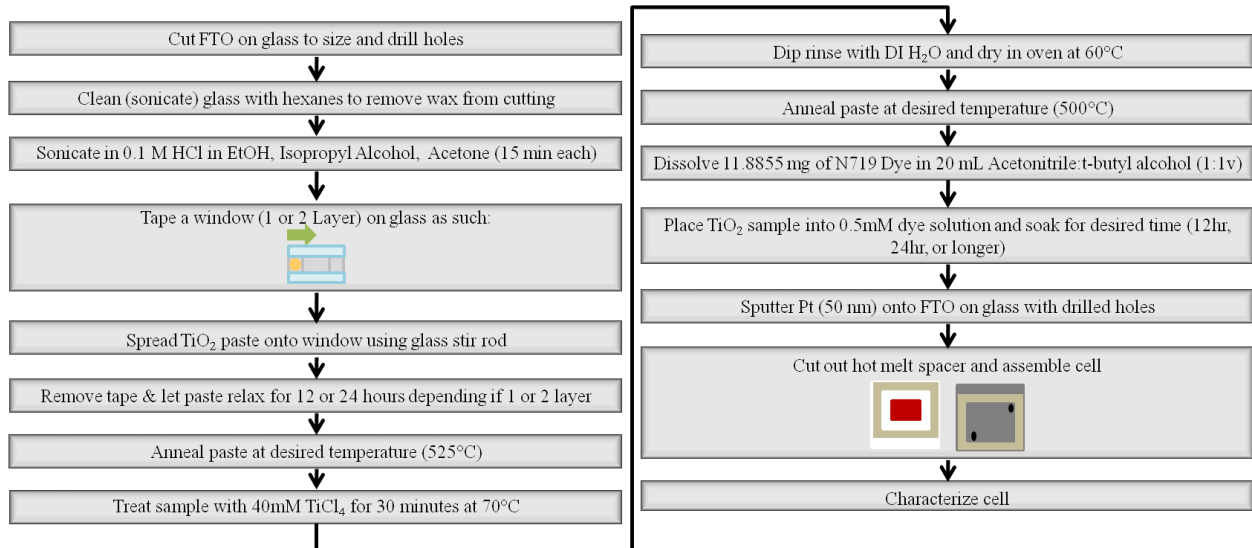


**Figure 3.2 Solar Cell Fabrication Flow Chart**

**The above chart shows the simplified preparation steps for a DSSC from bare substrates to a fully assembled functioning device.**

### Photoanode Preparation

The FTO substrates (Dyesol & Pilkington) were consecutively sonicated in 20 mL of 0.1M HCl in absolute ethanol, 20 mL of isopropyl alcohol, & 20 mL acetone for ~20 min each and dried upright at 60°C. The volumes used increased per number of substrates sonicated; ~20 mL for two, ~40 mL for four, ~60 mL for six, etc. The substrates were then treated with ~100 mL of 40mM aqueous solution of  $\text{TiCl}_4$  at 70°C for 40 min. Due to the exothermic nature of the  $\text{TiCl}_4$  dissolution in water, the  $\text{TiCl}_4$  stock solution (Acros Organics, 99.9%) is stored at ~4°C and the 40mM solution is prepared using previously chilled (~4°C) deionized water. The deionized water was submersed in an ice/water bath and was under magnetic stirring prior to the addition of  $\text{TiCl}_4$ . The 40mM  $\text{TiCl}_4$  solution was stored at ~4°C until it was needed. After  $\text{TiCl}_4$

treatment, the substrates were rinsed with deionized water and acetone and dried upright at 60°C. Once dry, a window was made on the substrates using Scotch® Magic Tape (~50-60 µm thickness) and TiO<sub>2</sub> paste (Dyesol, DSL 18NR-T) was applied over the window using the doctor blade technique. The tape was removed and the paste was allowed to relax for ~4 hours. The TiO<sub>2</sub> coated substrates were placed into a tube furnace, dried at 50°C and 70°C for 15 min and then sintered at 525°C for 30 min. Once the substrates had cooled to ~80°C, they were subjected to another 40mM TiCl<sub>4</sub> treatment (~100 mL) at 70°C for 30 min. The substrates were rinsed with deionized water and absolute ethanol and dried at 60°C. The sintered TiO<sub>2</sub> substrates were placed back into the tube furnace, dried at 50°C and 70°C for 15 min and then annealed at 500°C for 30 min.<sup>78</sup> When the substrates had cooled to 70°C, they were soaked in a 0.5mM solution of N719 dye (Solaronix, Ruthenium 535-bisTBA) in acetonitrile:t-butyl alcohol (1:1v) for 12 hours in the dark at room temperature. After soaking, the sensitized photoanodes were briefly soaked (<2 min) in absolute ethanol followed by a rinsing with absolute ethanol and then were dried at 60°C. The sensitized photoanodes were stored in the dark at room temperature until cell assembly took place.

### ***Platinum Counter Electrode***

A 0.75 mm hole was drilled into each piece of FTO glass using a Dremel drill and a diamond drill bit. The substrates were consecutively sonicated in absolute ethanol, isopropyl alcohol, & acetone for ~20 min each and dried upright at 60°C. The substrates were mounted to a sample holder for an ion beam coater and blown off with nitrogen gas before being inserted into the ion beam coater (Gatan Model 681 High Resolution Ion Beam Coater). 50 nm of Pt was sputtered onto the substrates at a rate of ~1.5Å/sec, a rocking angle of 7° at 8 rocks/sec, and 30 rotations per minute.

### ***Device Assembly***

The sensitized photoanodes and the Pt counter electrodes were sealed together with a 25µm hot melt spacer (Solaronix, SX 1170-25PF). A window was cut into the hot melt spacer with a gap between the sensitized TiO<sub>2</sub> and the spacer of ~2 mm. The electrodes and hot melt spacer were pieced together and held in place with a 1” binder clip. The electrode assemblies were placed in an oven at 60°C; the temperature was ramped to 110°C over ~10 min, held at 110°C for ~5 min, and the oven was allowed to cool via natural convection. Once cooled, a

NanoPort™ was affixed over the hole in the platinum counter electrode using epoxy and the epoxy was cured. Right before characterization, electrolyte (Solaronix, Iodolyte AN-50) was filled into the cell via vacuum filling.

### ***Photoanode & Device Characterization***

The photoanodes were characterized with UV-Vis and SEM. The fully assembled devices were characterized with IV curves (Dark & Light), IPCE, EIS, Chronoamperometry, & Chronopotentiometry. The thickness of a single tape layer of TiO<sub>2</sub> film was characterized with SEM (Hitachi S-3400 N) and found to be ~5µm. The Grätzel cell photoanodes were characterized with UV-Vis (Beckman DU 640 Spectrophotometer) throughout the device construction (before TiO<sub>2</sub> application, after the 2<sup>nd</sup> annealing of TiO<sub>2</sub>, and after dye soaking). The fully assembled devices were characterized with a solar simulator system from Newport Corporation. All IV curves, IPCE, and Chronopotentiometry were collected using a source measure unit (SMU) from Agilent (SMU #U2722A). EIS were collected with a potentiostat from Princeton Applied Research (PARSTAT 2273) and Chronoamperometry was completed with a potentiostat from CH Instruments (CHI440A Electrochemical Analyzer). Once assembled, the devices were first characterized with a dark IV (-0.2 V to 0.75 V) at 0.01 V/s followed by consecutive dark sweeps from 0.2 V to 0.75 V at 0.001 V/s. Due to the instrument design, sensitivity levels, and the variation in the dark current of the devices, the sensitivity level was changed as the sweeps were collected from 0.2 V to 0.75 V. For the first dark sweep from 0.2 V to ~0.3 V, the sensitivity was set at 10 µA; from ~0.3 V to ~0.45 V, the sensitivity was set at 100 µA; from ~0.45 V to ~0.58 V, the sensitivity was set at 1 mA; and from ~0.58 V to 0.75 V the sensitivity was set at 10 mA.

After all the dark curves were collected, two IV curves (-0.2 V to 0.75 V) were collected (~30 sec between collections) under 1 sun (100 mW/cm<sup>2</sup>) using a 300 W OF Xe lamp and an AM1.5G filter. The device was then placed in front of the Newport monochromatic light setup [75 W OF Xe lamp, motorized monochromator (#74004)] and the incident photon to current (IPCE), or external quantum efficiency, (EQE) was obtained. A third IV curve was collected under 1 sun irradiance to test for any cell degradation after EQE collection. Electrical impedance spectroscopy (EIS) was conducted on the devices to fit them to an electrical circuit as well as determine the electron lifetimes. EIS was performed in a frequency range of 100 mHz to 100

kHz (100 data points collected) with a AC potential of 10 mV rms overlaid. Using a shutter (Newport model #71445) to interrupt the incident light, chronoamperometry (CHI) and chronopotentiometry (Agilent) were conducted on the devices. For the chronoamperometric tests, a potential of 0 V (short circuit conditions) was applied to the devices and the resulting photocurrent was measured under dark & light conditions. The measurement began with the device under dark conditions for 10 sec; then the shutter was held open for 10 sec and 10 sec alternations of dark/light were conducted for a total 3 minutes. For the chronopotentiometric tests, a current of 0 A (open circuit conditions) was applied to the devices and the resulting photovoltage was measured under dark & light conditions. The measurement began with the device under dark conditions for 10 sec; then the shutter was held open for 10 sec and 10 sec alternations of dark/light were conducted for a total of 1.5 minutes. At 1 min 30 seconds, the shutter was opened for 10 sec and then left closed for 20 sec to investigate the decay of the photovoltage over a longer time period (due to some devices decaying very slowly). After 3 minutes, the shutter was opened one last time for 10 seconds and then the photovoltage decay was monitored up to 4 minutes (50 seconds), to ensure that the photovoltage had returned to dark conditions. A fourth IV curve was collected under 1 sun irradiance to again test for any cell degradation. For some of the devices, the IV characteristics were measured at different light intensities (1 sun, 0.5 sun, 0.25 sun). Using a neutral density (ND) filter (Newport #FSQ-ND03), the incident power density was reduced by half to achieve 0.5 sun and an IV curve was collected under these conditions. Leaving the ND filter in the light path, the applied power to the lamp was reduced from 330 Watts to 190 Watts in order to achieve 0.25 sun. Again an IV curve was collected under these incident light conditions. For the devices characterized with varying light intensities, one final IV curve at 1 sun irradiance was collected to again test the stability of the solar cell.

### **Dye-Sensitized Solar Cell Optimization**

Double layer GSCs were synthesized and optimized first but for comparison purposes (to Au nanoparticle incorporated cells discussed in Chapter 4), a plethora of single layer GSCs were fabricated and optimized following similar optimization steps. The four optimizations that were found to be critical to obtain the achieved efficiency of the devices were the transparent conductive oxide (TCO) employed, the method of the Pt application for the CE and its

subsequent thickness, the period of time that the TiO<sub>2</sub> paste was allowed to relax prior to sintering, and the integrity of the TiCl<sub>4</sub> solution for the TiCl<sub>4</sub> treatment. These four components of the fabrication process drastically affected the fill factor (series and shunt resistances) and the short circuit current density (J<sub>SC</sub>), which in turn affected the overall efficiency of the cell. Other techniques were also tried to further optimize the device efficiency (dye soaking time, annealing temperature, removing iron cation contamination, & taping methods) but will only be briefly touched. Although many different techniques were used to optimize the devices' performances, none could push the efficiencies past ~2.5% for single layer and ~4.1% for double layer. It wasn't until the steps outlined by Grätzel et al and Reale et al were followed (paste relaxation and TiCl<sub>4</sub> treatment) that devices with higher performances were achieved.<sup>7, 78</sup> After thorough (but not exhausted) optimizations, GSCs with efficiencies >4% (single layer) and efficiencies around 6% (double layer) were obtained (Figure 3.3 and Table 3.1) A statistical analysis for the single layer cells can be found in the Appendix C – Table C.1. In table 3.1, the GSCs are grouped by layer size (single or double) and are sorted from highest to lowest efficiency within each group.

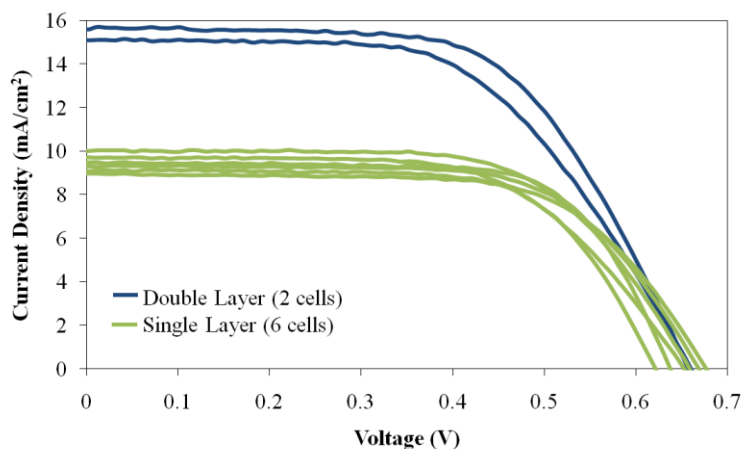


### Figure 3.3 IV Curves - Optimized Double & Single Layer GSCs

Four preparation steps were found to be critical in the fabrication of reasonably efficient GSCs: 1) the transparent conductive oxide (TCO) employed, 2) the method of the Pt application for the CE and its subsequent thickness, 3) the period of time that the TiO<sub>2</sub> paste was allowed to relax prior to sintering, 4) the integrity of the TiCl<sub>4</sub> solution for the TiCl<sub>4</sub> treatment. After optimization of these preparation steps, single layer and double layer GSCs displaying efficiencies >4% and ~6%, respectively, were obtained.

Table 3.1 Photovoltaic Characteristics - Optimized Double & Single Layer GSCs

	V <sub>OC</sub> (V)	J <sub>SC</sub> (mA/cm <sup>2</sup> )	FF	η (%)	R <sub>SH</sub> (kΩ)	R <sub>S</sub> (kΩ)
<b>Double Layer</b>	0.6566	15.608	0.6084	6.24	0.8133	0.0109
	0.6601	15.093	0.5671	5.65	1.1616	0.0134
<b>Single Layer</b>	0.6584	10.021	0.6389	4.22	7.8309	0.0141
	0.6374	9.467	0.6962	4.2	4.5331	0.0098
	0.6684	9.293	0.6524	4.05	10.2669	0.015
	0.6766	8.973	0.6469	3.94	1.4813	0.0157
	0.6523	9.716	0.609	3.86	13.8122	0.0166
	0.6212	9.094	0.6786	3.83	1.7556	0.0106

As discussed in Chapter 2, prior to calibrating the solar simulator system with a reference cell, all of the cell's performances were drastically lower than what was hoped. Although correcting for the un-calibrated system helped "improve" the performance of the devices by bringing the broadband light source up to the correct incident power density, it is not necessarily an optimization of the device itself and will not be discussed in detail. A detailed comparison of the devices' calculated efficiencies with measured data vs. calculated efficiencies taking the power density correction into account are provided in Appendix C – Figure C.1.

### *Optimization Process*

As stated above four critical parameters were discovered throughout the optimization process, which were the TCO employed, the application method of Pt for the CE, the TiCl<sub>4</sub> solution & paste relaxation. The effect of changing these parameters can be seen in Figure 3.4 &

Table 3.2. The IV curves shown in Figure 3.3 are of devices before (dotted lines) and after (solid lines) the critical changes.

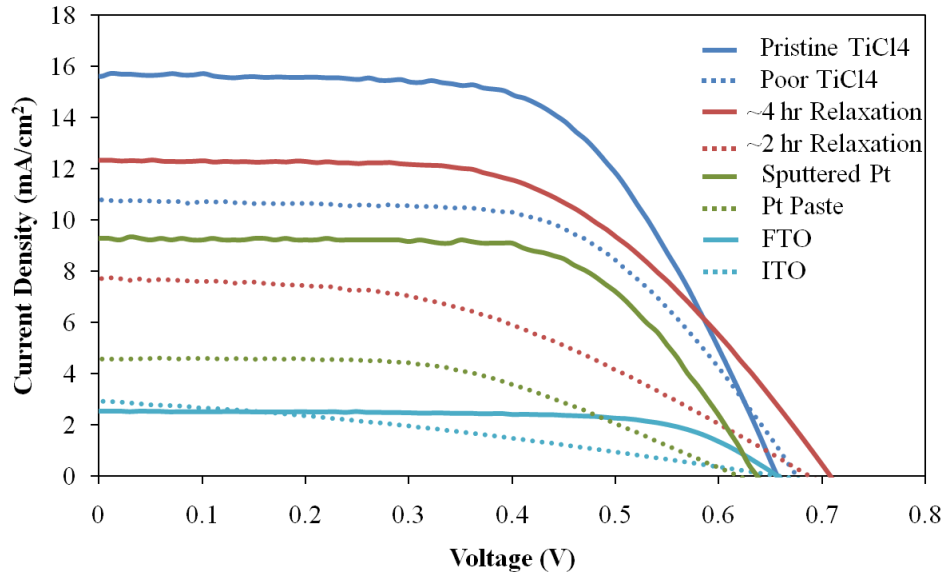


**Figure 3.4 Critical Parameter's Effects on IV Characteristics**

The effects of the optimization of the four critical preparation steps is shown above. All the optimizations improved (lowered) the series resistance of the devices, which led to higher photocurrents and in turn higher fill factors and efficiencies. The decreased series resistances and improved properties are made apparent in Table 3.2.

**Table 3.2 Photovoltaic Properties Before & After Key Optimizations**

	$V_{OC}$ (V)	$J_{SC}$ (mA/cm <sup>2</sup> )	FF	$\eta$	$R_{SH}$ (k $\Omega$ )	$R_S$ (k $\Omega$ )
<b>ITO</b>	0.6584	2.917	0.312	0.60%	0.412	0.171
<b>FTO</b>	0.6564	2.532	0.6893	1.15%	4.753	0.032
<b>Pt Paste</b>	0.6197	4.58	0.5143	1.46%	7.639	0.059
<b>Sputtered Pt</b>	0.6375	9.238	0.6448	3.82%	3.027	0.014
<b>2 hr Relaxation</b>	0.6874	7.706	0.4465	2.35%	1.307	0.043
<b>4 hr Relaxation</b>	0.7086	12.341	0.5506	4.82%	3.316	0.019
<b>Poor TiCl4</b>	0.6760	10.802	0.5977	4.36%	1.328	0.018
<b>Pristine TiCl4</b>	0.6566	15.608	0.6084	6.24%	0.813	0.011

The critical parameter that was affected after each optimization for all the devices was the series resistance. As discussed in the intro, a high shunt resistance and a low series resistance are desired for optimal device performance. An approximate of these resistances can be found by taking the inverse of the slope of the IV curve around the short circuit current (shunt resistance) and around the open circuit voltage (series resistance). Refer to Figure 1.11b. If a device has a low shunt resistance, low enough to affect the performance, then the open circuit voltage will be noticeable decreased. The parameters that have a noticeable change in the IV curves are the short circuit current and the fill factor. The increase of both of these after the critical change leads to the increase in efficiency. The improvement in these parameters can all be attributed to the improvement of one critical factor, the series resistance. Just as the shunt resistance affects the open circuit voltage, the series resistance affects the short circuit current and both of these together can affect the fill factor and in turn the device efficiency. The IV curves in Figure 3.4 show that, after each critical change, the slope of the IV curve near the open circuit voltage is drastically increased, which due to the inverse relationship, would led to a smaller series resistance. The calculated values in Table 3.2 (far right column) further show this decrease in series resistance. A more in depth, step by step analysis of these optimization processes is discussed below.

### ***Individual Optimization Steps – Double Layer GSCs***

#### ***1) TCE Optimization***

Cell fabrication began with double layer GSCs (two Scotch® tape layers ~120  $\mu\text{m}$  thick gave 10 – 14  $\mu\text{m}$  thick  $\text{TiO}_2$  layer). The first handful of cells had modest short circuit currents but were plagued with low fill factors, low shunt resistances, high series resistances which in turn gave extremely low (<1%) efficiencies. Due to a problem encountered ( $\text{TiO}_2$  film cracking – to be discussed later) when fabricating these cells improving the series resistance was undertaken first. Besides the problem of the film cracking, another possible source of the high series resistance was the degradation of ITO upon thermal treatment (sintering & annealing) of the  $\text{TiO}_2$  film. ITO has a lower thermal stability than FTO and at the  $\text{TiO}_2$  film annealing temperature of 500 - 525°C a substantial decrease in the conductivity of the ITO occurs. The electrical conductivity of the ITO film arises from defects present in the film's lattice ( $\text{Sn}^{4+}$  ion at an  $\text{In}^{3+}$  site and vacancies in the oxygen lattice).<sup>79, 80</sup> Upon annealing in air, oxygen fills in some

of these vacancies, decreasing the defects that led to the transparent oxides conductive properties.<sup>80, 81</sup> This in turn results in an increase in the electrical resistance of the ITO film, attributed to the increase in  $R_s$ , which is detrimental to the photovoltaic device's performance (Figure 3.6 below). Due to the poor device performance using ITO, thermal stability studies of ITO coated glass vs. FTO coated glass were conducted to confirm the suspicions that the ITO was not surviving the thermal treatments (Figure 3.5 and Figure C.2 in Appendix C).

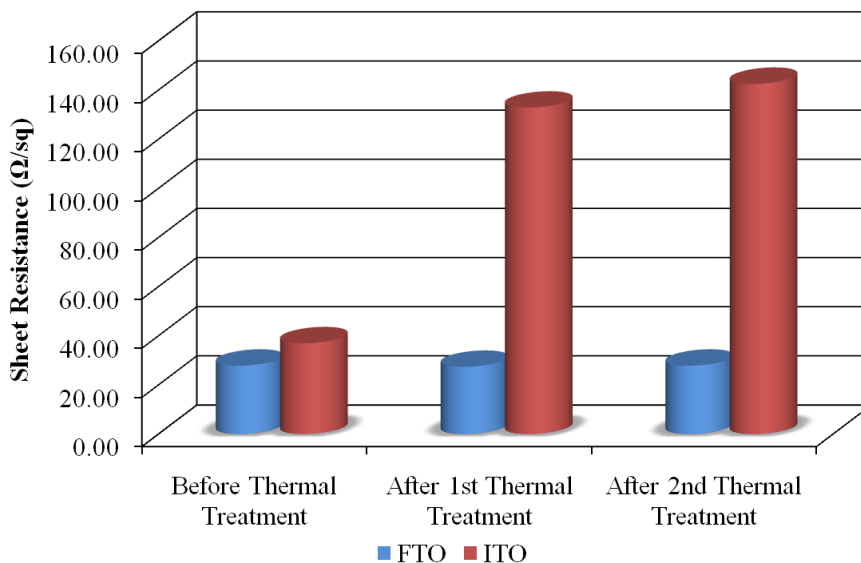


**Figure 3.5 TCO Thermal Stability**

**The criticalness of the choice of which transparent conductive oxide (FTO vs. ITO) is employed is evident from the above graph. In order to fabricate a GSC, the transparent conductive electrodes (TCE) need to be subjected to temperatures >500°C. At temperatures this high (first thermal treatment - 525°C), the conductivity of ITO is drastically reduced which would detrimentally increase the series resistance if employed in a device.**

After the first thermal treatment (525°C), the sheet resistance of FTO remained virtually unchanged (actually slightly decreased), while the sheet resistance of ITO more than tripled (from ~35 Ω/sq up to >120 Ω/sq). Upon the 2<sup>nd</sup> thermal treatment (500°C), FTO again remained unchanged, while ITO increased by about another 10 Ω/sq. This significant increase in the sheet resistance of the ITO film has a profound effect on the performance of DSSC's as is evident in Figure 3.6.

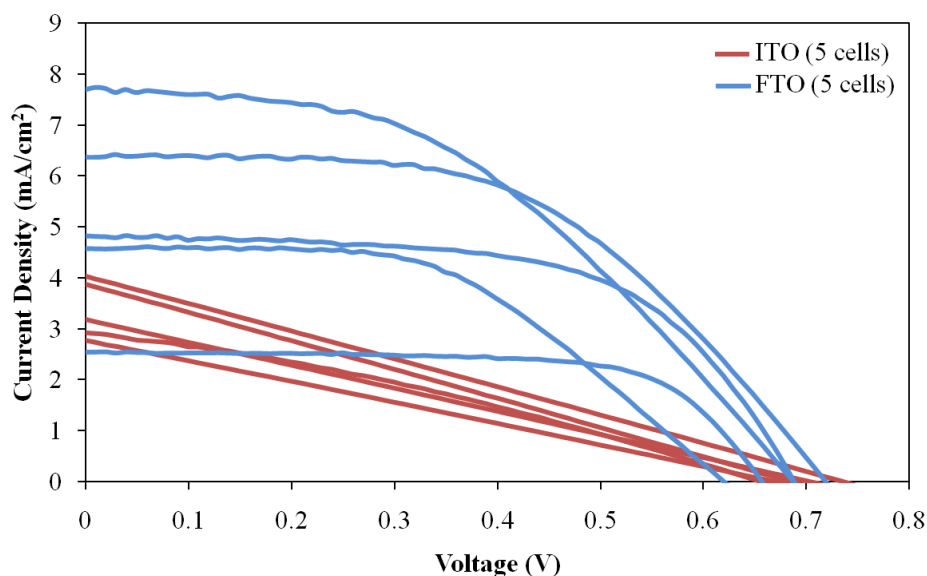


**Figure 3.6 IV Curves - ITO vs. FTO**

**Due to the increased sheet resistance of ITO upon the thermal treatments required for device fabrication, the overall series resistances of the devices is increased to such an extent that unfavorable effects occur. The increased series resistances decrease the photocurrents and fill factors leading to low efficiency devices. By replacing the ITO substrates with FTO the series resistance reductions can be avoided giving respectable IV responses.**

The high sheet resistance of the ITO increased the overall series resistance of the devices which led to IV curves that had poor fill factors of ~30% (straight lines for IV curve profiles). Due to ITO's low thermal stability, the ITO substrates were replaced by more stable FTO coated glass. Upon the replacement, the IV curves had fill factors that were almost doubled (>55%), which led to device efficiencies that were at least doubled.

## **2) Pt CE Optimization**

Although the efficiencies were improved, the series resistances were still high, short circuit currents were still relatively low, and device reproducibility was inconsistent. These shortcomings could be caused by multiple properties (TiO<sub>2</sub> film integrity, dye loading) but since the sheet resistance of the resultant Pt film on the counter electrode (CE) was inconsistent, a more reliable means of fabricating the Pt CE was the next component to be optimized. Originally the

Pt CEs were fabricated using a Pt catalyst paste (Dyesol Pt paste PT-1) that upon annealing decomposed to Pt metal forming a thin Pt film. The problem encountered with this paste was that the resultant Pt film was extremely non-uniform & discontinuous, which gave sheet resistances on the order of hundreds of  $\Omega$ /sq, even when a thick layer of paste was applied. A Pt paste from a different vendor was found to give reasonable performance but further optimizations using this paste were not explored. (See Figure C.3 & Table C.2 – Appendix C) In order to have a more uniform Pt film for the CE, an Ion Beam Coater (Gatan) was employed to sputter Pt onto the FTO substrate. Using the ion beam coater allowed the production of a uniform Pt film to within  $\pm 1 \text{ \AA}$  in thickness. Various Pt thicknesses were explored (40 nm to 80 nm) and it was found that a 50 nm Pt film for the CE gave the best, most reliable photovoltaic performance (Figure 3.7).

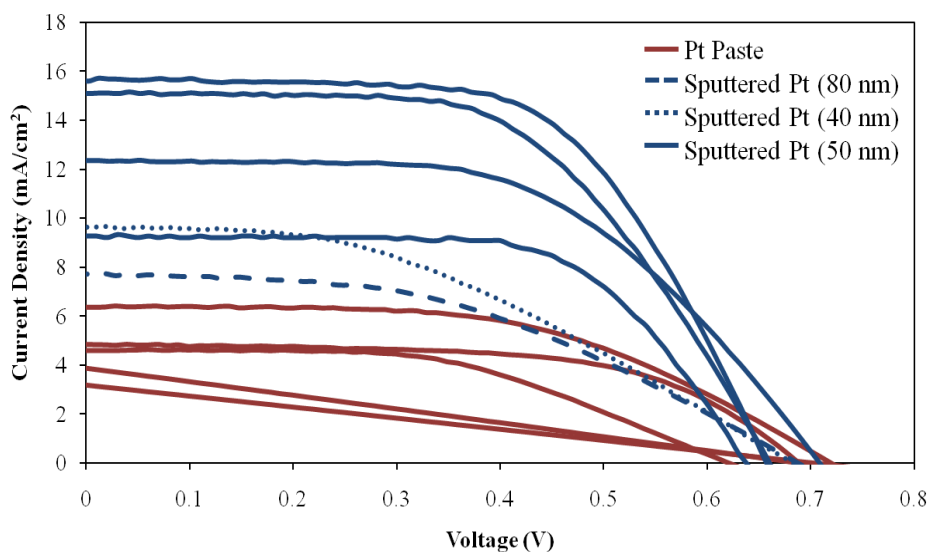


**Figure 3.7 IV Curves - Different Pt CEs**

**Using a Pt catalyst paste as the CE material can cause an increase in the series resistance of a device due to the formation a non-uniform film of Pt. By sputtering an appropriate thickness of Pt (50 nm) onto the substrate instead, lower series resistances can be obtained that give high photocurrents and reasonable efficiencies. If the Pt thickness is too thin (40 nm) resulting in a non-continuous film or too thick (80 nm) resulting in larger film resistances, similar heightened series resistances can occur.**

Once the device substrates were switched to FTO, higher fill factors, higher current densities, and higher efficiencies were achieved using the Pt paste as the CE but the series

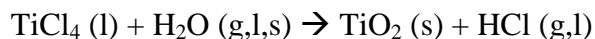
resistances were still high and the device reproducibility was poor. Replacing the Pt paste with sputtered Pt afforded higher current densities but the series resistances still weren't decreased (40 nm & 80 nm sputtered Pt). The series resistance for the 40 nm Pt CE was high most likely because of too thin of a film being deposited. The surface roughness of FTO is quite large (features on the order of hundreds of nanometers) which could have caused a 40 nm film to be somewhat discontinuous therefore increasing the film's sheet resistance (Figure C.4 – See Appendix C). For the 80 nm Pt CE, a continuous thin film could be achieved giving a good sheet resistance but the film was becoming so thick that the resistance over the film was large enough to increase the overall series resistance of the devices. The best device performance came from a 50 nm thick Pt film for the CE. The 50 nm of Pt allowed a continuous enough film for efficient charge transport but it also was not so thick that it hindered the flow of charges. The Pt thickness was likely not the sole cause of the high series resistance after switching to FTO but the best device performances were achieved using a 50 nm thick Pt CE. Further, in depth thickness optimizations could be done in the future.

### ***3) Optimization of photoanode with $\text{TiCl}_4$ treatment***

Another source of the high series resistance is the photoanode, in this case a  $\text{TiO}_2$  thin film. The integrity of this film is the key to obtaining high current densities. There are two device preparation steps that are critical in achieving a consistent, well electrically connected  $\text{TiO}_2$  photoanode film; the consistency of the  $\text{TiCl}_4$  solution and the relaxation of the  $\text{TiO}_2$  paste. Figures 3.8 and 3.9 show the effects that these two steps have on the device's IV characteristics. The first step that will be addressed is the  $\text{TiCl}_4$  solution. During the fabrication process of a device, the FTO substrate for the photoanode is subjected to the  $\text{TiCl}_4$  solution prior to  $\text{TiO}_2$  paste application as well as after the annealing step of the  $\text{TiO}_2$  film. The first treatment enhances the bonding strength of FTO and  $\text{TiO}_2$  and helps block charge recombination between the FTO and electrolyte.<sup>7, 78</sup> The second treatment increases the surface roughness and interconnectivity between the particles thus increasing dye-adsorption and the electrical connection resulting in higher photocurrents.<sup>7, 78, 82</sup> If the integrity of the  $\text{TiCl}_4$  solution is compromised then the integrity of the whole device and thus its performance are at risk.

The  $\text{TiCl}_4$  solution was first prepared under ambient conditions in the fume hood but since  $\text{TiCl}_4$  is moisture sensitive the solution preparation was difficult and the variability in the

concentration of the resultant solution was high due to the stock solution reacting with the water in the air before it could even be diluted.  $\text{TiCl}_4$  reacts exothermically with water (can be violently explosive) to form  $\text{TiO}_2$  and  $\text{HCl}$  as well as oxychlorides.<sup>83</sup>



In order to reduce the moisture exposure, the solution preparation was no longer done under ambient conditions but was completed in a glove box (solely used for DSSC prep). The stock  $\text{TiCl}_4$  and the diluted  $\text{TiCl}_4$  were also stored in the refrigerator ( $\sim 4^\circ\text{C}$ ) to help reduce the exothermic nature of dilution and increase the shelf life, respectively. Over time the  $\text{TiCl}_4$  solution completely reacts with water turning to an opaque white color, indicating the presence of  $\text{TiO}_2$ . Using this preparation method helped in the quality of the  $\text{TiCl}_4$  solution but the reproducibility of the solution was still difficult; solution would immediately turn white. If the solution is this opaque color upon preparation then its integrity is comprised and it will no longer provide the enhancements to the device. Eventually it was discovered that the moisture sensitivity wasn't so much the key issue as was the exothermic nature of the hydrolysis. Due to the exothermic nature of this reaction, the stock  $\text{TiCl}_4$  solution and the DI water used for the dilute solution were stored in a fridge ( $\sim 4^\circ\text{C}$ ). Upon preparation of the solution, the DI water was submerged into an ice bath, was kept under magnetic stirring, and the cold stock  $\text{TiCl}_4$  was added slowly. Using this method increased the integrity and reproducibility of the solution which in turn gave devices with the best photovoltaic performance (Figure 3.8).

The hypothesis is that upon addition of  $\text{TiCl}_4$  to the DI water, intermediate oxychlorides form. If the exothermic nature of this addition is not controlled (via chilled solutions & ice bath) then the heat generated from this reaction causes the intermediates to decompose, forming  $\text{TiO}_2$  and  $\text{HCl}$ . By lowering the dilution temperature, the heat generated by the addition can be absorbed and the intermediates can remain intact. The intermediates will eventually decompose overtime but by slowing this process, increased device efficiencies can be achieved. The rationale behind the enhancements provided by each  $\text{TiCl}_4$  treatment is this: In step 1, the  $\text{TiCl}_4$  decomposes into  $\text{TiO}_2$  on the FTO surface forming the recombination blocking layer and in step 2, due to the acidic nature of the  $\text{TiCl}_4$  solution, the  $\text{TiO}_2$  particles in the film are slightly etched (increasing surface roughness) which dissolves  $\text{TiO}_2$  into solution. Between the decomposition of  $\text{TiCl}_4$  and the  $\text{TiO}_2$  dissolved in solution, additional  $\text{TiO}_2$  is deposited at the particle interfaces, increasing the interconnectivity of the  $\text{TiO}_2$  particles (increasing the electrical connection).

Figure 3.8 shows the effects of these different  $\text{TiCl}_4$  preparation conditions. The transition of the solution preparation to the glove box resulted in some device enhancement but by comparing the IV curves in Figure 3.7 to the ones in Figure 3.5, the enhancements in this case were most likely due to the substitution of ITO coated glass for FTO. Upon the implementation of the chilled solutions, the magnetic stirring, and the ice bath a further increase in device performance (notably the short circuit current) was achieved. If the IV curves in Figure 3.8 are again compared but this time to the ones in Figure 3.7, it is evident that the major contributor to the performance enhancement (decreased series resistance, increased fill factor) is the change from Pt paste to sputtered Pt (50 nm).

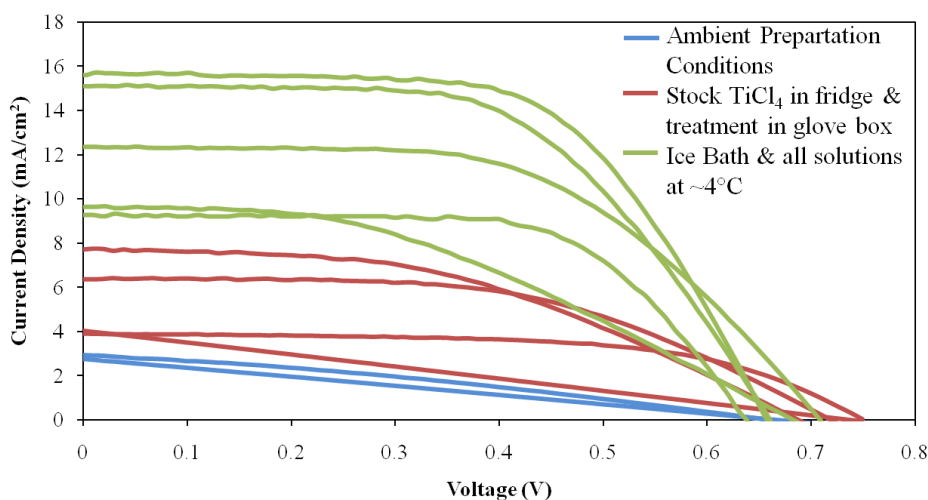


**Figure 3.8 IV Curves -  $\text{TiCl}_4$  Solution Effects**

**Without careful preparations of the  $\text{TiCl}_4$  solution, the solution integrity is prone to being compromised which could cause adverse effects on the photovoltaic characteristics. Due to the exothermic nature of the  $\text{TiCl}_4$  dilution, all the solutions used for the dilution need to be stored at  $\sim 4^\circ\text{C}$  and an ice bath with a magnetic stir bar need to be employed upon dilution. Utilizing this method ensures a high quality  $\text{TiCl}_4$  solution so that upon substrate treatment, decent electrical connections and dye adsorption can be achieved which will result in high photocurrents, reasonable fill factors, and moderate efficiencies.**

A large enhancement in the current density ( $8 \text{ mA/cm}^2$  up to almost  $16 \text{ mA/cm}^2$ ) is eventually obtained by transitioning to the ice bath and chilled solution but the cause of this enhancement can't be solely attributed to this transition though. From this conclusion and the

above conclusions, it would seem that the integrity of the  $\text{TiCl}_4$  solution did not have much bearing on the optimization of the devices but the integrity of this solution is extremely critical despite not being clearly evident in the following IV curves. Figure C.5 in Appendix C clearly shows the criticalness of the integrity of this solution.

#### ***4) Relaxation of $\text{TiO}_2$ Paste***

The final and probably most critical optimization step is the relaxation of the  $\text{TiO}_2$  paste. In the steps outlined by Grätzel et al, a relaxation period is used to decrease surface irregularities but the length of this “leveling” period is dependent on the viscosity of the paste solvent and must be visually monitored by the experimentalist.<sup>7</sup> As briefly mentioned earlier, upon the sintering,  $\text{TiCl}_4$  treatment, and/or annealing of the  $\text{TiO}_2$  paste, the film would crack and flake off, especially near the edges, which would directly affect the series resistance of the devices since the resultant electrical connectivity of the film would be poor. Even if the  $\text{TiO}_2$  survived the fabrication, it was still a concern that the films were compromised since almost every other  $\text{TiO}_2$  photoanode cracked. The initial hypothesis was that the cracking and peeling was possibly due to air bubbles in the  $\text{TiO}_2$  film, which would leave vacancies in the film, not allowing it to adhere well to the TCO substrate or itself, leading to poor electrical connections i.e. high series resistances  $\rightarrow$  low fill factors  $\rightarrow$  low efficiencies. To circumvent this, the as-applied  $\text{TiO}_2$  photoanodes were placed in a vacuum oven (~ 30 inches Hg below atmospheric pressure) at ~70°C for 1-2 hours prior to sintering. The vacuum oven treatment gave devices with improved efficiency leading to the conclusion that the possible air bubbles present were removed and filled in with  $\text{TiO}_2$  which improved the electrical connection of the  $\text{TiO}_2$ . In other words, the series resistance was decreased, increasing the fill factor which gave increased efficiency (Figure 3.9). Upon repeat trials though, it was found that the  $\text{TiO}_2$  films were still cracking apart and the device performances were variable so adopting some of the preparation steps outlined by Grätzel et al, a paste relaxation period was implemented instead of the vacuum oven treatment. The vacuum oven treatment was itself a 1-2 hour relaxation period but the hypothesis was that by placing the  $\text{TiO}_2$  film under vacuum, any air bubbles present would be removed but after their removal, the paste was not allowed to relax long enough for the  $\text{TiO}_2$  nanoparticles to fill in the air bubble vacancies. This would leave gaps in the film reducing the electrical connectivity and/or allowing a stress point for cracking to begin.

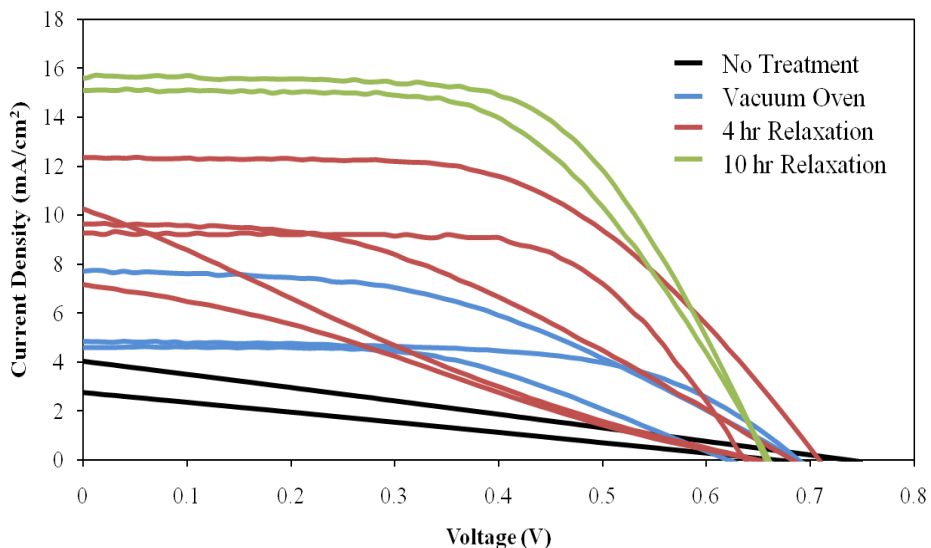


**Figure 3.9 IV Curves - Paste Relaxation**

**Allowing the TiO<sub>2</sub> paste to relax, reducing the surface irregularities, is the key critical fabrication step. Using the other optimized steps discussed above and allowing the paste to relax for four hours can result in an efficient device but the variation in the performance is unpredictable. To obtain a double layer GSC with a reasonable reproducible performance, at least a 10 hour past relaxation period is required.**

Since the vacuum oven treatment did produce devices with reasonable performances and itself was a 1-2 hour relaxation period, a relaxation period of double the time (4 hours) was chosen. The 4 hour relaxation time was conducted outside the vacuum oven in the hopes that any air bubbles present would diffuse out as the paste relaxed over the extended period. The 4 hr relaxation (in combination with the other optimizations) led to a decreased series resistance and an increased short circuit current density. The problem with the 4 hr relaxation period was that the reproducibility of the cells was poor. Even with the previous three critical parameters optimized, some devices that had a four hour TiO<sub>2</sub> paste relaxation period gave bad performances. Keeping the other three critical parameters unchanged, the paste relaxation time was increased to 10 hours resulting in the best performing devices. The increased relaxation time (in combination with the other three parameters) gave the lowest series resistance, highest short circuit current density, a reasonable fill factor, and the highest overall efficiency of >6%.

### *Single Layer GSC's Optimization*

Prior to fully optimizing the double layer GSCs, single layer GSCs were optimized alongside the double layer since the optimization steps were almost identical. Single layer cells were optimized for comparison purposes to the Au nanoparticle incorporated solar cells discussed in Chapter 4. Figure 3.10 also shows a curve from pre-optimization (black), three curves from during the optimization, (red), and five curves of optimized cells (blue). The optimized cells were fabricated back to back with no poor performing cells in between.

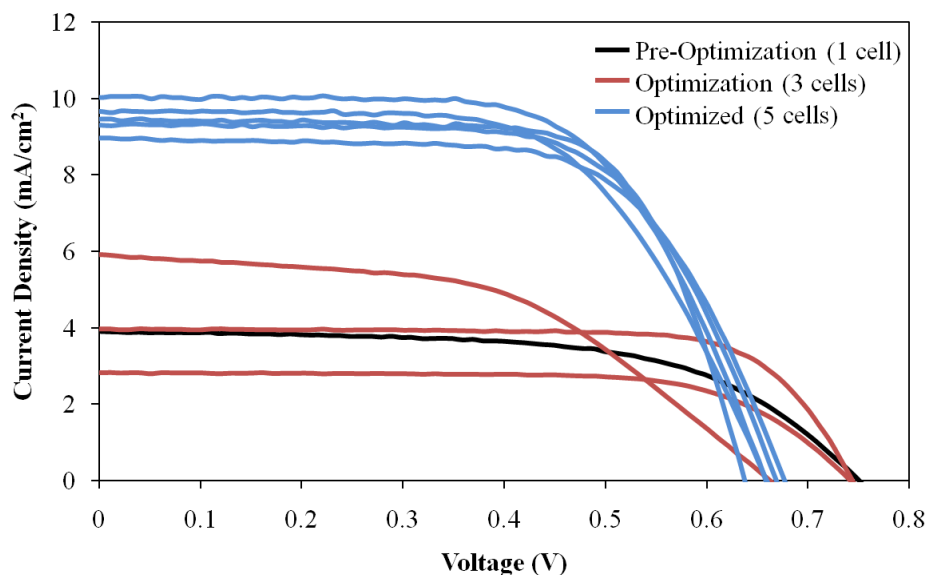


**Figure 3.10 IV Curves - Optimization of Single Layer GSCs**

**Single layer GSCs were optimized in the same manner as the double layer devices. Using the fully optimized fabrication steps with a four hour relaxation period, single layer GSCs of modest efficiencies were reproducibly fabricated.**

### *Noncritical Optimizations*

Other optimizations were tested along the way but none showed a substantial difference in device performance such as the four steps discussed above. The other steps tested were the dye-loading time (to increase short-circuit current), the annealing temperature (improve inter-particle connectivity i.e. series resistance), using reactive ion etching (RIE) cleaning instead of solvent cleaning (improve paste adherence to substrate), and the paste application & taping methods (improve paste uniformity/reduce cracking). The only optimization of these noncritical ones that could be considered borderline critical is the dye-loading time. With the dye N719 dye

employed, a dye-soaking time of at least 12-24 hours is required (1 layer vs. 2 layer) but the dye exposure time for both single and double layer GSC's should not really exceed much more than the 24 hour period or decreased photocurrents may arise due to the adsorption/desorption of dye molecules coming to an equilibrium and less dye molecules being chemisorbed due to the equilibrium being reached. Another note worthy step taken was to cease the use of any metallic (mainly steel) implements during the device fabrication. The iron cations ( $\text{Fe}^{3+}$ ) that would leach from the steel during the fabrication could have detrimental effects on the device performance, due to the oxides that form (quenchers) during the  $\text{TiO}_2$  paste sintering.<sup>7, 84-86</sup> This quenching effect (enhanced charge recombination) was not directly tested or observed in the devices presented here but to avoid any possibility of it, only plastic, glass, or Teflon coated lab utensils were employed.

### Further Device Characterizations

Various double and single layer GSCs were also characterized with the other photovoltaic characterization techniques. Figure 3.11 shows the IPCE for double & single layer GSCs. The IPCE for the devices correlates well with the measured IV curves in that the IPCEs for the double layer cells are higher than those of the single layer cells. The peak in the IPCE plots around 525 nm also correlates well with the maximum absorption peak (~530 nm) of the sensitizer used (N719). One discrepancy is that the IPCE plots do not always correlate well with the IV curves. A given cell may have a low short circuit current density while another cell (tested on a different day) has a higher short circuit density but the 2<sup>nd</sup> cell's IPCE is lower than the first's. The root of this discrepancy is under investigation.

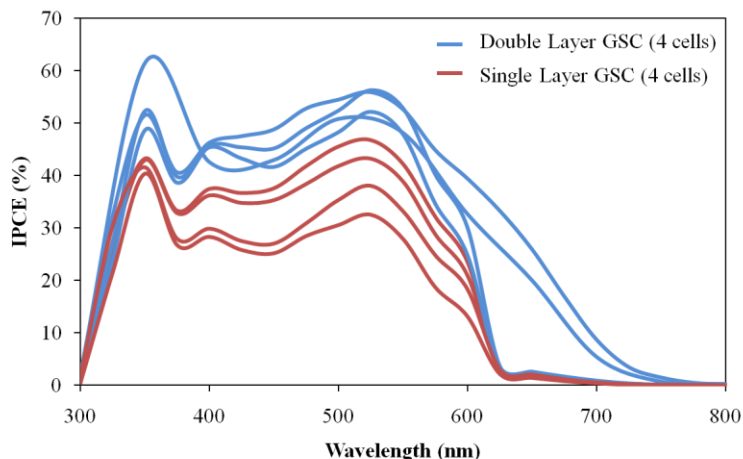


### Figure 3.11 IPCE - Double & Single Layer GSCs

The incident photon to current conversion efficiencies (IPCE) were collected for double and single layer GSCs. The three characteristic peaks (350 nm - TiO<sub>2</sub>, ~400 nm & 530 nm – dye) of the photoanode components were present. As expected the IPCE for double layer cells was higher than that of the single layer cells but large differences between individual devices within the groups was present. This discrepancy is under investigation.

The open circuit voltages (chronopotentiometry) and short circuit currents (chronoamperometry) under interrupted light conditions were also monitored for an extended period (~3 min). The results of a few cells are shown below in Figure 3.12 (open circuit voltage on the left and short circuit current on the right). Only two of the three minutes is shown for the chronoamperogram for ease of viewing. These plots show that both the open circuit voltages and the short circuit currents of the devices were stable. The chronoamperogram on the right also shows that the devices were not limited by electrolyte diffusion during operation (no photocurrent decay over time).

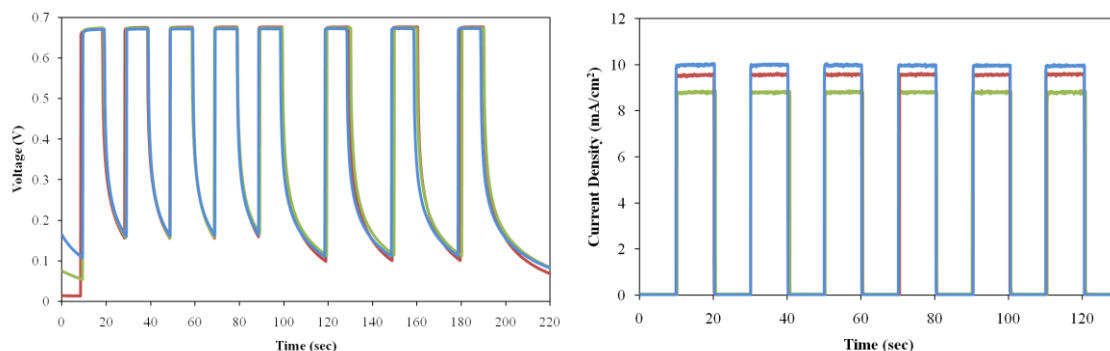


### Figure 3.12 GSC Illumination On/Off Measurements

The interrupted illumination measurements of the V<sub>OC</sub> and the J<sub>SC</sub> of the devices shows that the devices were stable during the testing period and the photocurrent is not limited by electrolyte diffusion.

Electrical impedance spectroscopy (EIS) was also conducted on a handful of the devices. As discussed earlier in the introduction, the spectra that is characteristic of a DSSC consists of three semicircles; charge transfer resistance at the counter electrode/electrolyte interface (1<sup>st</sup> semicircle), charge transfer resistance at the photoanode/dye/electrolyte interface (2<sup>nd</sup>

semicircle), & diffusion resistance (3<sup>rd</sup> semicircle). Due to the thin nature of the devices (not diffusion limited) and interference in the test frequency range, the diffusion resistance is not visible. The blue, green, and purple curves in the Nyquist plot (left plot) of Figure 3.13, which are very similar in impedance to one another, are from three of the optimized single layer GSCs. The red curve in the plot is one of the non-optimized single layer cells in Figure 3.10 (the IV curve with a  $J_{SC}$  of  $\sim 6 \text{ mA/cm}^2$  and a high series resistance). The high series resistance that is evident in the IV curve is also evident in the EIS spectra by the large impedance for both interfacial charge transfer resistances (semiconductor/dye/electrolyte & CE/electrolyte). While EIS can help confirm the results in the IV curve, it is also a very powerful tool for further characterization of the photovoltaic device such as the electron's lifetime in the photoanode (Table 3.3). In order to determine the electron lifetime, the test frequency is plotted vs. the phase angle (Bode phase plot – Figure 3.13 Right), and plugging in the frequency value of the peak phase angle (first peak in the bode phase plot) into the following equation,  $\tau_e = 1 / (2\pi f_{max})$ , will return the electron lifetime. The electron lifetimes for the three optimized cells are relatively close but the electron lifetime for the “non-optimized” cell is almost reduced by half. Due to the increased series resistance of the device, the flow of electrons would be hindered and recombinations are more likely i.e. shorter lifetime. The shorter lifetime would mean fewer charges are collected, resulting in a lower short circuit current density and therefore lower fill factor and efficiency, which is evident in the IV curve for this device (Figure 3.10).

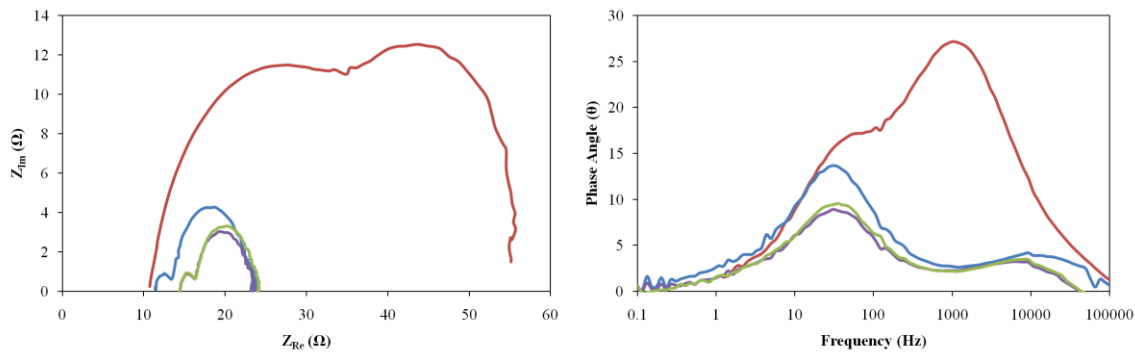


### Figure 3.13 EIS of GSCs – Nyquist Plot & Bode phase plot

Electrical impedance spectroscopy can give vital information into the charge transfer processes occurring within the device. The Nyquist and bode phase plots show similar results for three optimized cells (blue, green, and purple). The cause of the poor series resistance (IV curve with  $J_{SC}$  of  $\sim 6 \text{ mA/cm}^2$  in Figure 3.10) of the non-optimized cell (red) is evident after EIS. The impedance of the counter electrode and the photoanode are both substantially increased which leads to a shorter electron lifetime (Table 3.3) and reduced device performance.

Table 3.3 Electron Lifetimes in Photoanode

Red Curve		Blue Curve		Green Curve		Purple Curve	
$f_{\max}$ (Hz)	$\tau_e$ (ms)						
61.4	2.59	30.5	5.22	35.1	4.53	35.1	4.53

### Conclusions

Single and double layer GSCs were fabricated and optimized. Throughout the optimization process four critical parameters were realized; the transparent conductive oxide (TCO) employed, the method of the Pt application for the CE and its subsequent thickness, the period of time that the  $\text{TiO}_2$  paste was allowed to relax prior to sintering, and the integrity of the  $\text{TiCl}_4$  solution for the  $\text{TiCl}_4$  treatments. The underlying cause of the low device efficiencies was poor device series resistance. The optimization of the four critical parameters above (as well as other non-critical parameters) led to decreased series resistances, which in turn led to increased device performance. After the thorough optimizations, single layer GSCs with efficiencies  $>4\%$  and double layer GSCs with efficiencies around 6% (double layer) were obtained.

## Chapter 4 - Material Properties and Performance Effects of Dye-Sensitized Solar Cells (DSSC's) containing Au Nanoparticles (NPs)

As discussed in previous chapters an encouraging cheaper alternative to silicon solar cells are dye-sensitized solar cells (DSSC) which are based on a wide band gap semiconductor sensitized with a visible light absorbing species. While DSSCs are less expensive, their efficiencies are still quite low compared to silicon. Recently, the incorporation of metallic nanoparticles with plasmonic properties into silicon (and thin film) solar cells has been shown to improve the efficiency while also reducing the materials cost.<sup>35, 60, 61</sup> By utilizing these plasmonic properties, incident light can be scattered, concentrated, or trapped thereby increasing the effective path length of the cell and allowing the physical thickness of the cell to be reduced.<sup>56, 57,</sup><sup>87</sup> This concept can also be applied to DSSCs. Recently, DSSCs modified with Ag and Au nanoparticles have shown photocurrent and efficiency enhancements but without taking proper care in device design, the modification can have adverse effects.<sup>31, 32, 34, 62-64</sup> Similar results were obtained in our lab in which Au nanoparticle incorporated DSSC's showing short circuit current and efficiency effects (enhancements, no effect, or detrimental) were fabricated but these effects were found to be highly sensitive to the amount of Au nanoparticles present and the stability of the AuNPs in  $I_3^-/I^-$  solution.

### *Device Rationale*

These light harvesting properties of metal nanoparticles were applied to single layer GSCs. Figure 4.1 shows a schematic diagram of the dye-sensitized solar cell design, which has Au nanoparticles placed at the FTO/TiO<sub>2</sub> interface.

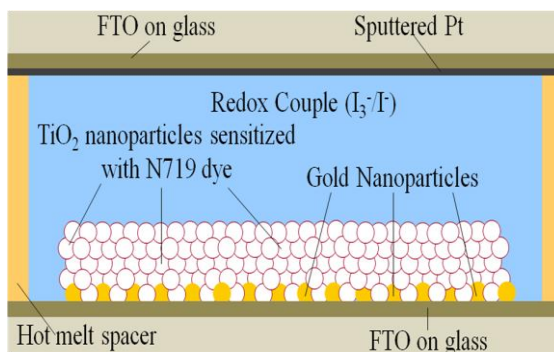


### Figure 4.1 AuNP Incorporated DSSC Design

The AuNP incorporated device is essentially a single layer GSC with 20 nm AuNPs placed at the TiO<sub>2</sub>/FTO interface.

Utilizing the light concentration effect of the metal nanoparticles (the 2<sup>nd</sup> geometry discussed in Figure 1.10 in the introduction), 20 nm Au particles were placed at the FTO/semiconductor interface to act as sub wavelength antennas, generating a high electric field around the nanoparticles, which hopefully will couple to the dye and increase its effective absorption cross section. The 20 nm particles were chosen due to the overlap of the employed sensitizer's (N719) peak absorption wavelength (~530 nm) and the surface plasmon resonance of the Au particle (~515 nm). (Figure 4.2) If the two absorption peaks begin to shift apart (larger nanoparticles), the coupling between the nanoparticle and the dye may decrease, which may decrease the dye's effective absorption cross section.

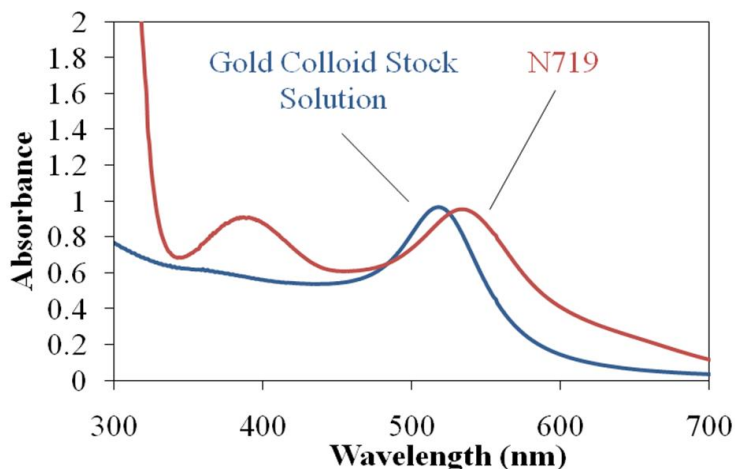
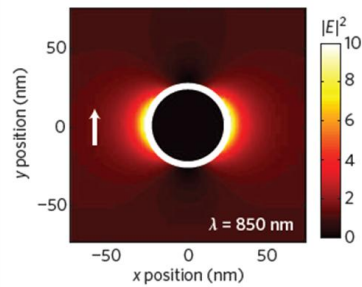


Figure 4.2 UV-Vis Absorption of Au NP Solution & Sensitizer (N719)

Due to the sensitizer employed (N719 -  $\lambda_{\text{max abs}} = 530 \text{ nm}$ ), AuNPs (20 nm) exhibiting a surface plasmon resonance near this wavelength were chosen to ensure the coupling of the nanoparticle and dye.

This crucial coupling between nanoparticle & dye arises from the presence of the intense electric field present around the particle and in the vicinity of the absorbed dye molecules. Figure 4.3 shows this high field enhancement (white ring) around a 25 nm Au nanoparticle (black circle), excited by 850 nm light.<sup>56</sup>



**Figure 4.3 Electric field enhancement around metallic nanoparticle<sup>56</sup>**

**A coupling between the dye and nanoparticle arises due to a intense electric field enhancement around the nanoparticle. The coupling would hopefully increase the photocurrent of the devices which should in turn lead to increased efficiencies. (Used with permission from ref. 56. Copyright © 2010 Nature Publishing Group)**

The strong field enhancement (of a few nanometers thick) is present around the entire particle with a decreasing field reaching out from the x-axis of the particle. Using this field enhancement around the particle, the plasmon resonance should be coupled to the sensitizer, which would hopefully increase the photocurrent of the devices and in turn led to increased cell efficiencies.

Ideally, a uniformly dispersed coverage of Au nanoparticles would be achieved. The nanoparticles should be close enough for the plasmons to couple to the dye and other neighboring nanoparticles but far enough apart that no deconstructive effects arise. Due to the improvement in the effective scattering and absorption cross sections, which can reach ten times the geometrical area, only ~10% surface coverage would be sufficient for most of the incident light to be captured.<sup>56</sup> Enhancements were indeed seen for some devices, even with large surface coverages (up to ~ a monolayer). In the initial studies, gold nanoparticles were applied to the FTO substrate by drop-casting or spin-casting methods but due to aggregation and non-uniformities arising during dewetting, the precision was quite poor. Since the nanoparticle deposition was so unpredictable but enhancements were shown for some devices (Figure D.1 - Appendix D), other deposition options were explored. Recently, it was shown that gold nanoparticles can be easily functionalized to ITO through a silane linker.<sup>88</sup> Following this concept, gold nanoparticles were functionalized to FTO substrates and DSSCs were assembled. An average photocurrent enhancement of 14% (maximum up to ~32%) and an average efficiency

enhancement of 13% (maximum up to ~23%) were realized with the larger enhancements arising from devices with lower surface coverages. However, controlling the degree of functionalization and the degree of aggregation of the nanoparticles proved to be difficult, which caused the measured photocurrent from device to device to be highly variable (enhancement vs. no enhancement for same surface coverages). Figure 4.4 shows the photovoltaic performance of the AuNPSCs vs. GSCs.

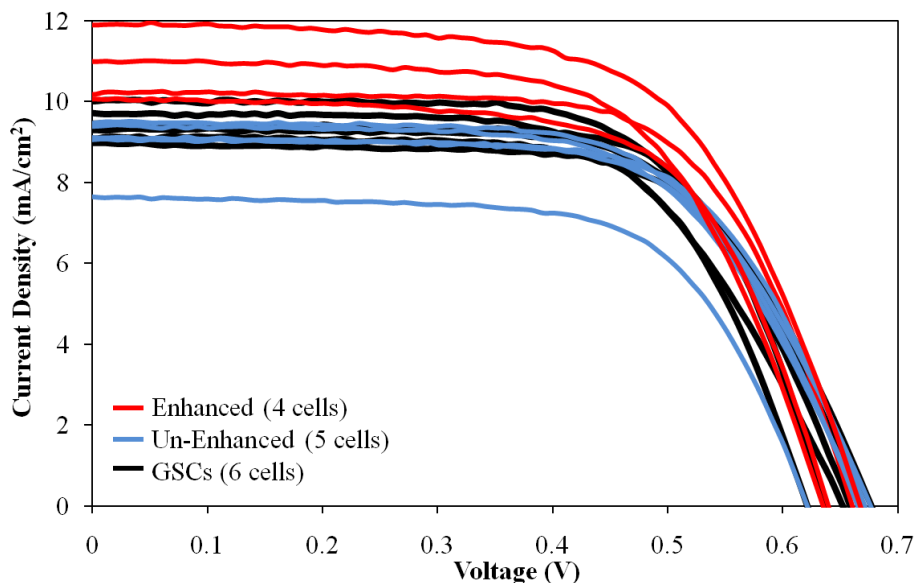


**Figure 4.4 IV Curves – AuNPSCs Enhanced vs. Un-enhanced**

**AuNP incorporated devices exhibited both favorable and adverse effects when compared to the performance of single layer GSCs. The devices were grouped into enhanced cells (higher photocurrent than GSC) and un-enhanced cells (similar or lower photocurrent than GSC). The effects on the photocurrent were extremely sensitive to the nanoparticle coverage and dispersion, with well dispersed, lower surface coverage devices exhibiting the highest photocurrent enhancements.**

The solar cells tested are grouped into three categories: GSCs, AuNPSCs – Non-enhanced, and AuNPSCs – Enhanced. Table 4.1 shows the averaged (including 99% confidence intervals) open circuit voltages ( $V_{OC}$ ), short circuit currents ( $J_{SC}$ ), fill factors (FF), efficiencies ( $\eta$ ), and resistances (shunt & series) for all these cells. There were no significant changes in the  $V_{OC}$ , FF, or series resistances between the GSCs and the AuNPSCs. There were improvements in the shunt resistances of the AuNP incorporated cells but due to the relatively unchanged  $V_{OC}$  the

increase in shunt resistance had marginal effects on the performance. Improvements were seen in the  $J_{SC}$  and since the series resistances also remained unchanged, the photocurrent enhancements can be attributed to the concentration of light by the AuNP plasmons. With all the other device parameters besides the photocurrent remaining unchanged, the overall device efficiencies were increased as well. There was ~14% enhancement between the averaged  $J_{SC}$  values and ~13% enhancement between the averaged  $\eta$ . The averaged  $J_{SC}$  and  $\eta$  for the un-enhanced cells were slightly lower than that of the GSCs due to the low performing (highly aggregated) cell. In general, a low functionalization (little to no aggregation) provided the best enhancement while a moderate to high functionalization (high aggregation) provided little to no enhancement or even a reduction. (discussed further in a latter section).

**Table 4.1 Photovoltaic Properties AuNPSCs - Enhanced vs. Non-Enhanced**

	$V_{OC}$ (V)	$J_{SC}$ (mA/cm <sup>2</sup> )	FF	$\eta$ (%)	$R_{SH}$ (k $\Omega$ )	$R_S$ (k $\Omega$ )
<b>GSCs</b>	0.652 ±0.021	9.43 ±0.41	0.654 ±0.032	4.02 ±0.18	6.6 ±5.2	0.0136 ±0.0029
<b>Non-Enhanced AuNPSCs</b>	0.661 ±0.025	8.94 ±0.86	0.649 ±0.019	3.84 ±0.45	12.5 ±22.8	0.0146 ±0.0020
<b>Enhanced AuNPSCs</b>	0.651 ±0.020	<b>10.8</b> <b>±1.1</b>	0.646 ±0.026	<b>4.53</b> <b>±0.40</b>	12.6 ±19.2	0.01125 ±0.00096

## AuNP DSSC's Synthesis and Assembly

### *Device Fabrication*

All FTO substrates used were diced into 2 cm x 2.5 cm pieces from a larger FTO coated glass piece (TEC8 glass, Dyesol, Queanbeyan NSW, Australia & Pilkington, Toledo, Ohio, USA).

### *Gold Nanoparticle Photoanode*

Two different methods of application of the Au NPs were tested: casting and functionalization. Schematic representations of these methods are given below and are followed by a detailed explanation of the application processes.

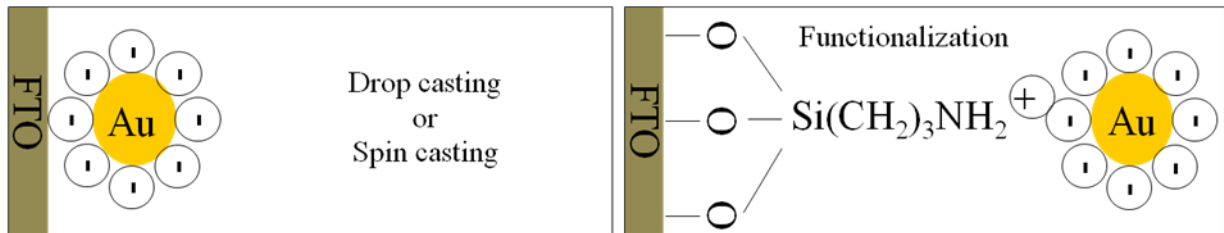


**Figure 4.5 Schematic of the AuNP Application Methods**

**Two different application methods were used for the deposition of the AuNPs; casting (drop or spin) and functionalization. For the casting methods the AuNPs were just applied directly to the FTO substrate. In order to functionalize the FTO surface, a silane linker that would electrostatically interact with the AuNPs, was covalently bound to the FTO substrate and then the AuNPs were applied to the silanized FTO.**

#### *Casted*

The FTO substrates (Dyesol & Pilkington) were consecutively sonicated in 20 mL of 0.1M HCl in absolute ethanol, 20 mL of isopropyl alcohol, & 20 mL acetone for ~20 min each and dried upright at 60°C. The volumes used increased per number of substrates sonicated; ~20 mL for two, ~40 mL for four, ~60 mL for six, etc. The substrates were then treated with the ice-bath prepared 40mM aqueous solution of TiCl<sub>4</sub> (~100 mL) at 70°C for 40 min. After TiCl<sub>4</sub> treatment, the substrates were rinsed with deionized water and acetone and dried upright at 60°C. The substrates were subjected to various casting methods of the Au nanoparticles; drop-casting and spin-casting. For the samples that were drop-casted, the substrate was placed onto a hot plate at 60°C. 200 μL of the stock Au nanoparticle solution was pipetted onto the substrate and allowed to dry. For the samples that were spin-casted, various spin rates were tested (2000, 1000, 500, 100 rpm). Any speed faster than 100 rpm appeared to spin the particles off the substrates, so only 100 rpm was consecutively used. To spin-coat Au nanoparticles onto the substrates, the samples were placed into the spin coater and 100 μL of the stock Au nanoparticle solution was pipetted onto them. The samples were spun at 100 rpm for 45 sec and at ~20 sec an additional 100 μL was pipetted onto the substrate. The samples were then dried at on a hot plate at 60°C.

### ***Functionalized***

The FTO substrates (Pilkington) were submerged in a 1% aqueous solution of  $\text{NH}_4\text{OH}$  under magnetic stirring at  $80^\circ\text{C}$  for 1 hr to ensure an active hydroxyl layer. The substrates were then rinsed with deionized water and dried at  $60^\circ\text{C}$ . Once dry, the substrates were refluxed under magnetic stirring in a 10% solution of (3-aminopropyl) triethoxysilane (APTS) in dry toluene for 30 min, rinsed with toluene, acetone, and deionized water, and dried at  $60^\circ\text{C}$ . Using a Teflon cell and an o-ring, the silanized substrates were subjected to gold nanoparticle solutions of varying nanoparticle concentrations and were immersed for several time periods so that different amounts of gold nanoparticles were functionalized to the FTO surface. The stock gold nanoparticle solution (Sigma Aldrich, Gold Colloid Solution, 20nm) was calculated to contain  $\sim 3.7 \times 10^{11}$  AuNPs/mL. Some substrates were subjected to 1 mL of the stock solution for 1, 2, 3, & 4 hours, with the 1 mL being swapped out for a fresh 1 mL (due to the solution turning colorless) at the 2 hr mark for the 3 & 4 hr soakings. Other substrates were subjected to 200  $\mu\text{L}$  of stock solution, 66  $\mu\text{L}$  stock solution diluted to 200  $\mu\text{L}$  with DI water, and 22  $\mu\text{L}$  stock solution diluted to 200  $\mu\text{L}$  with DI water for 2 hours each. After functionalization, all substrates were rinsed with DI water and dried at  $60^\circ\text{C}$ .

### ***Photoactive Layer Application and Sensitization***

Once dry, a window was made on the substrates (casted & functionalized) using Scotch® Magic Tape and  $\text{TiO}_2$  paste (Dyesol, DSL 18NR-T) was applied over the window using the doctor blade technique. The tape was removed and the paste was allowed to relax for  $\sim 4$  hours. The  $\text{TiO}_2$  coated substrates were placed into a tube furnace, dried at  $50^\circ\text{C}$  and  $70^\circ\text{C}$  for 15 min, and then sintered at  $525^\circ\text{C}$  for 30 min. Once the substrates had cooled to  $\sim 80^\circ\text{C}$ , they were subjected to another 40mM  $\text{TiCl}_4$  treatment ( $\sim 100\text{mL}$ ) at  $70^\circ\text{C}$  for 30 min. The substrates were rinsed with deionized water and absolute ethanol and dried at  $60^\circ\text{C}$ . The sintered  $\text{TiO}_2$  substrates were placed back into the tube furnace, dried at  $50^\circ\text{C}$  and  $70^\circ\text{C}$  for 15 min and then annealed at  $500^\circ\text{C}$  for 30 min.<sup>78</sup> The substrates were cooled to  $70^\circ\text{C}$  to avoid any water adsorption and then were soaked in a 0.5mM solution of N719 dye (Solaronix, Ruthenium 535-bisTBA) in acetonitrile:t-butyl alcohol (1:1v) for 12 hours in the dark at room temperature. After soaking, the sensitized photoanodes were briefly soaked ( $< 2$  min) in absolute ethanol followed by a

rinsing with absolute ethanol and then were dried at 60°C. The sensitized photoanodes were stored in the dark at room temperature until cell assembly took place.

### ***Platinum Counter Electrode***

A 0.75 mm hole was drilled into each piece of FTO glass using a Dremel® drill and a diamond drill bit. The substrates were consecutively sonicated in absolute ethanol, isopropyl alcohol, & acetone for ~20 min each and dried upright at 60°C. The substrates were mounted to a sample holder for an ion beam coater and blown off with nitrogen gas before being inserted into the ion beam coater (Gatan Model 681 High Resolution Ion Beam Coater). 50 nm of Pt was sputtered onto the substrates at a rate of ~1.5Å/sec, a rocking angle of 7° at 8 rocks/sec, and 30 rotations per minute.

### ***Device Assembly***

The sensitized photoanodes and the Pt counter electrodes were sealed together with a 25µm hot melt spacer (Solaronix, SX 1170-25PF). A window was cut into the hot melt spacer with a gap between the sensitized TiO<sub>2</sub> and the spacer of ~2 mm. The electrodes and hot melt spacer were pieced together and held in place with a 1” binder clip. The electrode assemblies were placed in an oven at 60°C; the temperature was ramped to 110°C over ~10 min, held at 110°C for ~5 min, and the oven was allowed to cool via natural convection. Once cooled, a tube adaptor (10-32 Coned NanoPort™ Assemblies, Product N-333) was affixed over the hole in the platinum counter electrode using epoxy and the epoxy was cured. Right before characterization, electrolyte (Solaronix, Iodolyte AN-50) was injected into the cell via vacuum filling.

### ***Photoanode & Device Characterization***

The photoanodes were characterized with UV-Vis and FESEM. The fully assembled devices were characterized with IV curves (Dark & Light), IPCE, EIS, Chronoamperometry, & Chronopotentiometry. The thickness of a single tape layer of TiO<sub>2</sub> film was characterized with FESEM (Hitachi S-3400 N) and found to be ~5µm. The Grätzel cell photoanodes were characterized with UV-Vis (Beckman DU 640 Spectrophotometer) throughout the device construction (before TiO<sub>2</sub> application, after the 2<sup>nd</sup> annealing of TiO<sub>2</sub>, and after dye soaking). The Au nanoparticle photoanodes were characterized with FESEM (FEI Nova NanoSEM 430) right after Au nanoparticle casting or functionalization and UV-Vis was collected throughout

device construction (before and after Au nanoparticles subjection, after the 2<sup>nd</sup> annealing of TiO<sub>2</sub>, and after dye soaking). The fully assembled devices were characterized with a solar simulator system from Newport Corporation. All IV curves, IPCE, and Chronopotentiometry were collected using a source measure unit (SMU) from Agilent (SMU #U2722A). EIS were collected with a potentiostat from Princeton Applied Research (PARSTAT 2273) and Chronoamperometry was completed with a potentiostat from CH Instruments (CHI440A Electrochemical Analyzer). Once assembled, the devices were first characterized with a dark IV (-0.2 V to 0.75 V) at 0.01 V/s followed by consecutive dark sweeps from 0.2 V to 0.75 V at 0.001 V/s. Due to the instrument design, sensitivity levels, and the variation in the dark current of the devices, the sensitivity level was changed as the sweeps were collected from 0.2 V to 0.75 V. For the first dark sweep from 0.2 V to ~0.3 V, the sensitivity was set at 10  $\mu$ A; from ~0.3 V to ~0.45 V, the sensitivity was set at 100  $\mu$ A; from ~0.45 V to ~0.58 V, the sensitivity was set at 1 mA; and from ~0.58 V to 0.75 V the sensitivity was set at 10 mA.

After all the dark curves were collected, two IV curves (-0.2 V to 0.75 V) were collected (~30 sec between collections) under 1 sun (100 mW/cm<sup>2</sup>) using a 300 W OF Xe lamp and an AM1.5G filter. The device was then placed in front of the Newport monochromatic light setup [75 W OF Xe lamp, motorized monochromator (#74004)] and the incident photon to current (IPCE), or external quantum efficiency, (EQE) was obtained. A third IV curve was collected under 1 sun irradiance to test for any cell degradation after EQE collection. Electrical impedance spectroscopy (EIS) was conducted on the devices to fit them to an electrical circuit as well as determine the electron lifetimes. EIS was performed in a frequency range of 100 mHz to 100 kHz (100 data points collected) with a AC potential of 10 mV rms overlaid. Using a shutter (Newport model #71445) to interrupt the incident light, chronoamperometry (CHI) and chronopotentiometry (Agilent) were conducted on the devices. For the chronoamperometric tests, a potential of 0 V (short circuit conditions) was applied to the devices and the resulting photocurrent was measured under dark & light conditions. The measurement began with the device under dark conditions for 10 sec; then the shutter was held open for 10 sec and 10 sec alternations of dark/light were conducted for a total 3 minutes. For the chronopotentiometric tests, a current of 0 A (open circuit conditions) was applied to the devices and the resulting photovoltage was measured under dark & light conditions. The measurement began with the device under dark conditions for 10 sec; then the shutter was held open for 10 sec and 10 sec

alternations of dark/light were conducted for a total of 1.5 minutes. At 1 min 30 seconds, the shutter was opened for 10 sec and then left closed for 20 sec to investigate the decay of the photovoltage over a longer time period (due to some devices decaying very slowly). After 3 minutes, the shutter was opened one last time for 10 seconds and then the photovoltage decay was monitored up to 4 minutes (50 seconds), to ensure that the photovoltage had returned to dark conditions. A fourth IV curve was collected under 1 sun irradiance to again test for any cell degradation. For some of the devices, the IV characteristics were measured at different light intensities (1 sun, 0.5 sun, 0.25 sun). Using a neutral density (ND) filter (Newport #FSQ-ND03), the incident power density was reduced by half to achieve 0.5 sun and an IV curve was collected under these conditions. Leaving the ND filter in the light path, the applied power to the lamp was reduced from 330 Watts to 190 Watts in order to achieve 0.25 sun. Again an IV curve was collected under these incident light conditions. For the devices characterized with varying light intensities, one final IV curve at 1 sun irradiance was collected to again test the stability of the solar cell.

### **Device Characterizations**

To obtain a clearer picture into the AuNP functionalization, the samples were imaged with FESEM. The AuNPSCs were divided into three different categories; high surface coverage (>20%), medium surface coverage (10-20%), and low surface coverage (<10%). Figure 4.6 shows the extent of functionalization for two different samples; one of medium surface coverage (~15%) and one of low surface coverage (~1.6%). Additional SEM images of high (>20%) and low surface coverages (~5%) are provided in (Figure D.2 – Appendix D). For surface coverages >20%, large aggregated groups of NPs were present with hardly any discontinuity between the aggregated NP groups. In the minimal areas of little aggregation, NPs were nicely dispersed with ~5-20 AuNPs clustered together in the aggregate. Despite the inconsistencies in the NP functionalization, the ratio of little aggregation area compared to high aggregation area was quite low, which gave rise to low to no performance enhancement. Even for medium surface coverages (10% - 20%) and for the middle of low surface coverages (5%), high NP aggregation was present. The decrease in the extent of aggregation correlated well with the decrease in surface coverage but as the surface coverage decreased, the areas of well dispersed, isolated NPs or NP clusters also decreased. It wasn't until the surface coverage decreased to ~2%, that the

areas of “aggregation” consisted almost solely of spatially isolated single NPs. Despite this spatial distribution between particles, the NPs still aggregated together leaving a lot of exposed FTO which can be attributed to the low surface coverage and the non-uniform spatial distribution.

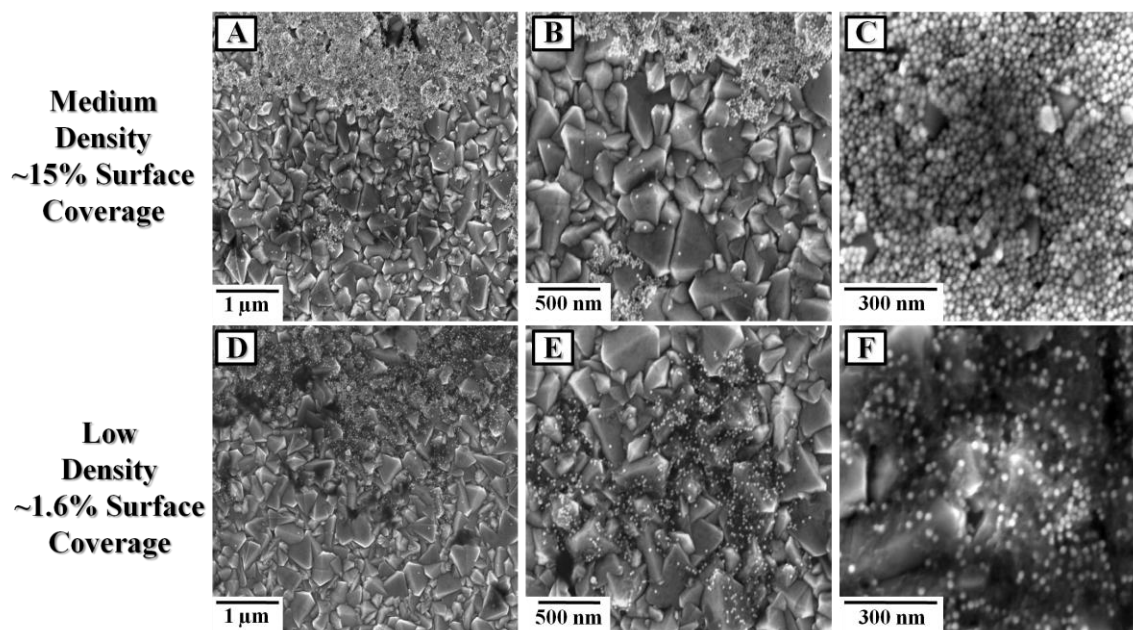


**Figure 4.6 FESEM of AuNP Functionalization – Medium & Low NP Densities**

(A) , (B), & (C) are of ~15% surface coverage and (D), (E), & (F) are of ~1.6% surface coverage at different magnifications. Well dispersed AuNPs were observed at low density surface coverages of about 2% while at higher surface coverages, large aggregates of NPs were visible.

UV-Vis spectroscopy was also conducted on the AuNP functionalized samples. (Figure 4.7) In general, the surface coverages correlated well with the UV-Vis spectra, in that the lower surface coverages gave rise to more light transmitted (less NPs present, less light absorbed).

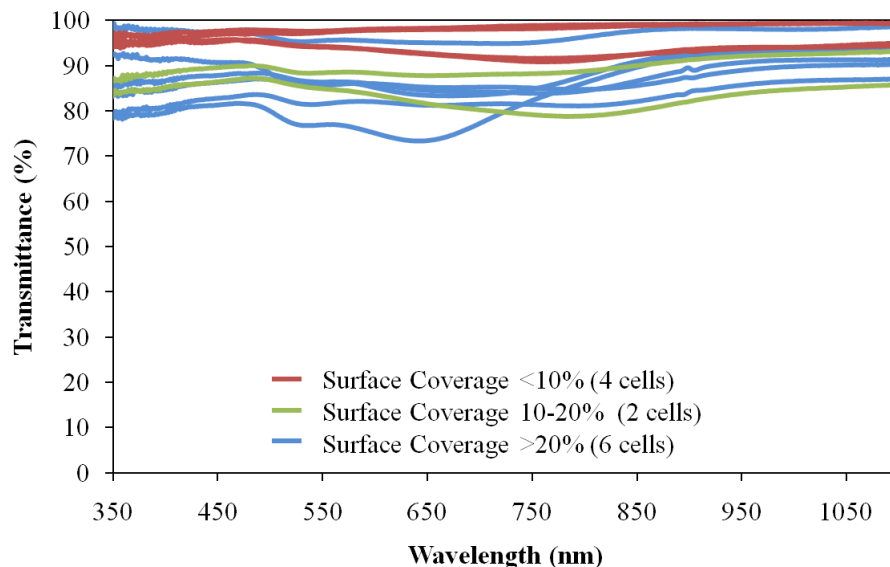


**Figure 4.7 UV-Vis Spectra AuNP Photoanodes**

**The AuNPs absorb <20% of incident photons which is highly desired; if the AuNPs absorb too much light, less light will reach the dye to generate photocurrent. As expected, higher surface coverage generally showed lower transmittance. Due to functionalization inconsistencies and aggregation, large deviations in the amount of transmitted light are present.**

Due to the inconsistencies in the functionalization and aggregation of the NPs, not all of the high density photoanodes gave similar percentages of light transmitted. Some of these devices absorbed comparable amounts of light to medium surface coverages and even low surface coverages. The logical thinking, though, was that the more nanoparticles present on the substrate, the more the incident light would be absorbed. The general trend of the UV-Vis spectra is in good agreement with this thinking, as well as the SEM images. Also, even the high surface coverages, only absorb <20% of the incident light which is highly desired. Due to the device thickness, if the AuNPs absorbed too much of the incident light, then not enough would reach the sensitized photoanode and a reduction in current would most likely arise due to the light being quenched by the NPs.

As discussed above, the AuNP functionalized samples were assembled into DSSC's and compared with GSC's. Figure 4.4 above showed clear photocurrent (& efficiency) enhancements, which was believed to be from the plasmon/dye coupling, but it is also apparent

that devices with no-enhancement or decreased performance occurred as well. Due to the functionalization inconsistencies and poor reproducibility of device performance, no concrete conclusion that the DSSCs were plasmon enhanced could be made, which shifted the concern more to the materials properties (surface coverages and chemical stability) of the device and not the plasmonic effects. The IV curves presented in Figure 4.4 were regrouped into the same surface coverage groups used to differentiate the samples for FESEM and UV-Vis. Figure 4.8 displays these regrouped IV-Curves.

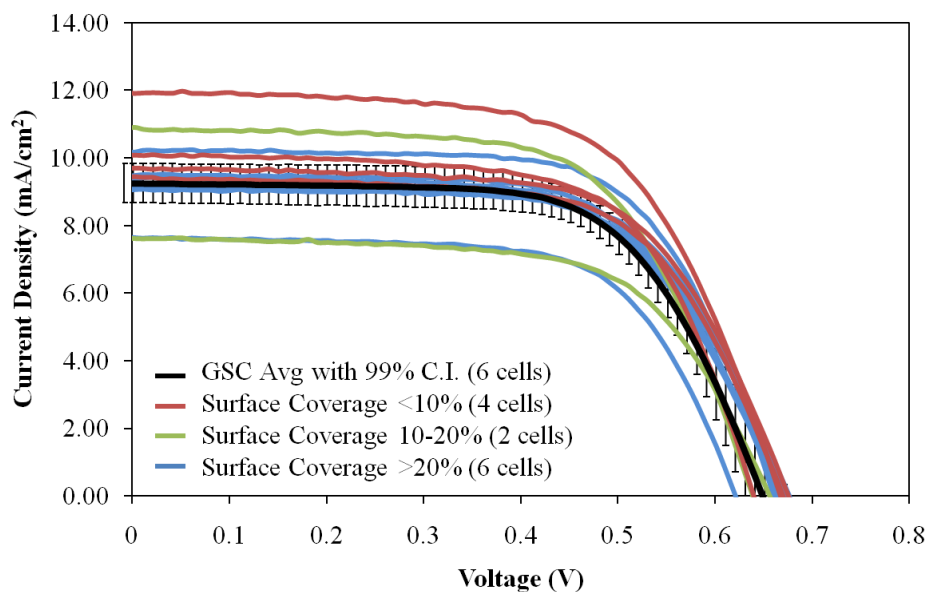


**Figure 4.8 IV Curves - AuNP Surface Coverage**

**The AuNP incorporated devices were re-grouped by their surface coverages. In general, devices with lower surface coverages, which had less aggregated particles, gave higher photocurrent enhancements. Large deviations in device performances between similar surface coverages were apparent. The deviations were attributed to the inconsistencies in the functionalization and aggregation of the NPs.**

AuNPSCs show clear photocurrent enhancements vs. the reference GSCs (99% C.I.s) which were likely due to the plasmonic effect of the Au NPs but the performances were highly sensitive to the nanoparticle aggregation, with the photocurrents varying with the distribution of the NPs. The general trend though is that the lower Au NP surface coverages gave larger enhancements. This trend is further confirmed by the light intensity dependence studies

presented in Figure 4.11. The top three curves in Figure 4.8, have photocurrent enhancements in descending order of surface coverages (>20% coverage  $\rightarrow$   $\sim 10$  mA/cm<sup>2</sup>, 10-20% coverage  $\rightarrow$   $\sim 11$  mA/cm<sup>2</sup>, <10% coverage  $\rightarrow$   $\sim 12$  mA/cm<sup>2</sup>). Only one other device, which had a low surface coverage, showed a slight enhancement. Figure 4.8 clearly shows the functionalization inconsistencies and poor device reproducibility (due to former). The photocurrents of a majority of the low surface coverage devices and high surface coverage devices fall right around the photocurrents of the GSCs. Despite the grouping right around the GSCs, the general enhancement trend (lower NP coverage = large photocurrent) can still be seen. None of the photocurrents of the low surface coverage devices falls below the GSC average, while a majority of the high surface coverage devices remain below the GSC average with a medium coverage and high coverage device both showing  $\sim 19\%$  (vs. GSC avg.) reduction in photocurrent (9.42 mA/cm<sup>2</sup> to 7.62 mA/cm<sup>2</sup>).

While the particle aggregation and functionalization inconsistencies were issues under investigation and are currently still being explored, the biggest concern with the devices that needed to be addressed was the effect of the electrolyte on the Au NPs. The iodide/tri-iodide (Solaronix, Iodolyte AN-50) electrolyte employed is highly corrosive to Au and Ag nanoparticles.<sup>63</sup> Recently, Hupp et. al. showed that without a pinhole free protective layer ( $\sim 8$  nm) of TiO<sub>2</sub> over Ag NPs, then the iodide/tri-iodide redox couple had detrimental effects on the integrity of the NPs, completely etching them away.<sup>63</sup> As discussed in Chapter 3, the TiCl<sub>4</sub> treatment of the TiO<sub>2</sub> photoanode increases the surface roughness and particle necking due to deposition of TiO<sub>2</sub> at the TiO<sub>2</sub> nanoparticle junctions.<sup>82</sup> Since the AuNP photoanodes were subjected to the same treatment, a thin layer of TiO<sub>2</sub> should have been deposited around the NPs as well, materializing the question, is this thin layer of TiO<sub>2</sub> enough to protect the Au NPs from the corrosive nature of the electrolyte? Experiments were designed with the following treatments: 1) Thermal, 2) TiCl<sub>4</sub>, 3) Electrolyte. The effects of all these treatments are visible in the FESEM images in Figure 4.9 below and Figure D.3 in Appendix D.

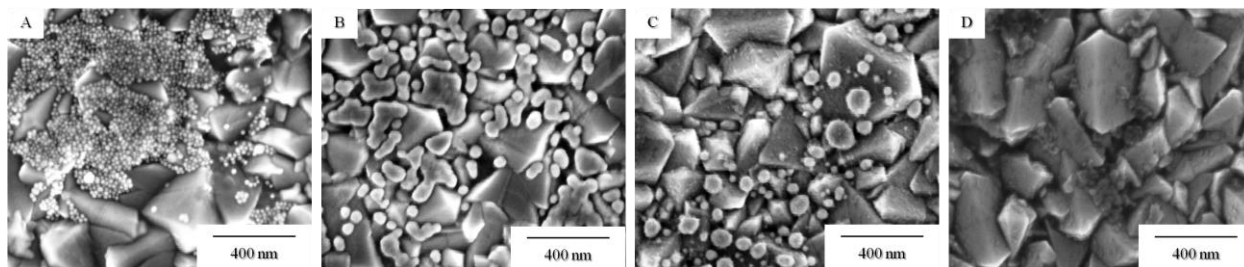


### **Figure 4.9 FESEM - Thermal & Electrolyte Treatments Effects**

**Upon thermal treatment of the AuNP functionalized substrates, the NPs lose their stabilizing ligand which causes them to fuse together into bigger particles (B). Due to the variability in functionalization and the high degree of aggregation, this fusing of particles could lead to large films of Au on the sample and in turn have adverse effects. Another issue is the corrosive nature electrolyte employed ( $I/I_3^-$ ). When the substrates are subjected to the  $TiCl_4$ , a thin layer of  $TiO_2$  is deposited over the surface (C) which ideally would shield the NPs from the corrosive electrolyte but as is evident in (D), after electrolyte treatment only AuNP remnants remain, indicating poor device stability.**

Figure 4.9a shows the as-functionalized AuNPs (~1.6% surface coverage). The AuNPs are more aggregated than previous 1.6% surface coverage samples and are not as well-dispersed, which is attributed to the functionalization inconsistencies. From Figure 4.9b, the criticality of the NPs being spatially distributed is apparent. During the thermal treatment, the organic stabilizing ligand of the AuNPs decomposes, destabilizing the NPs causing them to fuse together into larger particles (up to hundreds of nanometers). If there is a high surface coverage of AuNPs, then the particles will melt together and could potentially form a thin film (nanometers thick) over the entire (or a large portion of the) FTO surface, which would absorb the incident light, quenching the device. The presence of this thin film could be the cause of the observed photocurrent reductions. Due to the variations in nanoparticle functionalization, some samples would contain a higher amount of NPs than others, leading to variations in the formation of the fused particles which would give rise to deviations in the observed photocurrents. The AuNPs were then subjected to a  $TiCl_4$  treatment which deposited what is believed to be a thin layer of  $TiO_2$  onto the surface as can be seen in Figure 4.9c. The AuNPs lastly were exposed to the electrolyte. Figure 4.9d shows that the  $TiCl_4$  treatment did not generate a thick enough  $TiO_2$  protective layer to keep the AuNPs from being etched. Remnants of particles can be seen but no intact particles were found. Upon close inspection of Figure 4.9a & b, it is clear that the  $TiCl_4$  treatment deposited some sort of material (assuming  $TiO_2$ ) onto the FTO and over the AuNPs but it wasn't enough material to protect the NPs from the corrosive electrolyte. Before further efforts are invested into the functionalization inconsistencies, the devices need to be stable by including an appropriate protecting layer over the AuNPs.

In order to further understand the observed photocurrent effects (enhancement, no effect, reduction), the incident photon to current conversion efficiencies (IPCE) were collected. Figure 4.10 shows the IPCE for the cells tested (not all were tested with IPCE). The cells are grouped into the same surface coverage categories as previous figures.

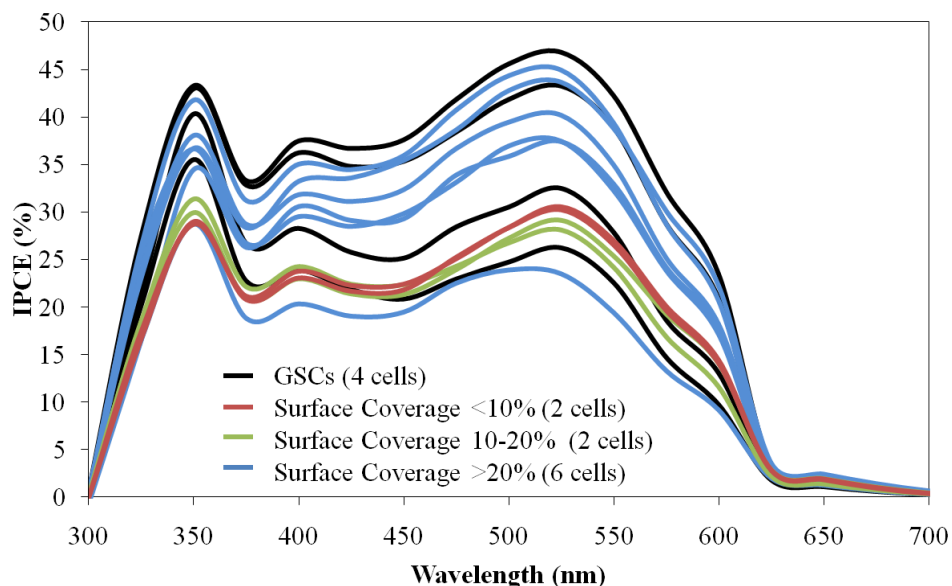


**Figure 4.10 IPCE – AuNPSCs**

**To better understand the photocurrent effects, the incident photon to current conversion efficiencies were assessed on various cells. Similar trends to the IV curves in Figure 4.8 were expected but the exact opposite was observed. The lower surface coverage cells generally gave lower IPCE than the higher surface coverage cells and the GSCs. The speculation is that the plasmonic effects are not as prominent at the low light intensities used for the IPCE.**

What was expected was an overall increase in the IPCE for the enhanced cells, while the un-enhanced cells remain virtually unchanged when compared to the GSCs. This was not the case; no general trends were really observed and the lower surface coverage devices (generally larger enhancement) actually displayed low IPCE. The large variance in IPCE could be due to the low light intensities used for the measurement (on the order 10's of  $\mu\text{W}$ ). Further investigations were completed by measuring IV curves at different irradiances (1 sun, 0.5 sun, & 0.25 sun) to see if the photocurrent difference vs. a GSC would drop below zero at low light intensities. (Figure 4.11)

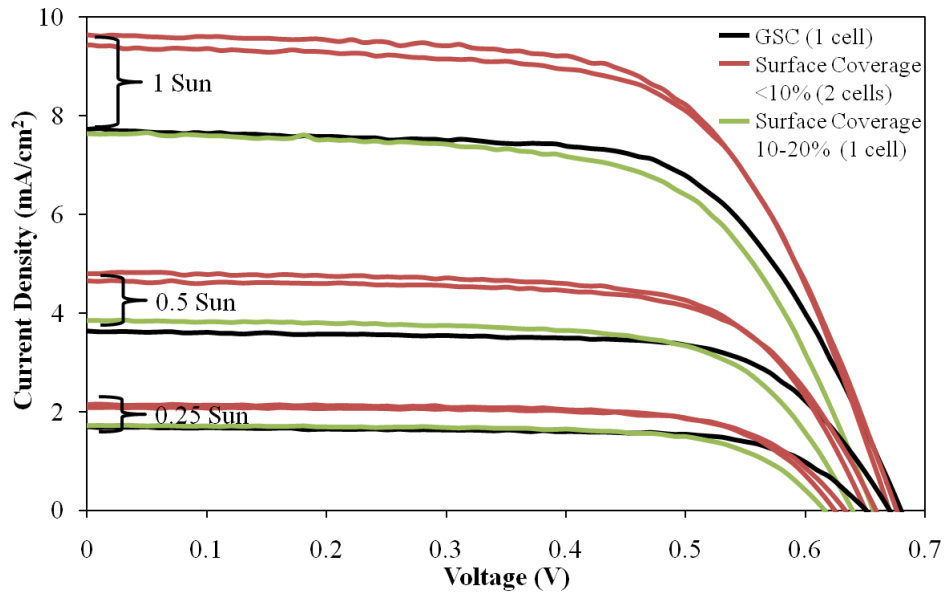


**Figure 4.11 IV Curves - AuNPSCs Performance At Different Light Intensities**

To investigate the observed IPCE phenomena, the IV responses of AuNPSCs of different surface coverages were measured at lower light intensities (1 sun, 0.5 sun, 0.25 sun). The general trend of lower surface coverages giving larger enhancements is again confirmed.

Figure 4.11 again verifies the general trend that lower surface coverages led to higher photocurrent enhancements. Devices with surface coverages of ~1.6% and 5% gave similar enhancements while the device with a surface coverage of ~15% gave essentially no enhancement. The resulting photocurrents were extracted and the photocurrent density differences between the AuNPSCs and GSCs were calculated with the following formula:

$$[(J_{SC, AuNPSC} - J_{SC, GSC}) / J_{SC, GSC}] * 100$$

The photocurrent density differences were then plotted vs. the incident light intensity (Figure 4.12).

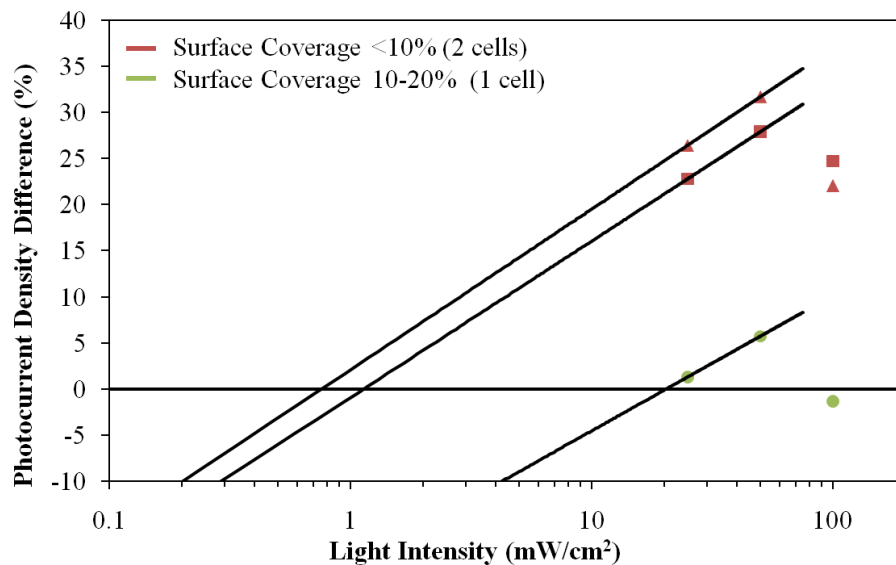


**Figure 4.12 Photocurrent Density Differences of AuNPSCs vs. GSCs**

The short circuit current densities from Figure 4.11 were extracted and the percent difference between the AuNPSCs and the GSC was calculated. Plotting this difference vs. the log scale of the light intensity shows that at lower light intensities the photocurrent difference drops below zero, meaning that at low incident light the plasmonic effects are likely non-beneficial and could actually have quenching effects.

This plot shows that as the light intensity decreases the photocurrent density difference also decreases meaning that the plasmonic effects may not be as strong (if present at all) at lower light intensities; upon extrapolating the light intensity to about  $60 \mu\text{W}/\text{cm}^2$ , which is the approximate light intensity used for the IPCE measurement, the photocurrent differences drop to negative values. This is indicative of possible adverse optical effects, such as quenching, at low incident light intensities.

### Additional Characterizations

Further device characterizations, such as IPCE (devices in Figure 4.11), Chronoamperometry/potentiometry, were also performed (Figures D.4 & D.5 - Appendix D).

### Conclusions

DSSC's containing metal nanoparticles (Au) at the FTO/photoanode interface were fabricated in attempts to exploit the plasmonic properties of the metal particles. By incorporating these AuNPs into the DSSCs, dramatic effects on the photocurrent were observed. Photocurrent

enhancements up to 32% vs. GSCs are possible with an average enhancement of 14% which led to an average efficiency enhancement of 13% (maximum up to ~23%). The effects of the AuNPs on the devices highly depend on the dispersion & surface coverage. Photocurrent reductions of ~19% were actually observed for some devices with higher surface coverages. These reductions and also the non-effected photocurrents are attributed to the functionalization inconsistencies and too high of a surface coverage, which would absorb too much light, quenching the device. The detrimental effects of the thermal treatment on a high surface coverage could be the cause of the observed photocurrent reductions. The functionalization of the AuNPs provides more control over NP deposition than casting methods but the functionalization & AuNP dispersion still needs to be improved & optimized for a high-performance plasmonic DSSC. Before this can be done though, the survivability of the AuNPs needs to be increased by incorporating a protection layer. With the AuNP dispersion optimized and a protection layer in place, reproducible enhancements of at least 32% should be achievable.

## Chapter 5 - Overall Conclusions and Future Outlook

In conclusion, a solar simulator system was acquired, installed and calibrated, single layer and double layer GSCs were optimized to efficiencies of 4% and 6% respectively, and AuNP incorporated DSSCs showing photocurrent reductions and enhancements (up to 32% increase) were fabricated. In order to calibrate the solar simulator system, the two lamps (broadband and monochromatic) in the system were aligned and the incident power densities were made as uniform as possible. Incident power density variations of less than 10% difference over 15 mm in x and y directions were achieved for both light sources. By additional fine-tunings of the lamp alignment and beam collimation, the power density uniformity could be further improved, decreasing the power density variations to less than 10% difference over 20+ mm. To certify that the solar simulator system was properly calibrated, a Si reference cell (with certification tracing to NREL) was employed.

With a calibrated solar simulator system in place, photovoltaic devices could be fabricated and reliably tested. The end goal was to fabricate new DSSC architectures and/or new device designs (such as the incorporation of NPs displaying plasmonic properties), investigating any new, interesting phenomena along the way but before this goal could be tackled, a consistent standard solar cell needed to be established for comparison purposes. The solar cell chosen for this was the benchmark DSSC based on  $\text{TiO}_2$  nanoparticles also known as the “Grätzel Cell” (GSC). In order to establish the standard, single and double layer GSCs were fabricated and optimized. Four critical fabrication parameters were ascertained during the optimization process. These parameters were the transparent conductive oxide (TCO) employed, the method of the Pt application for the CE and its subsequent thickness, the period of time that the  $\text{TiO}_2$  paste was allowed to relax prior to sintering, and the integrity of the  $\text{TiCl}_4$  solution for the  $\text{TiCl}_4$  treatments. Initially the devices were plagued by poor performances (photocurrent, fill factor, efficiency) which were caused by poor device series resistances. Through the optimization of the four critical parameters above (as well as other non-critical parameters) decreased series resistances were obtained, which in turn led to increased device performances. After the thorough optimizations, single layer GSCs with efficiencies  $>4\%$  and double layer GSCs with efficiencies around 6% (double layer) were reliably fabricated.

Having a steadfast benchmark for comparison, further device improvements, such as increasing the light harvesting capabilities through plasmonic exploitation, could be attempted. To do this, DSSC's containing metal nanoparticles (Au) placed at the FTO/photoanode interface were fabricated. The incorporation of these AuNPs into the DSSCs caused dramatic effects on device performance. Photocurrent enhancements up to 32% vs. GSCs with an average enhancement of 14% were observed. The photocurrent enhancements led to an average efficiency enhancement of 13% (maximum up to ~23%). While enhancements were obtained, photocurrent reductions of ~19% were also observed. The effects (enhancement/reduction) of the AuNPs on the devices highly depended upon the dispersion & surface coverages of the NPs. In general, the enhancements arose from lower NP surface coverages while the larger surface coverages caused reductions or little to no effect but the performance reproducibility for devices with the same surface coverage was inadequate. These large variations in the obtained photocurrents can be attributed to NP aggregation and functionalization inconsistencies. When the particles were highly aggregated ( $\uparrow$  surface coverage =  $\uparrow$  aggregation) fusing of the NPs due to the thermal treatments occurs. This fusing effect and the inconsistent NP deposition are believed to be the root cause of the observed photocurrent variations. If the NP deposition can be better controlled so that the particles are uniformly dispersed, then the fusing effect may no longer even be a concern, solving both problems at once. By functionalizing the AuNPs to the substrate as opposed to just casting them, more control over the deposition was achieved. The consistency of the functionalization & the AuNP dispersion still need to be improved & optimized to obtain a high-performance plasmonic DSSC. Before this can be done though, the survivability of the AuNPs needs to be increased by incorporating a protection layer. In the future, different thickness (5 nm to 20 nm) of TiO<sub>2</sub>, deposited by metalorganic chemical vapor deposition (MOCVD), can be tested as a shielding layer against the corrosive electrolyte. Once proper protection is achieved, various steps can be taken to try and optimize the functionalization. Some of these steps include polishing the rough FTO surface (hopefully reducing the aggregation in the large crystal crevices), conduct the functionalization in a glove box (silanization step is highly water sensitive; may give better functionalization), and upon the AuNP attachment step, place the AuNP functionalized substrate in the vertical position vs. the horizontal to avoid any potential sedimentation. With the AuNP dispersion optimized and a protection layer in place, reproducible enhancements of at least 32% should be achievable.

## References

1. Various Authors. 1973 Oil Crisis. [http://en.wikipedia.org/wiki/1973\\_oil\\_crisis#Secondary\\_effects](http://en.wikipedia.org/wiki/1973_oil_crisis#Secondary_effects) (8/4/11),
2. Various Authors. World Energy Consumption. [http://en.wikipedia.org/wiki/World\\_Energy](http://en.wikipedia.org/wiki/World_Energy) (8/2/2011),
3. Mierlo, F. v., World Energy Consumption. In Wikipedia: 2006.
4. Omegatron, World Energy Usage Width Chart. In Wikipedia: 2007.
5. Nazelrod, S., Remaining Oil. In Wikipedia: 2008.
6. Delphi234, Available Energy. In Wikipedia: 2008.
7. Ito, S.; Murakami, T. N.; Comte, P.; Liska, P.; Grätzel, C.; Nazeeruddin, M. K.; Grätzel, M., Fabrication of thin film dye sensitized solar cells with solar to electric power conversion efficiency over 10%. *Thin Solid Films* **2008**, 516, (14), 4613-4619.
8. Kroon, J. M.; Bakker, N. J.; Smit, H. J. P.; Liska, P.; Thampi, K. R.; Wang, P.; Zakeeruddin, S. M.; Gratzel, M.; Hinsch, A.; Hore, S.; Wurfel, U.; Sastrawan, R.; Durrant, J. R.; Palomares, E.; Pettersson, H.; Gruszecki, T.; Walter, J.; Skupien, K.; Tulloch, G. E., Nanocrystalline dye-sensitized solar cells having maximum performance. *Progress in Photovoltaics* **2007**, 15, (1), 1-18.
9. Lai, Y. H.; Lin, C. Y.; Chen, H. W.; Chen, J. G.; Kung, C. W.; Vittal, R.; Ho, K. C., Fabrication of a ZnO film with a mosaic structure for a high efficient dye-sensitized solar cell. *Journal of Materials Chemistry* **2010**, 20, (42), 9379-9385.
10. Sauvage, F.; Di Fonzo, F.; Li Bassi, A.; Casari, C. S.; Russo, V.; Divitini, G.; Ducati, C.; Bottani, C. E.; Comte, P.; Graetzel, M., Hierarchical TiO<sub>2</sub> Photoanode for Dye-Sensitized Solar Cells. *Nano Letters* **2010**, 10, (7), 2562-2567.
11. Bukowski, T. J.; Simmons, J. H., Quantum dot research: Current state and future prospects. *Critical Reviews in Solid State and Materials Sciences* **2002**, 27, (3-4), 119-142.
12. Bavel, S. S. v.; Sourty, E.; With, G. d.; Loos, J., Three-Dimensional Nanoscale Organization of Bulk Heterojunction Polymer Solar Cells. *Nano Letters* **2009**, 9, (2), 507-513.
13. Carlidge, E., Bright outlook for solar cells. *Physics World* **2007**, 20, (7), 20-24.
14. Conibeer, G., Third-generation photovoltaics. *Materials Today* **2007**, 10, (11), 42-50.
15. Green, M. A., Third generation photovoltaics: Ultra-high conversion efficiency at low cost. *Progress in Photovoltaics* **2001**, 9, (2), 123-135.
16. Kim, J. Y.; Lee, K.; Coates, N. E.; Moses, D.; Nguyen, T.-Q.; Dante, M.; Heeger, A. J., Efficient Tandem Polymer Solar Cells Fabricated by All-Solution Processing. *Science* **2007**, 317, (5835), 222-225.
17. Liska, P.; Thampi, K. R.; Gratzel, M.; Bremaud, D.; Rudmann, D.; Upadhyaya, H. M.; Tiwari, A. N., Nanocrystalline dye-sensitized solar cell/copper indium gallium selenide thin-film tandem showing greater than 15% conversion efficiency. *Applied Physics Letters* **2006**, 88, (20).
18. Cheng, H.-M.; Chiu, W.-H.; Lee, C.-H.; Tsai, S.-Y.; Hsieh, W.-F., Formation of Branched ZnO Nanowires from Solvothermal Method and Dye-Sensitized Solar Cells Applications. *The Journal of Physical Chemistry C* **2008**, 112, (42), 16359-16364.

19. Liu, J.; Kuo, Y.-T.; Klabunde, K. J.; Rochford, C.; Wu, J.; Li, J., Novel Dye-Sensitized Solar Cell Architecture Using TiO<sub>2</sub>-Coated Vertically Aligned Carbon Nanofiber Arrays. *ACS Applied Materials & Interfaces* **2009**, 1, (8), 1645-1649.
20. Martinson, A. B. F.; Hamann, T. W.; Pellin, M. J.; Hupp, J. T., New architectures for dye-sensitized solar cells. *Chem. Eur. J.* **2008**, 14, (15), 4458-4467.
21. Arango, A. C.; Oertel, D. C.; Xu, Y.; Bawendi, M. G.; Bulović, V., Heterojunction Photovoltaics Using Printed Colloidal Quantum Dots as a Photosensitive Layer. *Nano Letters* **2009**, 9, (2), 860-863.
22. Kongkanand, A.; Tvrđy, K.; Takechi, K.; Kuno, M.; Kamat, P. V., Quantum dot solar cells. Tuning photoresponse through size and shape control of CdSe-TiO<sub>2</sub> architecture. *J. Am. Chem. Soc.* **2008**, 130, (12), 4007-4015.
23. Lee, H. J.; Yum, J. H.; Leventis, H. C.; Zakeeruddin, S. M.; Haque, S. A.; Chen, P.; Seok, S. I.; Grätzel, M.; Nazeeruddin, M. K., CdSe quantum dot-sensitized solar cells exceeding efficiency 1% at full-sun intensity. *J. Phys. Chem. C* **2008**, 112, (30), 11600-11608.
24. Nozik, A. J., Quantum dot solar cells. *Physica E-Low-Dimensional Systems & Nanostructures* **2002**, 14, (1-2), 115-120.
25. Brabec, C. J.; Sariciftci, N. S.; Hummelen, J. C., Plastic solar cells. *Advanced Functional Materials* **2001**, 11, (1), 15-26.
26. Huynh, W. U.; Dittmer, J. J.; Alivisatos, A. P., Hybrid nanorod-polymer solar cells. *Science* **2002**, 295, (5564), 2425-2427.
27. Peumans, P.; Uchida, S.; Forrest, S. R., Efficient bulk heterojunction photovoltaic cells using small-molecular-weight organic thin films. *Nature* **2003**, 425, (6954), 158-162.
28. Peumans, P.; Yakimov, A.; Forrest, S. R., Small molecular weight organic thin-film photodetectors and solar cells. *Journal of Applied Physics* **2003**, 93, (7), 3693-3723.
29. Veenstra, S. C.; Loos, J.; Kroon, J. M., Nanoscale structure of solar cells based on pure conjugated polymer blends. *Progress in Photovoltaics* **2007**, 15, (8), 727-740.
30. Po, R.; Maggini, M.; Camaioni, N., Polymer Solar Cells: Recent Approaches and Achievements. *The Journal of Physical Chemistry C* **2009**, 114, (2), 695-706.
31. Ding, I. K.; Zhu, J.; Cai, W.; Moon, S.-J.; Cai, N.; Wang, P.; Zakeeruddin, S. M.; Grätzel, M.; Brongersma, M. L.; Cui, Y.; McGehee, M. D., Plasmonic Dye-Sensitized Solar Cells. *Advanced Energy Materials* **2011**, 1, (1), 52-57.
32. Peh, C. K. N.; Ke, L.; Ho, G. W., Modification of ZnO nanorods through Au nanoparticles surface coating for dye-sensitized solar cells applications. *Materials Letters* **2010**, 64, (12), 1372-1375.
33. Fang-Chung, C.; Jyh-Lih, W.; Chia-Ling, L.; Yi, H.; Chun-Hong, K.; Michael, H. H., Plasmonic-enhanced polymer photovoltaic devices incorporating solution-processable metal nanoparticles. *Applied Physics Letters* **2009**, 95, (1), 013305.
34. Standridge, S. D.; Schatz, G. C.; Hupp, J. T., Distance Dependence of Plasmon-Enhanced Photocurrent in Dye-Sensitized Solar Cells. *Journal of the American Chemical Society* **2009**, 131, (24), 8407-8409.
35. Pillai, S.; Catchpole, K. R.; Trupke, T.; Green, M. A., Surface plasmon enhanced silicon solar cells. *J. Appl. Phys.* **2007**, 101, (9), 093105.
36. Larry Kazmerski, K. Z., Best Research Cell Efficiencies. In NREL: 2003.
37. Jones, M. R., Dye Sensitized Solar Cell Scheme. In Wikipedia: 2009.
38. Suzuki, K.; Yamaguchi, M.; Kumagai, M.; Yanagida, S., Application of carbon nanotubes to counter electrodes of dye-sensitized solar cells. *Chemistry Letters* **2003**, 32, (1), 28-29.

39. Fan, S. Q.; Fang, B.; Kim, J. H.; Kim, J. J.; Yu, J. S.; Ko, J., Hierarchical nanostructured spherical carbon with hollow core/mesoporous shell as a highly efficient counter electrode in CdSe quantum-dot-sensitized solar cells. *Applied Physics Letters* 96, (6), 3.
40. Fang, B.; Kim, M.; Fan, S. Q.; Kim, J. H.; Wilkinson, D. P.; Ko, J.; Yu, J. S., Facile synthesis of open mesoporous carbon nanofibers with tailored nanostructure as a highly efficient counter electrode in CdSe quantum-dot-sensitized solar cells. *Journal of Materials Chemistry* 21, (24), 8742-8748.
41. Fang, B. Z.; Fan, S. Q.; Kim, J. H.; Kim, M. S.; Kim, M.; Chaudhari, N. K.; Ko, J.; Yu, J. S., Incorporating Hierarchical Nanostructured Carbon Counter Electrode into Metal-Free Organic Dye-Sensitized Solar Cell. *Langmuir* 26, (13), 11238-11243.
42. Sayer, R. A.; Hodson, S. L.; Fisher, T. S., Improved Efficiency of Dye-Sensitized Solar Cells Using a Vertically Aligned Carbon Nanotube Counter Electrode. *Journal of Solar Energy Engineering-Transactions of the Asme* 132, (2), 4.
43. Wang, G. Q.; Huang, C. C.; Xing, W.; Zhuo, S. P., Micro-meso hierarchical porous carbon as low-cost counter electrode for dye-sensitized solar cells. *Electrochimica Acta* 56, (16), 5459-5463.
44. Li, D. M.; Li, H.; Luo, Y. H.; Li, K. X.; Meng, Q. B.; Armand, M.; Chen, L. Q., Non-Corrosive, Non-Absorbing Organic Redox Couple for Dye-Sensitized Solar Cells. *Advanced Functional Materials* 2010, 20, (19), 3358-3365.
45. Kuang, D. B.; Klein, C.; Zhang, Z. P.; Ito, S.; Moser, J. E.; Zakeeruddin, S. M.; Gratzel, M., Stable, high-efficiency ionic-liquid-based mesoscopic dye-sensitized solar cells. *Small* 2007, 3, (12), 2094-2102.
46. Gorlov, M.; Kloo, L., Ionic liquid electrolytes for dye-sensitized solar cells. *Dalton Transactions* 2008, (20), 2655-2666.
47. Bai, Y.; Cao, Y. M.; Zhang, J.; Wang, M.; Li, R. Z.; Wang, P.; Zakeeruddin, S. M.; Gratzel, M., High-performance dye-sensitized solar cells based on solvent-free electrolytes produced from eutectic melts. *Nature Materials* 2008, 7, (8), 626-630.
48. Wang, P.; Zakeeruddin, S. M.; Moser, J.-E.; Grätzel, M., A New Ionic Liquid Electrolyte Enhances the Conversion Efficiency of Dye-Sensitized Solar Cells. *J. Phys. Chem. B* 2003, 107, (48), 13280-13285.
49. Snaith, H. J.; Karthikeyan, C. S.; Petrozza, A.; Teuscher, J.; Moser, J. E.; Nazeeruddin, M. K.; Thelakkat, M.; Gratzel, M., High extinction coefficient "Antenna" dye in solid-state dye-sensitized solar cells: A photophysical and electronic study. *Journal of Physical Chemistry C* 2008, 112, (20), 7562-7566.
50. Hagberg, D. P.; Yum, J. H.; Lee, H.; De Angelis, F.; Marinado, T.; Karlsson, K. M.; Humphry-Baker, R.; Sun, L. C.; Hagfeldt, A.; Gratzel, M.; Nazeeruddin, M. K., Molecular engineering of organic sensitizers for dye-sensitized solar cell applications. *J. Am. Chem. Soc.* 2008, 130, (19), 6259-6266.
51. Gao, F.; Wang, Y.; Shi, D.; Zhang, J.; Wang, M. K.; Jing, X. Y.; Humphry-Baker, R.; Wang, P.; Zakeeruddin, S. M.; Gratzel, M., Enhance the optical absorptivity of nanocrystalline TiO<sub>2</sub> film with high molar extinction coefficient ruthenium sensitizers for high performance dye-sensitized solar cells. *J. Am. Chem. Soc.* 2008, 130, (32), 10720-10728.
52. Campbell, W. M.; Jolley, K. W.; Wagner, P.; Wagner, K.; Walsh, P. J.; Gordon, K. C.; Schmidt-Mende, L.; Nazeeruddin, M. K.; Wang, Q.; Gratzel, M.; Officer, D. L., Highly

- efficient porphyrin sensitizers for dye-sensitized solar cells. *Journal of Physical Chemistry C* **2007**, 111, (32), 11760-11762.
53. Kuang, D.; Ito, S.; Wenger, B.; Klein, C.; Moser, J. E.; Humphry-Baker, R.; Zakeeruddin, S. M.; Gratzel, M., High Molar Extinction Coefficient Heteroleptic Ruthenium Complexes for Thin Film Dye-Sensitized Solar Cells. *J. Am. Chem. Soc.* **2006**, 128, (12), 4146-4154.
  54. Schmidt-Mende, L.; Bach, U.; Humphry-Baker, R.; Horiuchi, T.; Miura, H.; Ito, S.; Uchida, S.; Gratzel, M., Organic dye for highly efficient solid-state dye-sensitized solar cells. *Advanced Materials* **2005**, 17, (7), 813-+.
  55. Nazeeruddin, M. K.; Klein, C.; Liska, P.; Gratzel, M., Synthesis of novel ruthenium sensitizers and their application in dye-sensitized solar cells. *Coordination Chemistry Reviews* **2005**, 249, (13-14), 1460-1467.
  56. Atwater, H. A.; Polman, A., Plasmonics for improved photovoltaic devices. *Nature Materials* **2010**, 9, (10), 865-865.
  57. Pillai, S.; Green, M. A., Plasmonics for photovoltaic applications. *Solar Energy Materials and Solar Cells* **2010**, 94, (9), 1481-1486.
  58. Kelly, K. L.; Coronado, E.; Zhao, L. L.; Schatz, G. C., The optical properties of metal nanoparticles: The influence of size, shape, and dielectric environment. *Journal of Physical Chemistry B* **2003**, 107, (3), 668-677.
  59. Mertz, J., Radiative absorption, fluorescence, and scattering of a classical dipole near a lossless interface: a unified description. *Journal of the Optical Society of America B-Optical Physics* **2000**, 17, (11), 1906-1913.
  60. Nakayama, K.; Tanabe, K.; Atwater, H. A., Plasmonic nanoparticle enhanced light absorption in GaAs solar cells. *Applied Physics Letters* **2008**, 93, (12).
  61. Mookapati, S.; Beck, F. J.; Polman, A.; Catchpole, K. R., Designing periodic arrays of metal nanoparticles for light-trapping applications in solar cells. *Appl. Phys. Lett.* **2009**, 95, (5), 053115.
  62. Hagglund, C.; Zach, M.; Kasemo, B., Enhanced charge carrier generation in dye sensitized solar cells by nanoparticle plasmons. *Applied Physics Letters* **2008**, 92, (1), 013113.
  63. Standridge, S. D.; Schatz, G. C.; Hupp, J. T., Toward Plasmonic Solar Cells: Protection of Silver Nanoparticles via Atomic Layer Deposition of TiO<sub>2</sub>. *Langmuir* **2009**, 25, (5), 2596-2600.
  64. Brown, M. D.; Suteewong, T.; Kumar, R. S. S.; D'Innocenzo, V.; Petrozza, A.; Lee, M. M.; Wiesner, U.; Snaith, H. J., Plasmonic Dye-Sensitized Solar Cells Using Core-Shell Metal-Insulator Nanoparticles. *Nano Letters* 11, (2), 438-445.
  65. Schlichthorl, G.; Huang, S. Y.; Sprague, J.; Frank, A. J., Band edge movement and recombination kinetics in dye-sensitized nanocrystalline TiO<sub>2</sub> solar cells: A study by intensity modulated photovoltage spectroscopy. *Journal of Physical Chemistry B* **1997**, 101, (41), 8141-8155.
  66. Schlichthorl, G.; Park, N. G.; Frank, A. J., Evaluation of the charge-collection efficiency of dye-sensitized nanocrystalline TiO<sub>2</sub> solar cells. *Journal of Physical Chemistry B* **1999**, 103, (5), 782-791.
  67. Kern, R.; Sastrawan, R.; Ferber, J.; Stangl, R.; Luther, J., Modeling and interpretation of electrical impedance spectra of dye solar cells operated under open-circuit conditions. *Electrochimica Acta* **2002**, 47, (26), 4213-4225.
  68. Mierlo, F. V., Breakdown of incoming solar energy. In Wikipedia: 2007.
  69. Rohde, R. A., Solar Spectrum. In Wikipedia: 2007.

70. Christiana Honsberg, S. B. PV Education - Air Mass.  
<http://www.pveducation.org/pvcdrom/properties-of-sunlight/air-mass> (8/4/2011),
71. Tachibana, Y.; Moser, J. E.; Gratzel, M.; Klug, D. R.; Durrant, J. R., Subpicosecond interfacial charge separation in dye-sensitized nanocrystalline titanium dioxide films. *Journal of Physical Chemistry* **1996**, 100, (51), 20056-20062.
72. Haque, S. A.; Tachibana, Y.; Willis, R. L.; Moser, J. E.; Gratzel, M.; Klug, D. R.; Durrant, J. R., Parameters influencing charge recombination kinetics in dye-sensitized nanocrystalline titanium dioxide films. *Journal of Physical Chemistry B* **2000**, 104, (3), 538-547.
73. Tachibana, Y.; Haque, S. A.; Mercer, I. P.; Moser, J. E.; Klug, D. R.; Durrant, J. R., Modulation of the rate of electron injection in dye-sensitized nanocrystalline TiO<sub>2</sub> films by externally applied bias. *Journal of Physical Chemistry B* **2001**, 105, (31), 7424-7431.
74. Katoh, R.; Fuke, N.; Furube, A.; Koide, N., Effect of dye coverage on photo-induced electron injection efficiency in N719-sensitized nanocrystalline TiO<sub>2</sub> films. *Chemical Physics Letters* **2010**, 489, (4-6), 202-206.
75. Wenger, B.; Gratzel, M.; Moser, J. E., Rationale for kinetic heterogeneity of ultrafast light-induced electron transfer from Ru(II) complex sensitizers to nanocrystalline TiO<sub>2</sub>. *Journal of the American Chemical Society* **2005**, 127, (35), 12150-12151.
76. Pellnor, M.; Myllyperkiö, P.; Korppi-Tommola, J.; Yartsev, A.; Sundström, V., Photoinduced interfacial electron injection in RuN<sub>3</sub>-TiO<sub>2</sub> thin films: Resolving picosecond timescale injection from the triplet state of the protonated and deprotonated dyes. *Chemical Physics Letters* **2008**, 462, (4-6), 205-208.
77. Katoh, R.; Furube, A.; Yoshihara, T.; Hara, K.; Fujihashi, G.; Takano, S.; Murata, S.; Arakawa, H.; Tachiya, M., Efficiencies of electron injection from excited N<sub>3</sub> dye into nanocrystalline semiconductor (ZrO<sub>2</sub>, TiO<sub>2</sub>, ZnO, Nb<sub>2</sub>O<sub>5</sub>, SnO<sub>2</sub>, In<sub>2</sub>O<sub>3</sub>) films. *Journal of Physical Chemistry B* **2004**, 108, (15), 4818-4822.
78. Vesce, L.; Riccitelli, R.; Soscia, G.; Brown, T. M.; Di Carlo, A.; Reale, A., Optimization of nanostructured titania photoanodes for dye-sensitized solar cells: Study and experimentation of TiCl<sub>4</sub> treatment. *Journal of Non-Crystalline Solids* **2010**, 356, (37-40), 1958-1961.
79. Frank, G.; Kostlin, H., ELECTRICAL-PROPERTIES AND DEFECT MODEL OF TIN-DOPED INDIUM OXIDE LAYERS. *Applied Physics a-Materials Science & Processing* **1982**, 27, (4), 197-206.
80. Lee, S.; Noh, J. H.; Bae, S. T.; Cho, I. S.; Kim, J. Y.; Shin, H.; Lee, J. K.; Jung, H. S.; Hong, K. S., Indium-Tin-Oxide-Based Transparent Conducting Layers for Highly Efficient Photovoltaic Devices. *Journal of Physical Chemistry C* **2009**, 113, (17), 7443-7447.
81. Ngamsinlapasathian, S.; Sreethawong, T.; Suzuki, Y.; Yoshikawa, S., Doubled layered ITO/SnO<sub>2</sub> conducting glass for substrate of dye-sensitized solar cells. *Solar Energy Materials and Solar Cells* **2006**, 90, (14), 2129-2140.
82. Ito, S.; Liska, P.; Comte, P.; Charvet, R. L.; Pechy, P.; Bach, U.; Schmidt-Mende, L.; Zakeeruddin, S. M.; Kay, A.; Nazeeruddin, M. K.; Gratzel, M., Control of dark current in photoelectrochemical (TiO<sub>2</sub>/I<sup>-</sup>-I<sup>-</sup>3(-)) and dye-sensitized solar cells. *Chemical Communications* **2005**, (34), 4351-4353.
83. Various Authors. Titanium Tetrachloride.  
[http://en.wikipedia.org/wiki/Titanium\\_tetrachloride](http://en.wikipedia.org/wiki/Titanium_tetrachloride) (8/4/2011),

84. Cherepy, N. J.; Liston, D. B.; Lovejoy, J. A.; Deng, H. M.; Zhang, J. Z., Ultrafast studies of photoexcited electron dynamics in gamma- and alpha-Fe<sub>2</sub>O<sub>3</sub> semiconductor nanoparticles. *Journal of Physical Chemistry B* **1998**, 102, (5), 770-776.
85. Ferrere, S.; Gregg, B. A., Large increases in photocurrents and solar conversion efficiencies by UV illumination of dye sensitized solar cells. *Journal of Physical Chemistry B* **2001**, 105, (32), 7602-7605.
86. Kay, A. Solar Cells Based on Nanocrystalline TiO<sub>2</sub> Electrodes. PhD Thesis, Ecole Polytechnique Fédérale de Lausanne, Switzerland, 1994.
87. Catchpole, K. R.; Polman, A., Design principles for particle plasmon enhanced solar cells. *Appl. Phys. Lett.* **2008**, 93, (19), 191113.
88. Chen, Z.; Zu, Y., Gold Nanoparticle-Modified ITO Electrode for Electrogenenerated Chemiluminescence: Well-Preserved Transparency and Highly Enhanced Activity. *Langmuir* **2007**, 23, (23), 11387-11390.

## Appendix A - Solar Simulation System

The numbering and lettering system presented here in Appendix A for the solar simulator schematics does not correlate with that used in Chapter 2. The schematics presented here are more detailed and therefore have a more extensive numbering than the simple one given in Chapter 2.

### System Breakdown

The Newport solar simulator system can be broken down into four basic categories in which each part of the system is placed. The four categories are broadband light source, monochromatic light source, electrochemical characterization instruments, and miscellaneous. While every component of the solar simulator system is included in the breakdown below, every item may not appear in the schematics.

#### I. Broadband light source

- A. 300 Watt Xenon (Ozone free) Arc Lamp – Model # 6258
- B. 500 Watt Lamp Housing – Model # 67005
- C. 300 Watt Lamp Socket Adapter – Model # 66160
- D. Lamp Power Supply – Model # 69911
- E. Power Supply to Housing Connecting Cable – Model # 70050
- F. Condensing Optics Holder – Model # 67015
- G. Fused Silica Focusing Lens – Model # 39313
- H. Multiple Filter Holder – Model # 62020
  - 1. Air Mass 1.5 Filter – Model # 81094
  - 2. Neutral Density Filter – Model # FSQ-ND03
- I. Light Source Shutter and Shutter Power Supply – Model # 71445
- J. Beam Turning Assembly (for directing beam downward) – Model # 66245
  - 1. Beam Turning Mirror – Model # 66215
- K. Thermal Power Sensor (Supplied by ThorLabs) – Model # S302C

- L. Power Meter (Supplied by Thorlabs) – Model # PM100D

#### II. Monochromatic light source

- A. Apex Monochromator Illuminator – Model # 70611
  - 1. Includes motorized filter wheel
    - a. 285 nm cut-on filter – Model # 51220
    - b. 550 nm cut-on filter – Model # 51302
    - c. 1000 nm cut-on filter – Model # 51362
- B. 75 Watt Xenon (Ozone free) Arc Lamp – Model # 6263
- C. Light Shield – Model # 70625
- D. Motorized Monochromator – Model # 74004
  - 1. 350 nm blaze grating – Model # 74024
  - 2. 750 nm blaze grating – Model # 74025
- E. Micrometer Driven Slits (x2) – Model # 74001
- F. Focusing Lens Assembly – Model # 77330

- G. Fused Silica Focusing Lens – Model # 39313
- H. UV Silicon Detector – Model # 71675
- I. Optical Power/Energy Meter – Model # 1936-C

**III. Electrochem. Characterization Instruments**

- A. Agilent Source Measure Unit – Model # U2722A
- B. CH Instruments Electrochemical Analyzer (previously acquired prior to simulator) – Model # CHI440A
- C. PARSTAT (previously acquired prior to simulator) – Model # 2273

**IV. Miscellaneous**

- A. 24” Optical Rail (x2) – Model # PRL-24
- B. 3” Rail Carrier – Model # PRC-3
- C. 50 mm Travel Vernier Micrometer (x2) – Model # SM-50

- D. 2” Travel Translation Stage (x2) – Model # 433
- E. 90° Angle Bracket – Model # 360-90
- F. 30” x 48” Workstation – Model # LW3048B-OPT
- G. ¼-20 Black Oxide Screw Kit – Model # SK-25A
- H. Standard 2” Rod (x8) – Model # 12312
- I. Standard 2” Rod Holder (x8) – Model # 14421
- J. TRACQ Basic Software – Model # 77890
- K. Configurable HP Compaq Microtower PC – Model # dx7500
- L. PV Measurements, Inc. 2 cm x 2 cm Calibrated Silicon Reference Cell

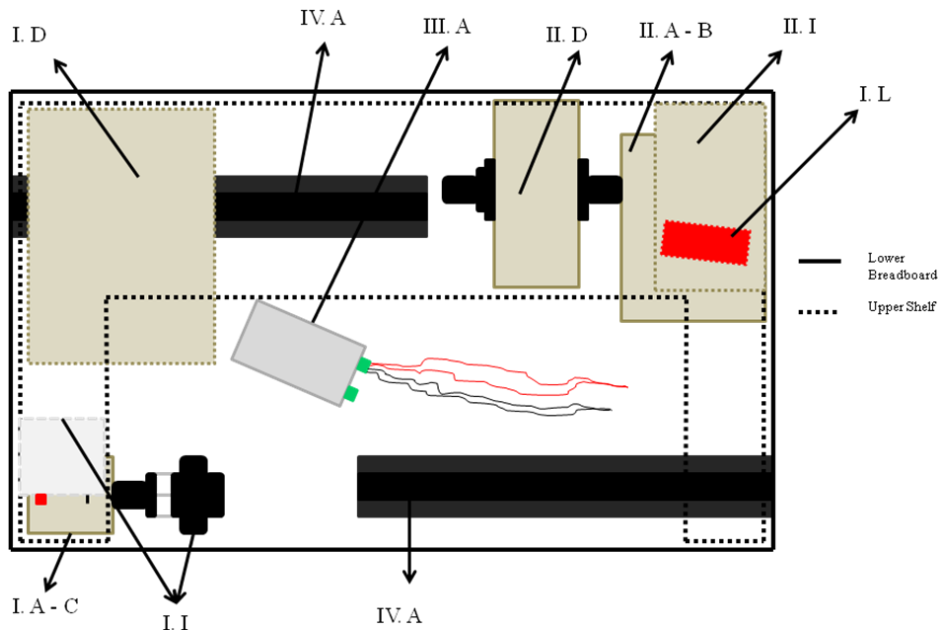


**Figure A.1 Solar Simulator System Complete Schematic**

**A complete schematic of the solar simulator setup including the components on the lower breadboard (laser table) and the upper shelf components (all in dotted lines).**

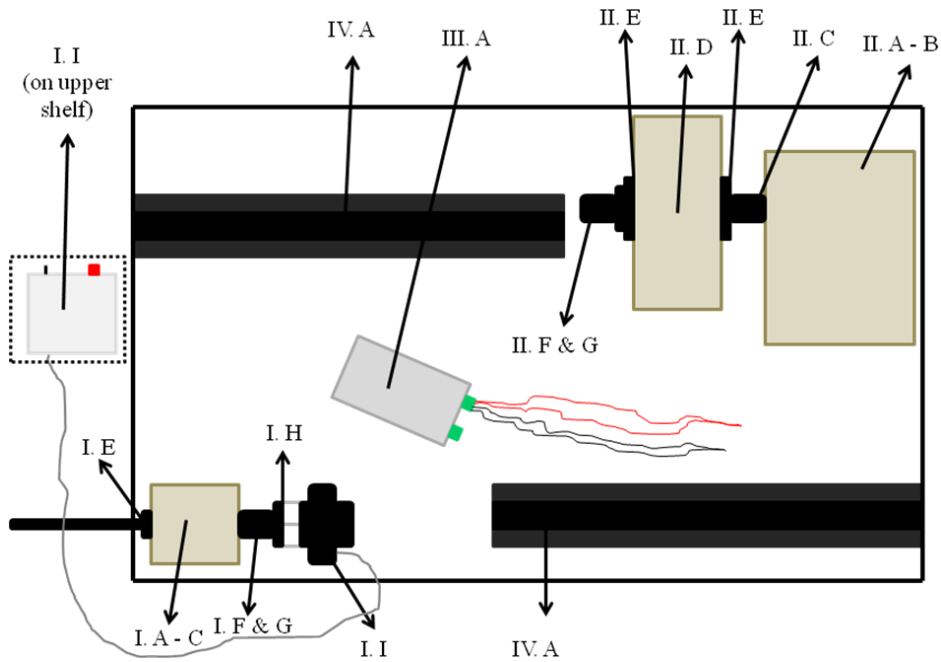


**Figure A.2 Solar Simulator Lower Breadboard Schematic**

The lower breadboard components consist of the two light sources, the monochromator, the motorized shutter, the sample tracks, and the source measure unit.

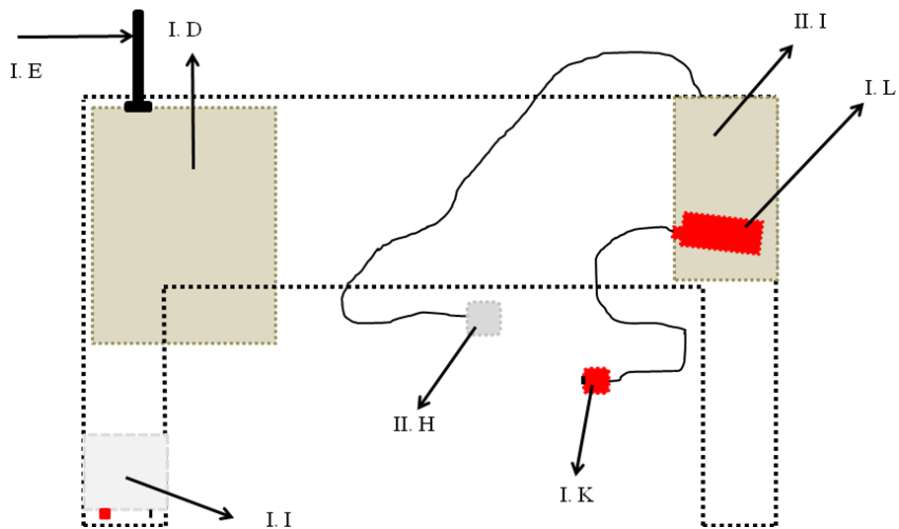


**Figure A.3 Solar Simulator Upper Shelf Schematic**

The components on the upper shelf consist of the 300 W lamp power supply, the motorized shutter power supply, and both detectors/power meters (broadband & monochromatic).

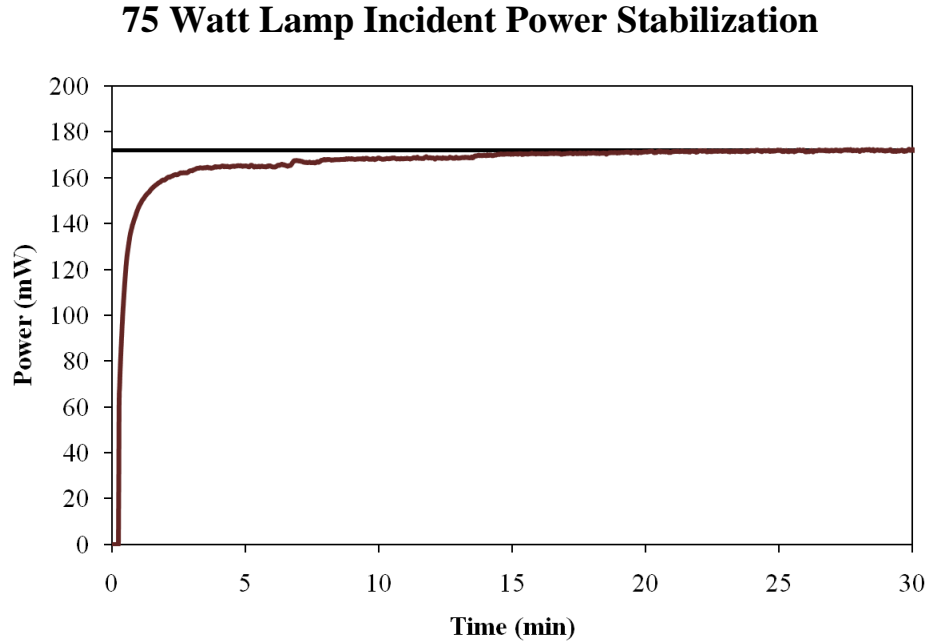


**Figure A.4 75 Watt Lamp Warm up Period**

Similar to the 300 W lamp, the 75 Watt Lamp requires at least a 15 minute warm up period to reach a moderately stable power output but a 30 minute time interval should be used to achieve full stabilization.

## Appendix B - Reference Cell Data Supplied by PV Measurements, Inc.

All data and curves provided in appendix B below are for the 2 cm x 2cm reference cell. The reference cell and calibration data were supplied by PV Measurements, Inc., Boulder, Colorado.

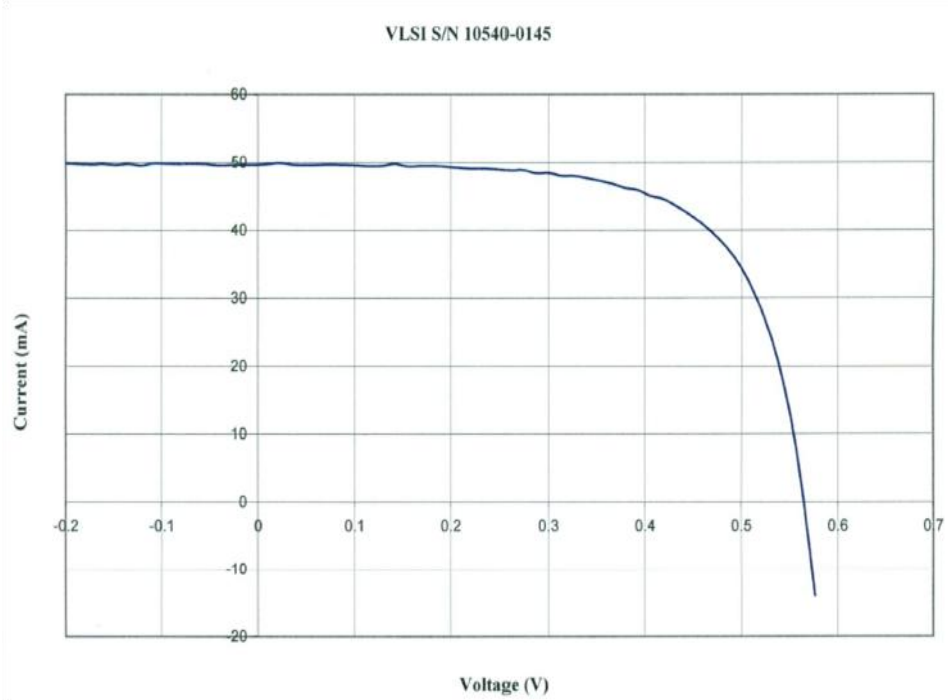


**Figure B.1 IV Curve for Calibrated Reference Cell**

**Table B.1 Certified Values for Si Reference Parameters**

Certified Values							
$I_{SC}$ (mA)	$J_{SC}$ (mA/cm <sup>2</sup> )	$V_{OC}$ (V)	FF (%)	$\eta$ (%)	$J_{max}$ (mA/cm <sup>2</sup> )	$V_{max}$ (V)	$P_{max}$ (mW/cm <sup>2</sup> )
49.7 ± 0.7	11.94	0.5639 ± 0.0032	67.3 ± 1.0	4.5 ± 0.1	10.21	0.4446 ± 0.0059	4.54

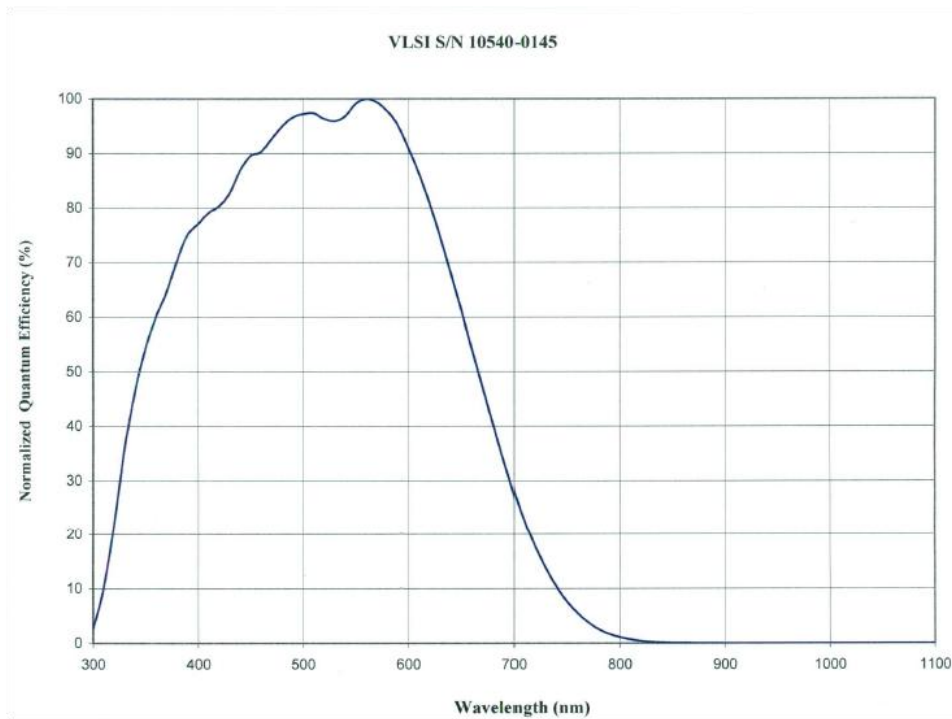


**Figure B.2 IPCE for Calibrated Reference Cell**

## Appendix C - Optimization of GSCs

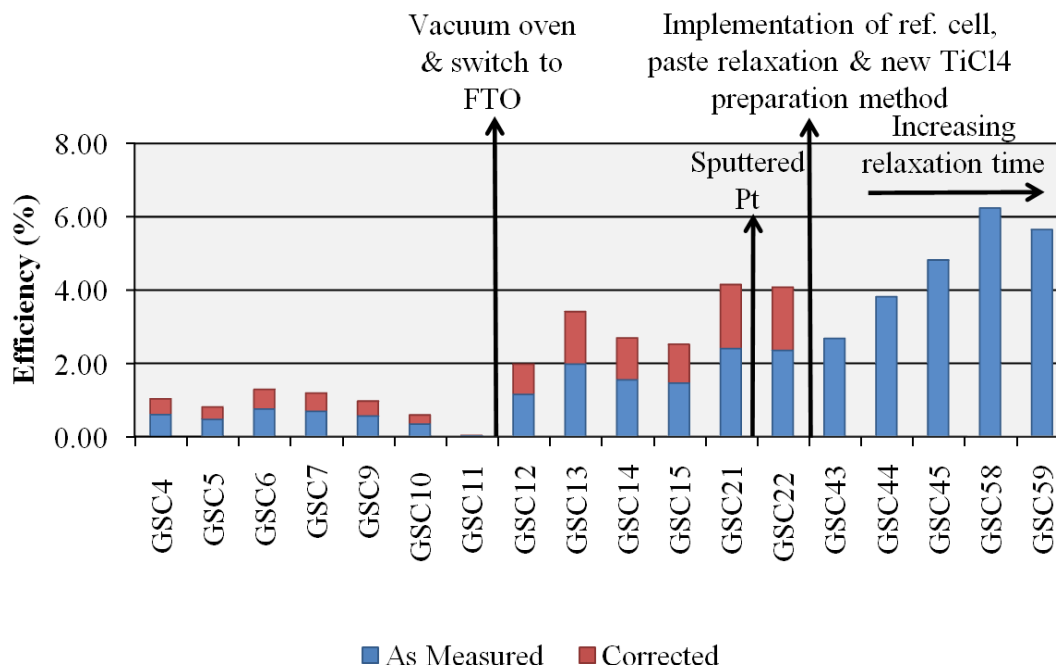
### Statistical Analysis of Single Layer GSCs

Table C.1 Single Layer GSCs Statistics

	$V_{OC}$ (V)	$J_{sc}$ (mA/cm <sup>2</sup> )	FF	$\eta$ (%)	$R_{SH}$ (k $\Omega$ )	$R_s$ (k $\Omega$ )
<b>Mean <math>\pm</math> 99% CI</b>	0.6586 $\pm$ 0.0174	9.494 $\pm$ 0.460	0.6487 $\pm$ 0.0362	4.054 $\pm$ 0.182	7.585 $\pm$ 5.542	0.01424 $\pm$ 0.00305
<b>Std Dev</b>	0.0151	0.400	0.0314	0.158	4.811	0.00265
<b>% Std Dev</b>	2.289	4.212	4.842	3.891	63.43	18.58

### Performance Effects Using Power Density Correction

In order to accurately test and compare solar cells, the solar simulator employed needs to be calibrated properly to the standardized solar irradiance of 1 sun (100 mW/cm<sup>2</sup>). As discussed in Chapters 2 & 3, this can be done using a calibrated reference cell. Prior to the implementation of the reference cell, the calculated efficiencies of the devices were much lower than expected. This was due to the use of an un-calibrated power meter & detector. When the power meter showed a detector reading of 100 mW/cm<sup>2</sup>, the true power density was only around 58 mW/cm<sup>2</sup>. Once the lamp was calibrated to the reference cell, instead of the power meter/detector, the detector read out on the power meter was now 160 mW/cm<sup>2</sup>. With the lamp calibrated, the measured photocurrents (for the reference cell) were increased by about 1.7x, which correlated to about the same increase in overall efficiency (between 1.6 & 1.7x). Figure C.1 shows the calculated efficiencies of some devices throughout the optimization process (in blue) using the as measured values. Also shown are the calculated efficiencies (accounting for power density correction – in red) of the devices measured prior to the reference cell calibration.



**Figure C.1 Calculated Efficiencies - As Measured vs. Power Density Corrected**

The efficiencies of the solar cells tested prior to implementation of the reference cell were re-calculated accounting for the discrepancy in the measured power density. Efficiencies slightly over 4% could have been obtained before the final optimizations steps had the system been properly calibrated with a reference cell. The efficiency increase upon switching to FTO is also clearly evident.

What can be taken from Figure C.1 is that if the proper calibration had been in place at the start, then some of the cells would have already been optimized enough to break 4% efficiency. Even if the reference cell had been used throughout the whole optimization process though, the devices would have still been further optimized past GSC22 since only 4% efficiency was achieved. Allowing the paste to relax prior to sintering afforded the achievement of efficiencies >5.5% (up to 6%). Further optimizations could still be done to the double layer cells to push their efficiencies past possibly 8%.

Figure C.1 further confirms that the use of FTO over ITO and allowing the paste to relax, are key steps in fabricating a respectably efficient GSC. Although the figure doesn't further confirm that the use of sputtered Pt and the integrity of the  $TiCl_4$  are key steps, it must be kept in mind that this graph doesn't represent all the fabricated cells and it is only of the efficiency.

These critical fabrication steps affect many of the parameters of the device (which in turn do affect the efficiency) but conclusions as to whether the fabrication step was critical or not can't be drawn solely on the efficiency (discussed in more detail in Chapter 3).

### Thermal Stability of ITO

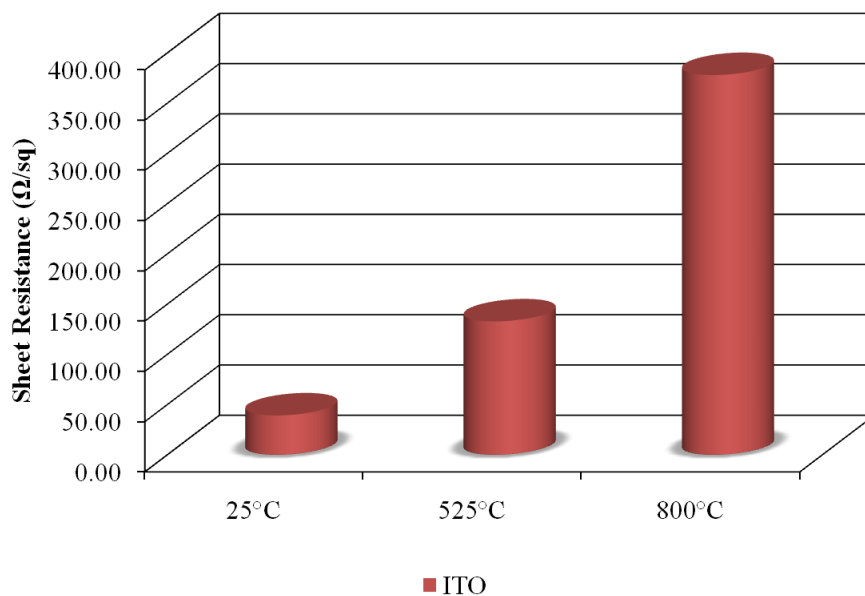


**Figure C.2 Temperature Effects on ITO Sheet Resistance**

**The thermal stability of ITO is quite poor, as is apparent from the above figure, which makes it a very poor candidate for GSC preparation. The GSC preparation requires temperatures  $>500^{\circ}\text{C}$  and at this high temperature the sheet resistance of the ITO has already more than tripled.**

### Sputtered Pt CE vs Various Pt Paste CEs

Although for the optimization of the double layer cells, a Pt CE that was sputtered gave much better performance over the Pt paste, when optimizing the single layer cells, a Pt paste CE was tested using paste from a different vendor (Dyesol Pt paste PT-1 vs. Solaronix Pt Catalyst T/SP). The problem with the Solaronix paste was that upon annealing, the Pt paste would not form a uniform thin layer of Pt (even when the paste layer was thick) therefore making the sheet resistance of the Pt thin film on the order of hundreds of  $\Omega/\text{sq}$  (sputtered thin film  $\sim 10 - 15 \Omega/\text{sq}$ ). This problem could be due to the Pt catalyst degrading or the catalyst is not

homogeneously dispersed throughout the solvent but the problem was not explored. The performance of the cell with the Dyesol paste was decent and was similar to that of the optimized single layer cells with sputtered Pt (Figure C.2). With some slight optimizations, using the Dyesol paste could prove to be just as effective as the sputtered Pt, while keeping the costs and sample preparation time down.

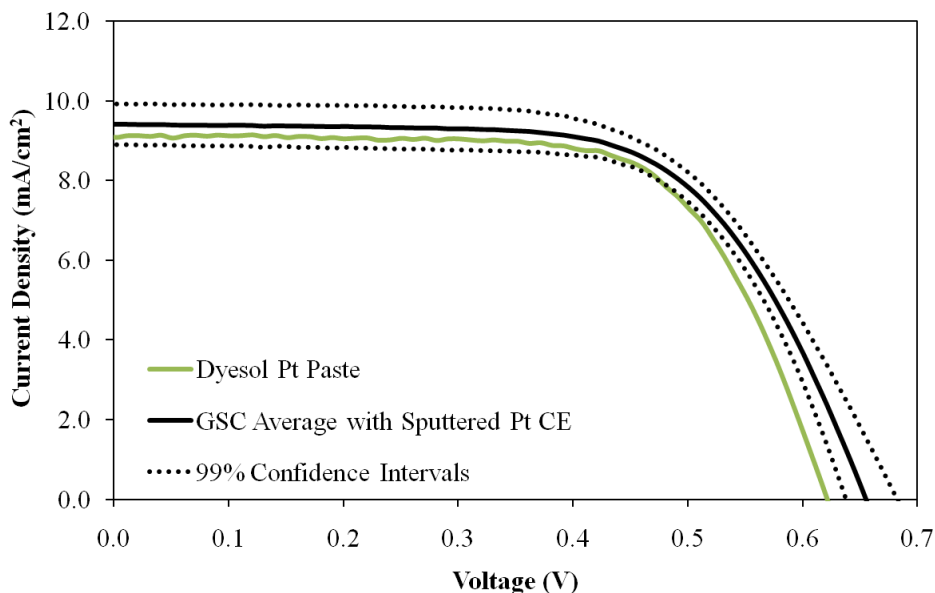


**Figure C.3 IV Curves - GSC Avg. with Sputtered Pt CE vs. Dyesol Pt Paste**

By employing a Pt paste from a different vendor, a GSC with the new Pt paste as the counter electrode gives an illuminated IV response almost within the 99% confidence intervals for five averaged GSC IV responses.

**Table C.2 Photovoltaic Characteristics - GSC Avg. with Sputtered Pt CE vs. Dyesol Pt Paste**

	$V_{OC}$ (V)	$J_{SC}$ (mA/cm <sup>2</sup> )	FF	$\eta$ (%)	$R_{SH}$ (k $\Omega$ )	$R_S$ (k $\Omega$ )
<b>Dyesol Pt Paste</b>	0.6212	9.094	0.6786	3.83	1.7556	0.0106
<b>Avg. of Sputtered Pt Cells</b>	0.6586	9.494	0.6487	4.05	7.585	0.014
<b>99% Confidence Intervals</b>						
<b>High</b>	0.6760	9.955	0.6849	4.236	13.127	0.0173
<b>Low</b>	0.6413	9.033	0.6125	3.872	2.042	0.0112

### FTO Surface Roughness

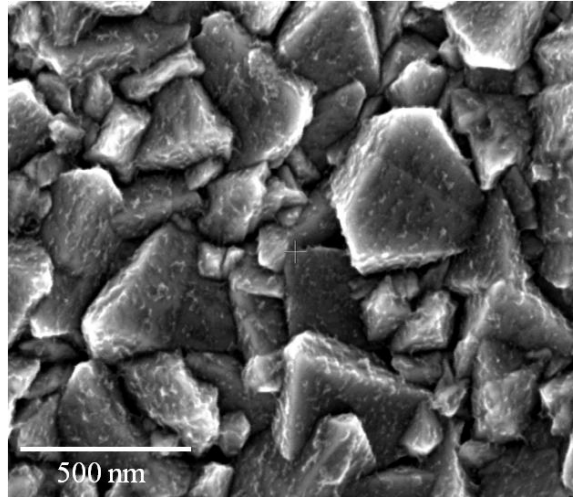


**Figure C.4 SEM Image FTO Surface Roughness**

The surface roughness of FTO is quite large which could explain why 40 nm of sputtered Pt gave a high series resistance. The rough surface may have led to a discontinuous film that would have a high resistance and thereby would increase the device series resistance. The image above was taken after a  $\text{TiCl}_4$  treatment which explains the apparent material on top of the FTO crystals.

### Criticalness of TiCl<sub>4</sub> Solution Integrity

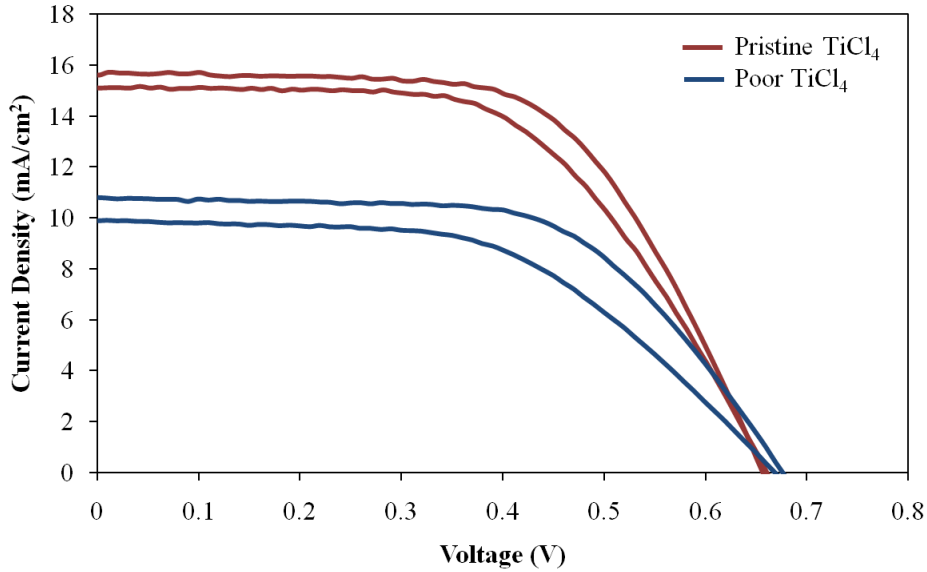


**Figure C.5 Poor TiCl<sub>4</sub> Solution Effects on Photovoltaic Performance**

Additional double layer GSCs were fabricated using the optimized parameters except allowing the integrity of the TiCl<sub>4</sub> to be compromised. The criticalness of this solution’s condition is apparent from the increased series resistances, decreased current densities, decreased fill factors, and decreased efficiencies.

**Table C.3 Photovoltaic Parameters - Pristine TiCl<sub>4</sub> vs. Poor TiCl<sub>4</sub>**

	V <sub>OC</sub> (V)	J <sub>SC</sub> (mA/cm <sup>2</sup> )	FF	η	R <sub>SH</sub> (kΩ)	R <sub>S</sub> (kΩ)
<b>Pristine TiCl<sub>4</sub></b>	0.6566	15.608	0.6084	6.24%	0.81	0.011
	0.6601	15.093	0.5671	5.65%	1.16	0.013
<b>Poor TiCl<sub>4</sub></b>	0.6760	10.802	0.5977	4.36%	1.33	0.018
	0.6611	9.599	0.5598	3.55%	1.09	0.023

Following the same preparation procedures for the optimized double layer GSC’s, two additional devices were made but were treated with a TiCl<sub>4</sub> solution whose integrity was compromised (solution allowed to sit around until it became opaque). From the above figure, it is clear that the TiCl<sub>4</sub> solution’s viability is crucial in decreasing the series resistances (particle

necking) and increasing dye adsorption i.e. increased short circuit current (increased surface roughness) which both led to increased fill factors and efficiencies.

## Appendix D - AuNP Incorporated DSSC's

For the first AuNPSCs fabricated, the AuNPs were deposited either by spin-casting or drop-casting. Both casting methods showed photocurrent enhancements, with a drop-casted cell showing the largest photocurrent enhancement of all AuNPSCs. (Figure D.1) Devices fabricated with the casting methods also showed photocurrent reductions as well. The performance inconsistencies can be attributed to the AuNP deposition irregularities which arise during dewetting. Due to this non-uniformity, a more controlled means of deposition (functionalization) was employed.

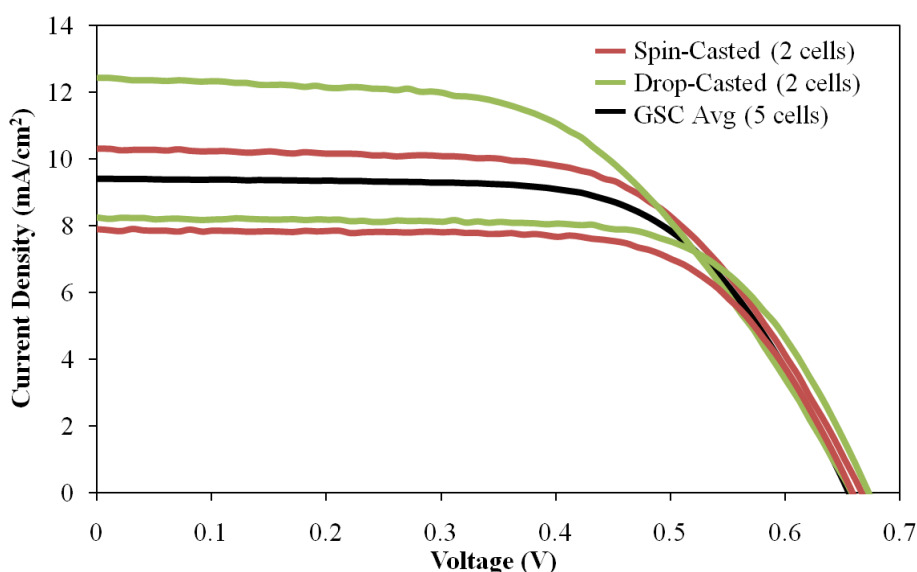


**Figure D.1 IV Curves - Casted AuNPSCs**

**Photocurrent enhancements and reductions were observed for AuNPSCs that had the AuNPs deposited both by spin-casting and drop-casting. The inconsistencies are attributed to the poor precision of these deposition techniques which comes from variations in the dewetting processes.**

Figure D.2 shows additional AuNP surface coverages that were tested. The high density (>20%) provided well dispersed AuNPs in certain areas but the degree of aggregation elsewhere was extremely large, leading to detrimental effects in the device's performance. Even for lower densities of NPs (~5%), the extent of the AuNP aggregation, although less than the high density

devices, was still considerable. Despite the aggregation though, the lower density devices generally gave higher photocurrent enhancements.

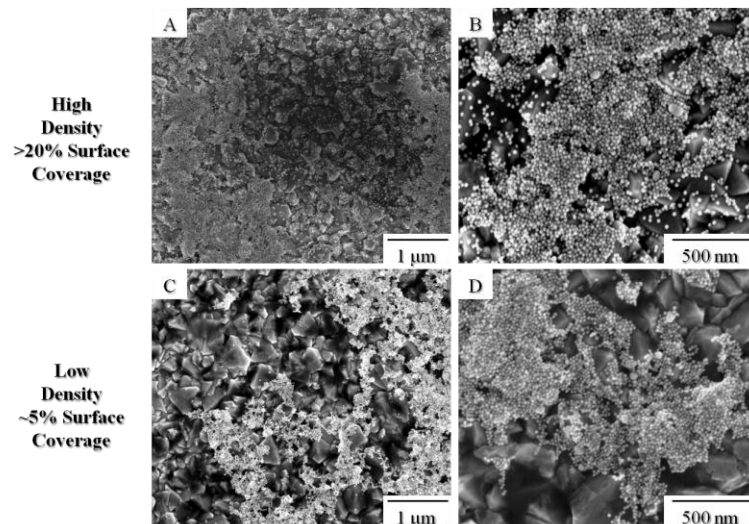


**Figure D.2 FESEM of AuNP Functionalization – High & Low NP Densities**

**Higher surface coverages gave well dispersed NPs in areas of the substrate but a majority of the NPs formed large aggregates. Even lower surface coverages of ~5% gave similar results but to a lesser extent than the higher coverages.**

Figure D.3b & c reiterate the effects that annealing (particle fusing) and electrolyte exposure (Au etching) have on NPs. Figure D.3a is of a highly aggregated AuNP area and upon annealing, these highly aggregated areas can form large particles or large islands (100s of nanometers in size) of Au film. These larger formations can have unfavorable effects on the device performance. As discussed above, a 30 minute electrolyte exposure time almost completely dissolves away the AuNPs leaving only remnants on the FTO surface. Therefore after a 2 hour exposure, the presence of even AuNP remnants was not likely as can be seen in Figure D.3c. There appeared to be a material present in various locations on the FTO surface but due to the deposition of  $\text{TiO}_2$  during the  $\text{TiCl}_4$ , a distinction between AuNP remnants and possible  $\text{TiO}_2$  deposition was not achievable.

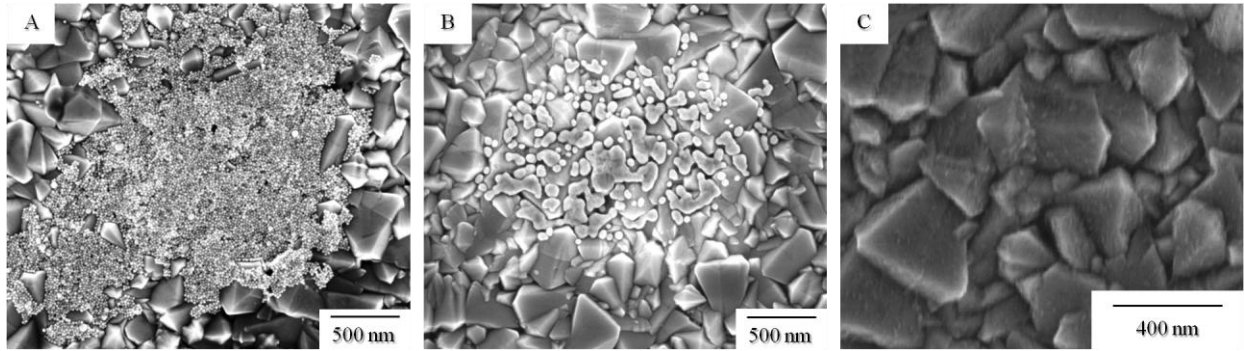


**Figure D.3 FESEM AuNPs - 2 Hr Electrolyte Exposure**

(A) shows a low surface coverage sample (~1.6%). (B) shows the thermal fusion effects of the NPs. In (C) no NPs remained with hardly any remnants of the particles either, which was expected since after a 30 min. exposure there was little NP remnants left.

### Additional Characterizations

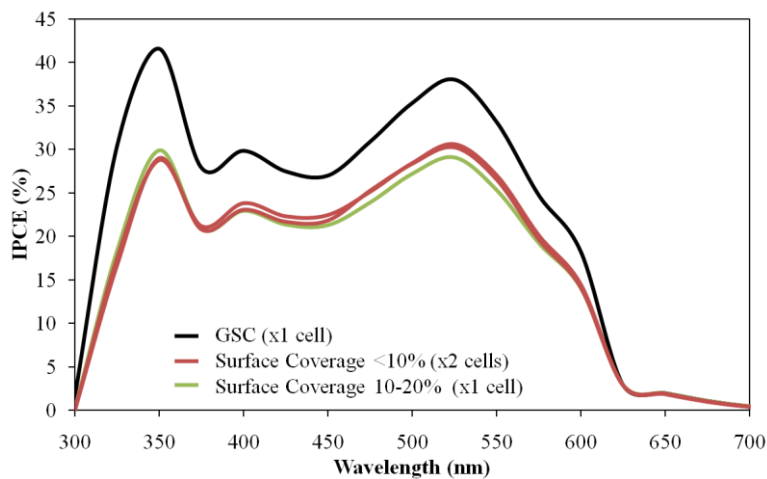


**Figure D.4 IPCE - AuNPSCs (IV Curves Tested At Different Light Intensities)**

IPCE for the AuNPSCs that were tested at different light intensities again shows a similar trend to previous IPCE curves in that the low surface coverage devices show reduced IPCE.

IPCE was also performed on the AuNPSCs (& GSC) that were tested at various light intensities. The results coincided well with the previous IPCE measurements in that the AuNPSCs display a lower photon to current conversion efficiency than the GSC.

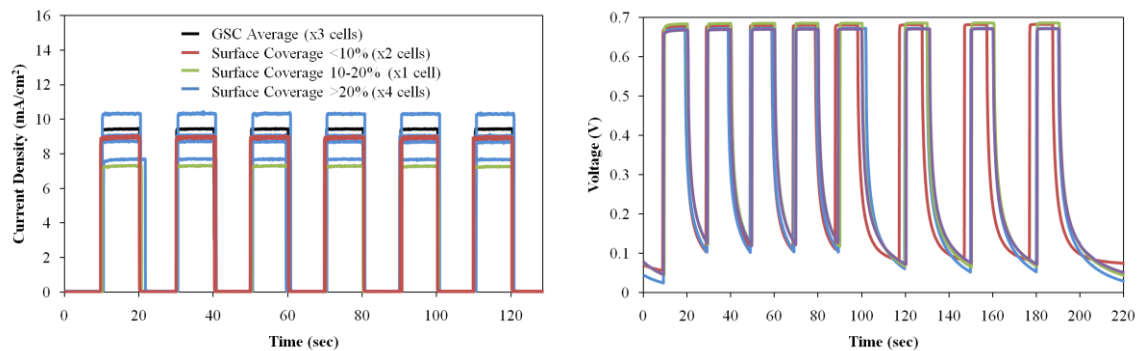


**Figure D.5 AuNPSCs  $J_{SC}$  and  $V_{OC}$  Illumination on/off tests**

**Certain AuNPSCs were subjected to chronoamperometry and chronopotentiometry in order to test stability. The devices were stable during the testing period and also from the chronoamperogram it is evident that the devices are not diffusion limited.**

The short circuit currents (chronoamperometry) and open circuit voltages (chronopotentiometry) under interrupted illumination conditions were also recorded, just as the GSCs. The resultant photocurrents and photovoltages are shown above in Figure D.5 (short circuit current on the left and open circuit voltage on the right). Both the open circuit voltages and the short circuit currents of the devices were stable and the devices were not limited by electrolyte diffusion during operation (no photocurrent decay over time).